OPEN ACCESS



First Sagittarius A* Event Horizon Telescope Results. VIII. Physical Interpretation of the Polarized Ring

The Event Horizon Telescope Collaboration (See the end matter for the full list of authors.)

Received 2024 January 4; revised 2024 February 16; accepted 2024 February 17; published 2024 March 27

Abstract

In a companion paperwe presenthe first spatially resolved polarized image of Sagittarius on eventhorizon scales, captured using the Event Horizon Telescope, a global very long baseline interferometric array operating at a wavelength of 1.3 mm. Here we interpretthis image using both simple analytic models and numeriogeneral relativistic magnetohydrodynamic (GRMHD) simulationise large spatially resolved linear polarization fraction (24%–28%, peaking at ~40%) is the most stringent constraint on parameter space, disfavoring models that are too Faraday depolarize similar to our studies of M87, polarimetric constraints reinforce a preference for GRMHD models with dynamically important magnetic fiel Asthough the spiral morphology of the polarization pattern is known to constrain the spin and inclination angle, the time-variable rotation measure (RM) desgivalent to ≈46° ± 12° rotation at 228 GHz) limits its present utility as a constraint. If we attribute the RM to internal Faraday rotation, then the motion of accreting material is inferred to be counterclock voisietrary to inferences based on historical polarized flares, and no model satisfies all polarimetric and total intensity constraints. On the other hand, if we attribute the mean RM to an external araday screen then the motion of accreting material inferred to be clockwise, and one model passes all applied total intensity and polarimetric constraints: a model with strong magnetic fields, a spin parameter of 0.94, and an inclination of 150°. We discuss how future 345 GHz and dynamical imaging will mitigate our present uncertainties and provide additional constraints on the black hole and its accretion flow.

Unified Astronomy Thesaurus concepts: Black holes (162); Supermassive black holes (1663); Black hole physics (159); Galactic center (565); Radio interferometry (1346); Polarimetry (1278); Magnetohydrodynamics (1964) Supporting material: figure set

1. Introduction

Synchrotron emission from the plasma neasupermassive black holes (BHs) provides a crucial source of insight into the physical processes that drive accretion and outflow in galactic of a Kerr BH with a mass $M \approx 4 \times 10^6 M_e$ that is only cores.It is intrinsically polarized, and both linear polarization and circular polarization provide information about the emitting accreting a trickle of material relative to that captured atthe plasma's density, temperature composition, and magnetic.

Bondi radius in a radiatively inefficient manner (e.g., plasma's density, temperature, composition, and magnetic field. In the rest frame of the emitting fluid, the linear polarization direction is orthogonal to the local magnetic fields. magnetized plasma along the line of sightmparts additional polarimetric effects via Faraday rotation, which rotates the plane of linear polarization with a $\frac{1}{3}$ dependencewhere λ is the observing wavelength, and Faraday conversion, which exchanges linearnd circular polarization states Finally, for emission near a BHthe polarization is subjecto achromatic rotation from propagation in a curved spacetime.

Recently, the Event Horizon Telescope (EHT) Collaboration published images of the supermassive BH at the Galactic center, Sagittarius Å (Sgr A*; Event Horizon Telescope

Original content from this work may be used under the terms of the Creative Commons Attribution 4.0 licence. Any further distribution of this work must maintain attribution to the author(s) and the title of the work, journal citation and DOI.

Collaboration et al. 2022a, 2022b, 2022c, 2022d, 2022e, 2022f, hereafter Papers I–VI)These images revealed a bright emission ring encircling a centralbrightness depression (the "apparentshadow"), consistent with the expected appearance Hilbert 1917; Bardeen 1973; Luminet 1979; Jaroszynski& Kurpiewski 1997; Falcke et al. 2000). Comparisons of the EHT so images of linear polarization capture the projected magnetic measurements with numerical simulations provide estimates of field structure perpendicular to the line of sight. Any magnetized plasma along the line of sightmarts additional luminosity that is $L = 10^{6} \, \text{erg s}^{-1} \sim 10^{-9} \, \text{L}_{\text{Edd}}$ (see, e.g., Paper V, and references thereinHere M_B is the Bondi mass accretion rate and $L_{Edd} = 4\pi GMc \text{ m/}\sigma_T$ is the Eddington luminosity, with G, c, m_{D} , and σ_{T} being the gravitational constant, speed of light, proton mass, and Thomson cross section, respectively. Previously, measurements linearly polarized emission near Sgr*Agave strong evidence for this low accretion state (e.g., Agol 2000; Quataert& Gruzinov 2000). In addition, the emission ring morphology, including the lack of a pronounced brightness asymmetry in EHT images. favors a viewing angle in Sgr Å that is at a low to moderate inclination ($\square 50^\circ$) relative to the angular momentum of the inner accretion flow (see.g., Figure 9 in Paper V).

> Event Horizon Telescope Collaboration et al. (2024, hereafter Paper VII) reports the firstpolarized images of Sgr Å using EHT observations at 230 GHz taken in 2017. These images show a prominent spiral polarization pattern in the emission ring

¹⁵⁴ NASA Hubble Fellowship Program Finstein Fellow.

that is temporally stable, strongly linearly polarized (≈25%), and dominated by azimuthally symmetric structure. Both the image- Polarimetric Constraints Derived from the Static Reconstruction of Sgr A averaged polarization fraction (m_t~ 5%) and the resolved polarization fraction ($\langle |m| \rangle \approx 25\%$)are significantly higherin Sgr A than in the EHT's observations of Marevent Horizon Telescope Collaboration et al. 2021a, hereafter Reper VII). In M87, this polarization pattern was explained by coherent an dynamically important magnetic fieldsepolarized by Faraday effects (EventHorizon Telescope Collaboration et l. 2021b, hereafter M87 Paper VIII).

In this paper, we provide the theoretical modeling and interpretation to accompany Paper VII. In Section 2, we summarize the new polarimetric observationabnstraints on Sgr A*. In Section 3, we provide general arguments about what Note. These two methods each provide posteriors, from which 90% confidence these constraints imply for Sgr A* through comparison with plasma properties geometrical ring models to evaluate the degree of coherence in the polarized imagend semianalytic emission models to evaluate the interplay between spacetime and emission parametersin determining polarized image structure.In Section 4, we describe a large library of general relativistic magnetohydrodynamic (GRMHD) imulations for Sgr A. In Section 5, we evaluate which of these GRMHD models are compatible with the observationadonstraints.In Section 6, we summarize our findings and describe the prospects for improved constraints from future observations of Sgr A*.

2. Summary of Polarimetric Observations

the Sgr A EHT data taken on 2017 April6th and 7 between 226.1 and 230.1 GHz (see Section 2 of Paper VII for more details). For theoretical interpretation, we adopt eight observa- explored in this paper are computed, listed in Table 1. To tional constraints derived from images generated by the THEMIS and the m-ring reconstruction methods (note that "m" is the azimuthal/angular mode number hereot polarization fraction; see Johnson et al. 2020). Of the four methods include these images and then inferred 90% confidence regions. in Paper VII, these are the only methods that provide Bayesianm-ring method does not provide independent values of vnet posteriors from which we compute 90% confidence intervals. sense bracketthe possible spatia and temporal variability. In brief, the m-ring method fits a ring model to each snapshot independently, but the allowed spatial variability is very limited (see Figure 10 in Paper VII for a visualization). by construction (m _ 2 for total intensity, m _ 3 for linear polarization, and m _ 2 for circular polarization)n contrast, THEMIS attempts to optimize a single static image most consistentwith the full data over time, with a noise budget attributed to time variability. Despite the vast differences between these modelthey recover key image quantities with similar accuracy in synthetic data tests and arrive amostly consistent observables (Paper VII).

Throughoutthis work, the large and time-variable rotation measure (RM) of Sgr poses a significant systematic uncertainty. Defined as RM $\equiv \Delta \chi/\Delta k^2$, where χ is the electric vector position angle (EVPA), the RM of Sgr A may originate from Faraday in the plasma probed as a function of optical depth, or a combination of these effects. Examining the polarized light curve ferred from our static image reconstruction vielgus et al. for the same 2 days as our EHT observations, Wielgus et al. (262222b, 2024) find 2.6% < m_{net}< 11% and −2.1% < v_{net}< arrive at \acute{a} RMñ = -4.65 $^{+1.25}_{-1.18}$ $^{'}$ 10 5 rad m 2 . We reservea lengthy discussion ofhe RM of Sgr Å in both observations and theory for Appendix On summary the fraction of the RM

Table 1

Observable	m-ring	THEMIS	Combined
m _{net} (%)	(2.0, 3.1)	(6.5, 7.3)	(2.0, 7.3)
v _{net} (%)	L	(-0.7, 0.12)	(-0.7, 0.12)
ୁ(m ⟩ (%)	(24, 28)	(26, 28)	(24, 28)
(lm ⟩ (%) nd ⟨ v ⟩ (%)	(1.4, 1.8)	(2.7, 5.5)	(0.0, 5.5)
β ₁	(0.11, 0.14)	(0.10, 0.13)	(0.10, 0.14)
$ \beta_2 $	(0.20, 0.24)	(0.14, 0.17)	(0.14, 0.24)
∠β₂ (deg) (as observed)	(125, 137)	(142, 159)	(125, 159)
∠β₂ (deg) (RM derotated)	(-168, -108)	(-151, -85)	(-168, -85)
$ \beta_2 / \beta_1 $	(1.5, 2.1)	(1.1, 1.6)	(1.1, 2.1)

regions are quoted. As constraints on our models, we conservatively adopt the three simple models: one-zone physical models to evaluate the inimum and maximum of these 90% confidence regions from both of these methods combined (rightmostolumn), with the exception of $\langle |v| \rangle$, which is treated as an upper limit. Derotation assumes that the mean RM can be attributed to an external Faraday screen, for which a frequency of 228.1 GHz is adopted.

that can be attributed to an externational screen is currently unresolved. Thus, throughout this work we consider the recovered image statistics both with and without RM derotation. Derotating the image corresponds to an interpretation where the time-average RM is attributed to a relatively stable externational screen, separate from our models, which can be corrected for. Refraining from doing so corresponds to an interpretation in which all of the RM is generated internally within our models. Our GRMHD In Paper VII, static polarimetric images are constructed from simulations can reproduce the intraday variability of the RM. but not its stability of sign (see Appendix C).

For each of these methodseight observationabonstraints generate these ranges, large quantity of images consistent with the data were generated from each method's posterior distribution. We computed the relevant observables for each of which is fixed to the mean ALMA-inferred value for circular These methods make drastically different assumptions and, in golarization analysis (see Paper VII). When combining the two methods for theoretical hterpretation, we adopt the minimum and maximum of the union of both 90% confidence regions

> The quantities met and vet correspond to the net linear and circular polarization that would be inferred from a spatially unresolved measuremefor the time-averaged imageThese are given by

$$m_{\text{net}} = \frac{\sqrt{\left(\mathring{\mathbf{a}}_{i} \mathbb{I}_{i}\right)^{2} + \left(\mathring{\mathbf{a}}_{i} \mathbb{I}_{i}\right)^{2}}}{\mathring{\mathbf{a}}_{i} \mathbb{I}_{i}},$$
 (1)

$$V_{\text{net}} = \frac{\mathring{\mathbf{a}}_{i} \square i}{\mathring{\mathbf{a}}_{i} \square i}, \tag{2}$$

rotation internal to the emitting region, an external screen, changes where Σ denotes a summation over each pixel i. For the timein the plasma probed as a function of optical depth or a resolved light curves, which are distinct from the values - 0.7%, respectively, where we quote the centra 90% of the values observed during the same 2 days of observation. Interestingly, we find that the m-ring method arrives at much

lower values of methanTHEMIS, which may be attributable to temporal cancellations of fluctuating EVPA patterns.

The remainder of our constraints are structuraduantities. beginning with $\langle |m| \rangle$ and $\langle |v| \rangle$, the image-averaged linear and circular polarization fractionThese are given by

$$\acute{\mathbf{a}}|m|\tilde{\mathbf{n}}| = \frac{\mathring{\mathbf{a}}_{i}\sqrt{\square_{i}^{2} + \square_{i}^{2}}}{\mathring{\mathbf{a}}_{i}\square_{i}}, \tag{3}$$

$$\mathbf{\acute{a}}|V|\tilde{\mathsf{n}} = \frac{\mathring{\mathsf{a}}_{i}|\mathbb{D}_{i}|V| |V|}{\mathring{\mathsf{a}}_{i}|V|}. \tag{4}$$

Note that these quantities depend on the effective resolution of our images. Throughout this work we quote values from our simulations corresponding to 20 µas resolution to mimic EHT resolution. We treat the resolved circular polarization fraction (|v|) as an upper limit, and thus the combined range extends to 0 in Table 1. This is due to the fact that the circularly polarized images presented in Paper VII show structural differences that we attribute to noise (see also Event Horizon Telescope Collaboration etal. 2023, hereafter M87 Paper IX). Because of the absolute magnitude inherento the definition of this quantity, it is biased high when the signal-to-noise ratio is too low.

Complex B modes correspond to Fourier decompositions of the linear polarization structure, here m refers to the number of times that an EVPA tick rotates with azimuth (Palumbo et al. 2020). These coefficients are defined by

$$b_{m} = \frac{1}{I_{\text{tot}}} \grave{Q}_{0}^{*} \grave{Q}_{0}^{2p} P(r,j) e^{imj} r \mathcal{G}_{j} \not D, \qquad (5)$$

$$I_{\text{tot}} = \grave{\mathbf{Q}}^{\text{V}} \grave{\mathbf{Q}}^{2p} I(r,j,j,j,q,d)$$
 (6)

P = Q + iU. The rotationally invariant mode, β_2 , has natural connections to what we believe are azimuthally symmetric disk/jet structures, in particular the magnetic field geometry. ItsStokes brightness is indicated in the diverging colomap, with red/blue amplitude encodes the strength of this mode, hile its phase encodes the pitch angle and handedness of EVPA tick&le observe ∠β closer to ±180° than 0°, which corresponds to tick patterns that are more toroidal than radial.

When considering observational constraints without RM derotation, we simply adopt the range of $\angle \beta_2$ as observed on the sky. When considering observationabnstraints with RM derotation,we derotate ∠ß assuming that there is an external Faraday screen between us and the emitting region that we capality as a probe of rotational symmetry. Since there is no characterize by the mean RM over time. Since depends on twice the EVPÅ, we therefore add $-2\langle RM\rangle \hat{\mathcal{K}}$ to $\angle\beta_2$, where $\langle RM\rangle$ is the mean RM observed on April 6 and 7Therefore, the range on $\angle \beta$ had been significantly shifted by the Faraday screen by $2RM^2 = -92.0^{+24.7}_{-23.4}$ deg. Applying this derotation both shifts and broadens the constraint.

Mean images from the posterior distributions generated by each method are plotted in Figure 1. Two sets of linearly and with derotation, respectively. Note that derotation reverses image of Sgr Å exhibits three salient features: polarized images are showporresponding to images without the handedness of the polarization spirathich has important implications for the flow structureln the first two rows, total intensity is shown in gray scalewith contours drawn at 25%, 50%, and 75% of the peak brightness. These same contours are 3. The ordered structure exhibits a high degree of rotational repeated in the bottom rowln the top and middle rows, the

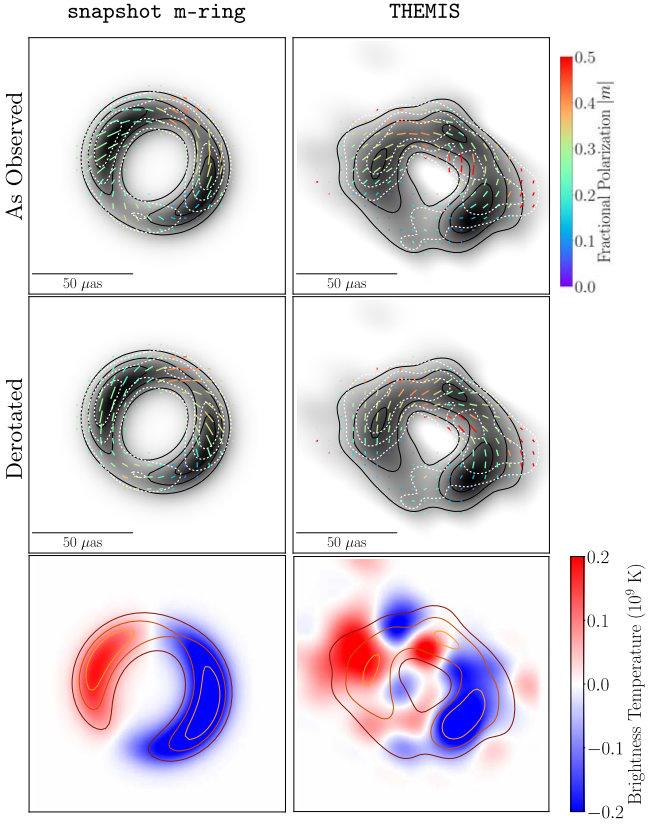


Figure 1. Polarized images of Sgr Aused for physicalinterpretation in this work. Two methods from Paper VIIsnapshot m-ring and THEMIS. included. Top and middle total intensity is shown in gray scalepolarization ticks indicate the EVPA, the tick length is proportional to the linear polarization intensity magnitude, and color indicates fractional linear polarization. The dotted contour levels correspond to linearly polarized intensities of 25%, 50%, and 75% of the polarization peak. The solid contour levels indicate total where ρ and j correspond to polar coordinates in the image and htensity at 25%, 50%, and 75% of the peak brightness he top row shows images without derotation, and the middle row shows images with a derotation of 46.0 deg to account for Faraday rotation. Bottom: total intensity is indicated in solid colored contours at 25%, 50%, and 75% of the peak brightness, and the indicating a positive/negative sign.

colored ticks encode linear polarization, where the length scales with the total linearly polarized intensity and the color scales with the fractional polarization. The dashed white contours plot the linearly polarized intensity rather than the total intensity.

Finally, we also compute the simplest nonrotationally symmetric mode, β_1 , as a probe of polarization asymmetry. Again, $|\beta_1|$ encodes the strength of this mode, and we use clear axis (such as the spin axis) to define ₹60°, we do not study $\angle \beta_1$. We also refrain from computing higher-orde β_m modes, which are more likely to be sensitive to smaller-scale noise fluctuations.

3. Analytic Models

As discussed in the previous sectiothe linearly polarized

- 1. It has a large resolved polarization fraction of 24%–28%, with a peak of ~40%, much higher than M87.
- 2. The linear polarization structure is highly ordered.
- symmetry, which appears to spiral inward with

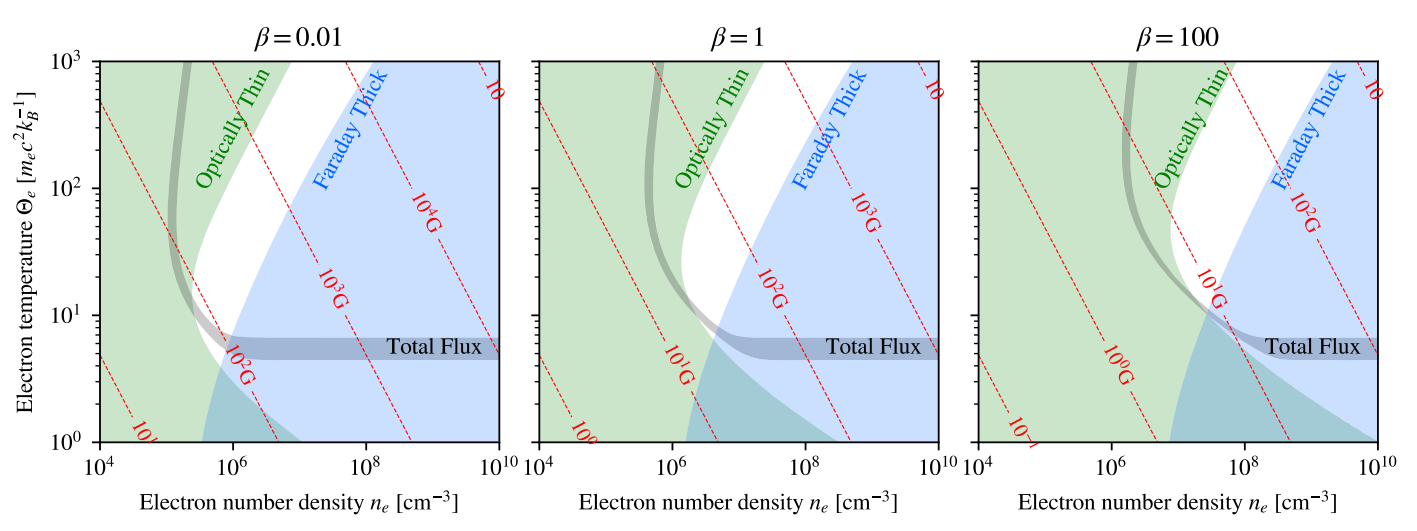


Figure 2. Allowed parameter space in electron number density and dimensionless electron temperature to the one-zone model described in Section 3.1. The panels correspond to different assumed values of plasma 🚜 🕍 Pμag We require that the total flux density 2 Jy 🗧 3 Jy (gray region) and optical depth τ < 1 (green region). Corresponding magnetic field strengths are shown as red dotted lines. In blue, we plot the Faraday thick redam Unlike for M87, we find that the model is Faraday thin wherever there is intersection between our two constraints.

counterclockwisehandednessafter derotating by the apparent RMor clockwise without derotating.

Before exploring more physically complete GRMHD models, we demonstrate that each of these features can be understood in polarized synchrotron emission and transfercoeffithe context of simple analytic models.

3.1. One-zone Modeling

We use the basic assumptions described in Paper that Sgr A is an accreting BH with extremely small Eddington ratio and follow M87 * Paper VIII to include polarimetry. This polarized one-zone model validates the more complicated numerical models shown later in this paper and offers a natural regions in Figure 2 respectively. The magnetic field strengths explanation for the high polarization fraction of Sgrralative to M87^{*}.

We model the accretion flow around Sgr Å as a uniform sphere of plasma with radius $r = 5 r_g$, where $r_g = GM/c^2$, comparable to the observed size of Sgr A^{*} at 230 GHz (Papers III and IV), with uniform magnetic field oriented at fiducial 60° inclination relative to the line of sight. The outcomes of our one-zone modelepend only weakly on the field orientation. Note that the plasma velocity and the gravitational redshift are neglected.

ion-electron temperature ratio is 3, the ions are subvirial by a factor of 3, and plasma $\beta \equiv P_{gas}/P_{mag} = 1$. Adopting the observational flux constraint $\not \equiv 2.4$ Jy (Wielgus et al. 2022a), we obtained the self-consistent solution n_e; 10 ⁶ cm⁻³ and B; 29 G. Using this solution, we can estimate the strength of the Faraday rotation at 230 GHz with the optical depth to Faraday rotation t_{r_v} :

$$t_{r_V} \gg r r_V \square 0.98 \left(\frac{r}{5 r_g}\right),$$
 (7)

where ρ_V is the Faraday rotation coefficient(e.g., Jones& Hardee 1979). In contrast, similar modeling arrived at $t_{r_{V}} \sim 5.2 (^{f}/5 \, ^{r}g)$ for M87* (M87* Paper VIII). The value inferred for Sgr A suggests that the internal Faraday rotation may not be negligible (see also Wielgus et al. 2024), but it also may not necessarily lead to substantial depolarization.

By including optical depth effects and using the Dexter cients, we relax some assumptions, such as ion-electron temperatureratios and virial factor, and plot the allowed parameter space as in M8Paper VIII. Specifically,

- 1. we relax the flux constraint to 2 Jy ≤ ₹ 3 Jy to include the effect of variability; and
- 2. we require the same assumption that \mathbf{A}^{\star} is optically thin, i.e., $\tau < 1$.

The above requirements are marked by the gray and green are shown as red dotted contour lines, and the different panels assumedifferent plasma β. In blue, we plot the contour corresponding to $t_{f_V} > 2p$, beyond which internal Faraday depolarization becomes increasingly important. Unlike for M87 (see Figure 2 of M87 Paper VIII), we find that the regions where the totaflux and optically thin constraints are satisfied only occur in Faraday thin regions of parameter space. We note that this is compatible with multifrequency RM measurements that suggest $t_{r_V} \sim 1$ (Wielgus et al. 2024). In Paper V, we assumed that the plasma is optically thin, the Again, this is enough to noticeably rotate the EVPA pattern, but not enough to cause substantial depolarization.

In summary, the total flux and optical depth constraints of Sgr A naturally require small Faraday deptheshich explains the large inferred values of $\langle |m| \rangle$.

3.2. Ordered Polarization: Ordered Fields

Because beam depolarization can only decrease the observed polarization fraction, measurements of the linear polarization at varying angular scales provide information about the degree of order in the underlying polarization. A priori, it could be possible that the underlying magnetic field is significantly tangled on scales much smaller than the bealthowever, the combination of unresolved (met≈ 0.07) and EHT-resolved $(\langle |m| \rangle \approx 0.25)$ linear polarization measurements constrains the degree of order in the trueunderlying polarization pattern on

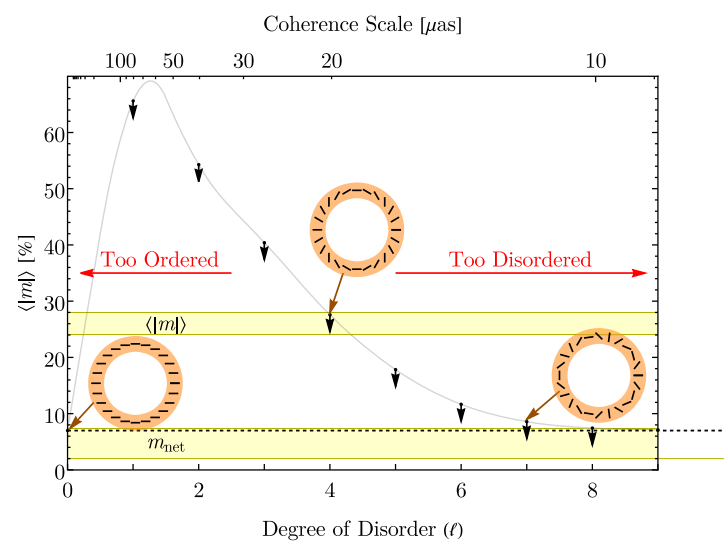


Figure 3. The combination of unresolved (met) and EHT-resolved ((|m|)) linear polarization measurements (at 20 µas resolution) constrains the degree din flows have been used for decades to gain tractable yet order in the underlying polarization image. In this schematic example, a polarized m-ring has a fixed netpolarization, m_{het} = 0.07 (denoted with the black dashed line) together with a single strongly polarized mode atigher order, ℓ , that controls the degree of disorder. For small values of ℓ , the resulting explore a very simple model, KerrBAM (or Kerr Bayesian image is too ordered, with (|m|) exceeding our observed value for Sgr A* (denoted with the uppervellow band). For large values of m, the resulting image is too disordered, with beam depolarization eliminating the highly polarized image structureIn this example, the fields must be substantially ordered to be consistent with our observations of Sgr A, with polarized structure that is coherent on scales of the $\ell \approx 4$ mode, corresponding to angular assuming an equatorial ring of emission with a specified fluid ordered to be consistent with our observations of Sgr A, with polarized scales of $\theta \approx 4\theta \approx 20 \mu as$.

scales smaller than our beam size, disallowing significant spatially unresolved disorder.

polarization confined to two azimuthal Fourier modesbeled with index ℓ . First, we include a constant (ℓ = 0) mode that defines met. We fix the amplitude of this mode to be 0.07 to match unresolved observations of Sgr A. Next, we add a second mode with varying index $\ell > 0$ and an amplitude of 0.7, similar to the peak fractional polarization expected for synchrotron emissionBy varying ℓ , we can crudely assess the allowed degree of coherence in the polarization of Sgr A

Figure 3 shows the resolved fractionablarization (|m|) at an angular resolution of 20 µas as a function of the secondary mode index ℓ . Both a perfectly ordered polarization field ($\ell = 0$) and a highly disordered polarization field (ℓ ? 1) will have $m_{net} \approx \langle |m| \rangle$. For the former, there is no beam depolarization; high value of $\langle |m| \rangle$ relative to m_{net} that we observe is a powerful diagnostic of coherent polarized structure.

fractions that are too high, while large values of ℓ produce resolved polarization fractions thatre too low. Many effects that are notincluded in this toy modelcould further decrease the resolved fractional polarization—the amplitude of the small-scale polarization structure could be significantly less than the synchrotron maximum (e.g. from optical depth or Faraday depolarization), there could be a mix of more than tw

modes, and there could be radial polarization structure that causes beam depolarization Hence, this example provides a conservative lowerlimit on the scale of coherentpolarized structure. To be consistent with our measurements of Sqr A we require $\ell \square$ 4corresponding to structure on angular scales of $q \gg \frac{p}{r} 5q_1 \gg 20 \, mas$ Here $\theta_1 = r_q/d$, where d is the distance and $5\theta_{\alpha}^{\dagger}$ is the approximate radius of the emission ring in Sgr A. Hence, even without detailed modeling we anticipate that the underlying polarization in Sgr A is highly ordered, with significant power on azimuthal scales of $\theta \approx 4M$ or more. That is, the large resolved polarization fraction implies relative order of the magnetic field pattern on scales below the beam size.

3.3. Decoding the Polarization Morphology

Semianalytic models enable computationally inexpensive investigation of the effects of model parameters on images. For example, semianalytic models of radiatively inefficient ccrephysically motivated insights into accretion flows (Bromley et al. 2001; Broderick et al. 2009, 2011, 2014, 2016; Pu et al. 2016; Pu & Broderick 2018; Vincent et al. 2022). Here we Accretion Modeling), a semianalytic model for equatorial, axisymmetric synchrotron emission around a Kerr BH (Palumbo etal. 2022). This modeling framework carries out velocity, magnetic field geometry and radial emission profile. Here we use this simple model to illustrate the effects of inclination and spin on polarized image structure.

As our starting point, we average magnetic fields and As a simple toy model, we analyzed a thin, circular ring with velocity fields in three KHARMA GRMHD simulations (to be discussed in Section 4) in both time and azimuth. We specify a ring of emission centered at a radius of am dam duse the values of the fluid velocity and magnetic field extracted from the GRMHD midplane at this radius 7.7 To give the emission ring a realistically finite width, the emission is spread in a Gaussian spanning approximately 4f-8ra, keeping the velocity and magnetic field vectors constant/with these valuesKerrBAM is able to capture the effects of beamingame draggingand lensing on the resultanimage. Note that this model excludes the likely contribution of emission off the midplane (e.g., Falcke et al.1993; Markoff et al.2007).

For three different magnetically arrested disks (MADs) with spins of 0, +0.5, and +0.94, we plot several polarimetric quantities of interest (leftmost column) and their model images for the latter, the beam depolarization eliminates all small-scale (subsequent columns) in Figure 4. Along with the polarimetric polarized power, even at the resolution of the EHT. Hence, the observables, we overlay our constraints in gray, where for ∠β the range without RM derotation is shown as a hatched region. Since this modelplaces emission exactly at me midplane by As expected, small values of ℓ produce resolved polarization construction images produced at inclinations too close to 90° are misleading and therefore not included. The KerrBAM prescription doesnot include Faraday effects, only crudely modeling optical depth (in this case applying a midplanenormal crossing optical depth τ_{\perp} = 0.5 applied uniformly to

This toy model is equivalent to the "m-ring" model used in Paper VII, but we label with the index " ℓ " here to avoid ambiguities.

¹⁵⁶ Ratherthan four-vectorcomponents, we average the Hodge dual of the , Faraday tensor and then reconstruct the averaged magnetic field vector from the condition $b^\mu u_\mu = 0$.

The velocity is computed in the frame of the zero angularmomentum observer in Boyer-Lindquist coordinates, while the magnetic field is computed in the fluid frame.

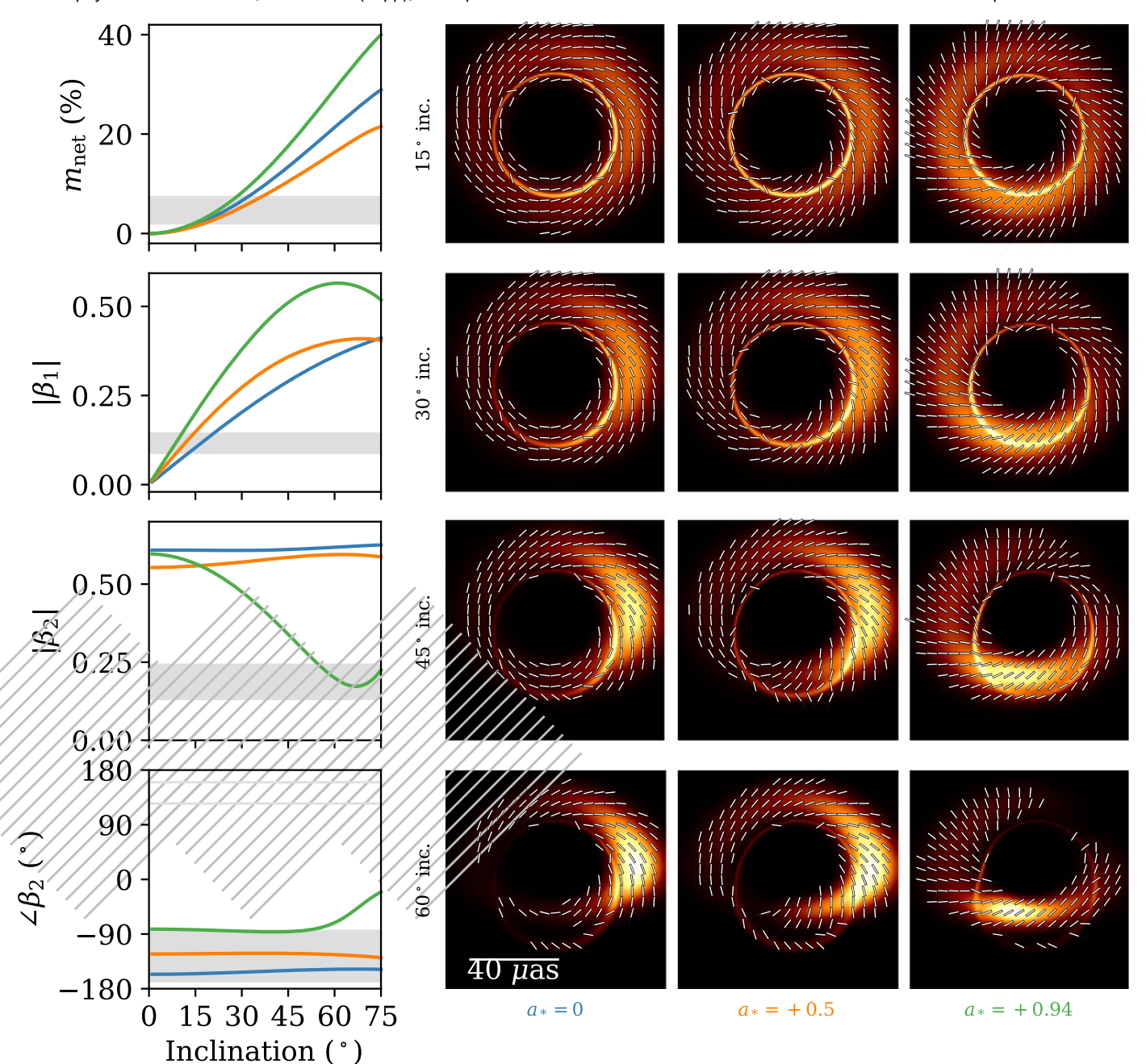


Figure 4. Left column; image quantities determined from simplified analytic KerrBAM models evaluated using MAD GRMHD fluid velocities and magnetic fields of three spins. In this and subsequent figures, we plot our observational constraints as gray bands for reference with their their to RM derotation shown as a hatched region. We use this model to understand key trends, but we caution that more physically complete GRMHD models are necessary for quantitative compar Right three columns: corresponding KerrBAM images evaluated at four example inclinations.

 \mathbb{I} , \mathbb{I} , and \mathbb{I}) and assuming a prespecified emission model confined to the midplane, so detailed agreement with the GRMHD models is neither expected nor achieved. Nevertheless, this model is useful for understanding several qualitative trends in our GRMHD library that are successfully reproduced.

First, the net polarization is minimized atlow inclination, since the symmetry of the accretion flow causes cancellation of 180 \square $\angle \beta$ \square 0 owing to their more spiral EVPA structures. polarization in the integrated image. The amplitude of the rotationally invariant mode β_2 is always high, due to the underlying azimuthal symmetry of the system. Meanwhile, the substantially by eye. amplitude of $|\beta_1|$ is stronger at higher inclinations, as it is sensitive to asymmetries in the polarized image inally, we

highlight the spin dependence of∠β2, which this modeling demonstrates is driven by the evolution of the magnetic field and velocity structure in the GRMHD simulations due to frame dragging (see also Ricarte et al. 2022; Chael et al. 2023; Emami et al. 2023b). The a* = 0 model has $\angle \beta_2 \sim -180^\circ$, corresponding to a very toroidal EVPA pattern and thus radial magnetic fields. Meanwhile, the higher spin models acquire Interestingly, $\angle \beta_2$ remains strikingly stable with inclination, although the overall image structure appears to evolve

This exploration shows that some of the most salient qualitative features of the polarized image can be traced back

Table 2 Summary of the Sgr Å GRMHD Simulation Library Used in This Work

Setup	GRMHD	GRRT	a*	Mode	Γ_{ad}	t _{final}	r _{out}	Resolution
Torus	KHARMA	IPOLE	0, ±0.5, ±0.94	MAD/SANE	$\frac{4}{3} / \frac{4}{3}$	50,000	1000	288 × 128 × 128
Torus	BHAC	RAPTOR	0, ±0.5, ±0.94	MAD/SANE	$\frac{4}{3} / \frac{4}{3}$	30,000	3333	512 × 192 × 192
Torus	H-AMR	IPOLE	0, ±0.5, ±0.94	MAD/SANE	$\frac{13}{9} / \frac{5}{3}$	35,000	1000/200	348/240 × 192 × 192

Note. The last column is N N₂ × N₃, with coordinate x monotonic in radius, x monotonic in colatitude θ, and proportional to longitude f. Times are given in units of t_a and radii in units of r_a. Different settings may be adopted for MAD models compared to SANE orassdenoted by a /.

to fundamental properties of the fluid and spacetime (magnetic field geometry and spin) without necessarily invoking more uncertain aspects of GRMHD models such as Faraday rotatio the electron-to-ion temperature ratio, and the electron distribution function. However, more physically complete calculations with GRMHD simulations that include these effects selfconsistently are still necessary for quantitative comparison.

4. GRMHD Models

While semianalytic models provide qualitative insights and intuition about BH accretion flows, they do not enforce conservation laws or capture time-dependent phenomena such as turbulence and shocks that play a crucial role in determining the detailed system structurehus, we generate dynamical source models using numerical ideal GRMHD simulations. A fluid approximation would appear to conflict with the fact that the rate of Coulomb collisions is small, leading to mean free paths well exceeding the system size, implying that a collisionless kinetic treatment of the plasma may be necessary (Mahadevan & Quataet 997). However, kinetic instabilities can produce small-scale inhomogeneities in the magnetic field that produce an effective collisionality through particle-wave interactions (Kunz et al. 2014; Riquelme et al. 2015; Sironi & Narayan 2015; Meyrand et al. 2019). We implicitly assume that radiative effects like cooling are not dynamically important for the fluid evolution. This assumption is well motivated given the low accretion rate of Sgr Å, M 10 6M Edd, for which the radiative cooling timescale is long compared to the accretion timescale (Dibi et al. 2012; Ryan et al. 2017; Chael et al. 2018; Porth et al. 2019; but see also Yoon et al2020).

In Paper V, to compare with total intensity EHT and multiwavelength constraints, we generated a suite of GRMHD-derived images sampling a range ofinitial conditions and parameterizations of the electron temperature and distribution function. We simplify our exploration in this work, limiting ourselves to simulations with untilted toruslike initial conditions, relativistic thermal electron distribution functions (eDFs) lacking nonthermal contributions, and electron temperatures prescribed via the Mościbrodzkaatt (2016) R – β prescription (see Equation (8) below). The properties of our GRMHD simulations are summarized in Table 2. Radiative transferis integrated within a radius of 100rg, explicitly ignoring material in highly magnetized regions with $\sigma \equiv b^2/\rho > 1$, within which mass density is artificially injected to keep the simulation stable. We briefly cut, and the eDF in Appendices D-F, respectively. While departures from these assumptions are both interesting and

Table 3 Summary of Parameters Sampled by Our GRMHD Libraries

n⊋arameter	Values		
Magnetic field state	MAD, SANE		
a*	-0.94, -0.5, 0.0, 0.5, 0.94		
i (deg)	10, 30, 50, 70, 90, 110, 130, 150, 170		
R _{hiah}	1, 10, 40, 160		
Magnetic field polarity	Aligned, Reversed		

Note. We coarsely sample a five-dimensional parameter space. For each combination of parameters and for each of the KHARMA and BHAC codes, we ray-trace the equivalent of 10 nights of observations.

physically justified, we defer a thorough investigation of these topics to future work.

Our GRMHD library samples a five-dimensionparameter space. The first parameteris the magnetic field state, either an MAD model (Bisnovatyi-Kogan & Ruzmaikin 1976; Igumenshchev et al. 2003; Narayan et al. 2003; Tchekhovskoy et al. 2011) or a standard and normal evolution (SANE) model (De Villiers et al. 2003: Gammie et al. 2003: Naravan et al. 2012; Sądowski et al2013). These describe models in which the magnetic flux threading the horizon for a given accretion rate has saturated and become dynamically import(aMAD) or not (SANE). The second is the BH spin, which we denote as a* ä [- 1, 1], where a negative sign indicates a retrograde disk with respect to the spin vector hird is the inclination, which uniformly samples i ä [0°,180°], instead of only i ä [0°,90°] as probed in Paper V, because Faraday rotation and emission of circular polarization break the symmetry when polarization is considered. Our fourth parameter is Rhigh, which sets the asymptotic value of the ion-to-electron temperature ratio as plasma $\beta \rightarrow \infty$ (Mościbrodzka et al.2016). Specifically,

$$\frac{T_i}{T_e} = R_{\text{low}} \frac{1}{1 + h^2} + R_{\text{high}} \frac{b^2}{1 + h^2},$$
 (8)

where T_i and T_e are the ion and electron temperatures, respectively. While the potential importance of electron cooling for M87* motivated models with cooler electrons = 10, here we only consider R_{low} = 1 owing to the much smaller Eddington ratio of Sgr A. Finally, our fifth parameter is the magnetic field polarity with respect to the angular momentum vector of the disk, either aligned or reversed, which affects the direction of Faraday rotation and the handedness of circularly polarized emission. This last degree of freedom only matters test the impact of our choices of outer integration radius, the σ for polarized radiative transfer and was ignored in Paper V. We produce a library of images for each combination of these parameterstabulated in Table 3.

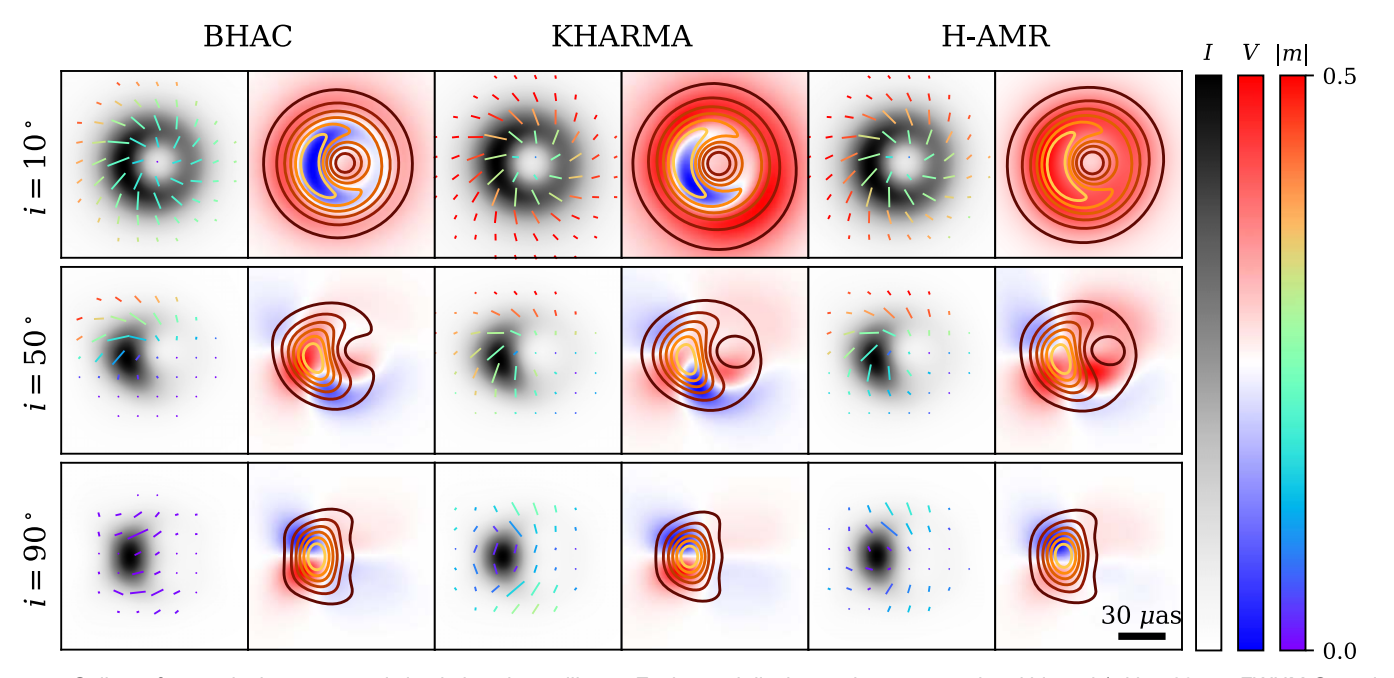


Figure 5. Gallery of example time-averaged simulations in our library. Each panel displays a time-averaged and blurred (with a 20 µas FWHM Gaussian kernel) Ma a* = 0.94, Rhigh = 40 aligned models at three different inclinations. The first panel of each set displays total intensity and linear polarization, while the second panel each setdisplays total intensity and circularpolarization. Tick lengths scale the totalpolarized flux density in a given pixel, while their colors scale with the polarization fractionH-AMR models are ray-traced only for a subset of models for comparison and are not used for scoring.

We retain the use of multiple codes to assessnumerical systematic differences. For scoring, we generate libraries spanning 15,000t ($t_q = r_q/c$), equivalent to about 10 8 hr nights of observation for the parameter combinations listed in an MAD a * = 0.94, R_{high} = 40 aligned field simulation, Table 3 using two code combinations HARMA 158 (Prather et al. 2021) + IPOLE¹⁵⁹ (Mościbrodzka & Gammie 2018) and BHAC⁶⁰ (Porth et al. 2017; Olivares et al. 2019)RAPTOR¹⁶¹ (Bronzwaer et al. 2018, 2020), where the first and second codepolarization. As the inclination grows, the total intensity image in each pair correspond to GRMHD and GRRTespectively. As a further consistency checka third set is generated with H-AMR¹⁶² (Liska et al. 2022) +POLE for a subset of parameter space (only i __ 90°, aligned fields and 5000t) that we do not use for scoring.

Each simulation is initialized with a torus of gas in constant angular momentum hydrodynamic equilibrium (Fishbone & Moncrief 1976). These tori are perturbed with a weak, poloidal along both a horizontal and vertical axis due to flips in the linemagnetic field. The simulations vary in their initial radius of maximum pressure (from ~15rto 40r_g) and adiabatic index, Γ_{ad} Codes differ in their choice of Γ_{ad} because Γ_{ad} = 4/3 applies to a fluid of relativistic electrons angd = 5/3 applies to a fluid of nonrelativistic ions, but only one fluid is evolved in these models. Depending on the torus size and initial magnetic field configuration, the simulations develop into an MAD or SANE state (see,g., Wong et al. 2022).

In Figure 5, we plot a selection of time-averaged GRMHD snapshots from our libraryblurred to EHT resolution using a Gaussian convolution kernel with an FWHM of 20 µas. In the left panel of each setwe plot total intensity in gray scale and the resolved linearpolarization as colored ticks. In the right panel of each set, we plot the circular polarization from blue to

red with total intensity contours. Each panel is individually normalized such that the color maps span from 0 tonthell) on the left and $\max(|\mathbb{I}|)$ on the right. Each of these models is computed with different codes as indicated above.

The codes exhibitagreemenin terms of total intensity and polarized morphology butdiffer somewhatin the degree of becomes more asymmetric owing to Dopplebeaming (e.g., Falcke etal. 2000; Medeiros etal. 2022; Paper V). The same holds true for the polarization, which is further affected by a Faraday depolarization gradient (see Appendix A.3). The magnetic field geometry as sampled by deflected lights is encoded in the image of circular polarization. In particular, edge-on images in circular polarization exhibit sign inversions of-sight magnetic field directionand this signal disappears as the viewing angle decreases (Ricarte et al. 2021; Tsunetoe et al. 2021).

5. GRMHD Model Scoring

We introduce a novel methodology to score each ofour GRMHD models using the eight polarimetric constraints in Table 1. Our new scoring scheme acts on time-averaged GRMHD images and attempts to accommodate variations between codesNote that we only include quantities inferred from our polarimetric images in these constraints we will discuss comparisons with totalintensity and multifrequency constraints derived in Paper V.

1. First, each modeltime series of images is splitinto 10 windows, each with 1500 M duration. Within each window, we produce a time-averaged image by averaging each of the Stokes parameters. Then, we blur the average image with a Gaussian kernel with an FWHM of 20 µas and compute each of the eight observables for scoring.

¹⁵⁸ https://github.com/AFD-Illinois/kharma

¹⁵⁹ https://github.com/moscibrodzka/ipole

¹⁶⁰ https://bhac.science

https://github.com/jordydavelaar/raptor

https://www.matthewliska.com/home-1/project-four-zng9g-rd5bb

Constraints Without $\angle \beta_2$

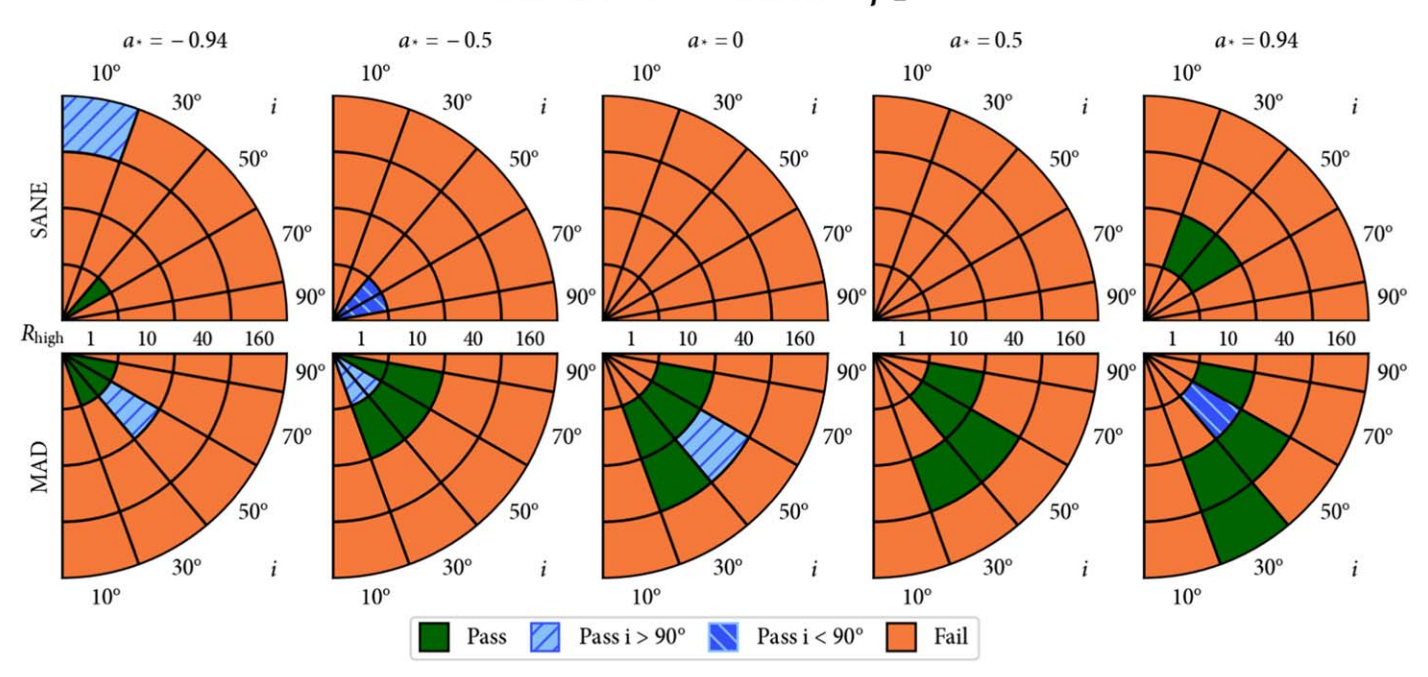


Figure 6. Combined polarimetric constraints on the GRMHD model/brary excluding ∠β2. Orange models fail, green models pass aboth the given and its supplementary angle, and blue regions only pass with the given or supplementary angle as indicated. SANE models are plotted on the top half, and MAD models as plotted on the bottom half. Different columns correspond to different spins from -0.94 to 0.94. Within each wedge, the radial direction corresponded the azimuthal direction corresponds to observer inclination.

- 2. For each combination of parameters, we combine the codes, this results in 20 different samples. From these values, we compute the 90% quantiles¹⁶³ of each observable to capture the time variability.
- 3. A model passes an individual observational constraint if there is overlap between its 90% quantile region and that of the observations. A model passes a set of observational In Figure 6, we plot a pass/fail table combining all constraints if it passes allof the constraints in the set simultaneously.

The most important differences compared to the scoring system utilized in Paper V are that this new system operates opolarity. time-averaged images and combines the results from multiple codes into a single theoretical range. We tested performing scoring using only one simulation set at a time. Since KHARMA model electron temperatures are assigned systematically hotter than those of the BHAC models (see Appendix H), KHARMA passes models with larger Rhigh-There is more disagreement between the codes for SANE models than for MAD models. The constraints with the most disagreemenbetween the two codes are $\angle \beta$, $|\beta_2|/|\beta_1|$, and m_{net} with the KHARMA simulations ruling out more SANE models than the BHAC simulations in each case.

with the underlying physics. For brevity, we defer a pedagogicalexploration of how each of our free parameters

is imprinted onto the observables to Appendix A.We study values of the observables predicted by the KHARMA and how each individual constraint affects model selection in BHAC codes. Since there are 10 windows and two sets of Appendix B. Here we summarize the highest-levelscoring results, first excluding $\angle \beta_2$ and then including $\angle \beta_2$ either as observed or after performing RM derotation.

5.1. Constraints Independent of RM

polarimetric constraints, with the exception of $\angle \beta_2$. These plots combine both polarities of the magnetic fiels howing a pass as long as either polarity passes. These tables are slightly but not systematically different as a function of magnetic field

We find that the tight constraint on $\langle |m| \rangle$ (24%–28%) is the most powerful, driving most of the trends shown in this figure. It is much more constraining on parameter space than for which a much larger range (2.0%–7.3%) is allowed the $|\beta_2|$ constraint rules out a few additional typically edge-on models, but it does not provide too much more additional constraining power because $\langle |m| \rangle$ and $|\beta_2|$ are correlated. Without $\angle \beta_2$, Figure 6 reveals no significant preference between i > 90° and i < 90° models.

While our total intensity constraints generally favored larger values of R_{high} (due largely to multiwavelength constraints; Each of the observational constraints has known connection Paper V), our polarimetric constraints usually prefer more moderate values. This is because larger values, of Rsually lead to larger internal Faraday rotation depths (see Appendix A.4), which is the most important physical driver 163 For ∠β₂, to evade problems with phase wrapping, we translate angles into of depolarization in our models. However, an interesting trend Paper V to continue to pass with R = 160. This is the MAD respectively. This occurs predominantly when a model is so depolarized that it $e^{x} = 0.94$, $R_{high} = 160$, $i = 30^{\circ}/150^{\circ}$ model. MAD models with larger spin have smaller Faraday rotation depths(see

unit vectors in the complex plane centered at 0 before computing 90% quantilewith respect to spin allows one of the best-bet models of and then translate backt the magnitude of the mean of these unit vectors is less than 0.05, we set the lower and upper ranges of tr\$-180° and 180° $\angle \beta_2$ is approximately uniformly distributed.

All Polarimetric Constraints

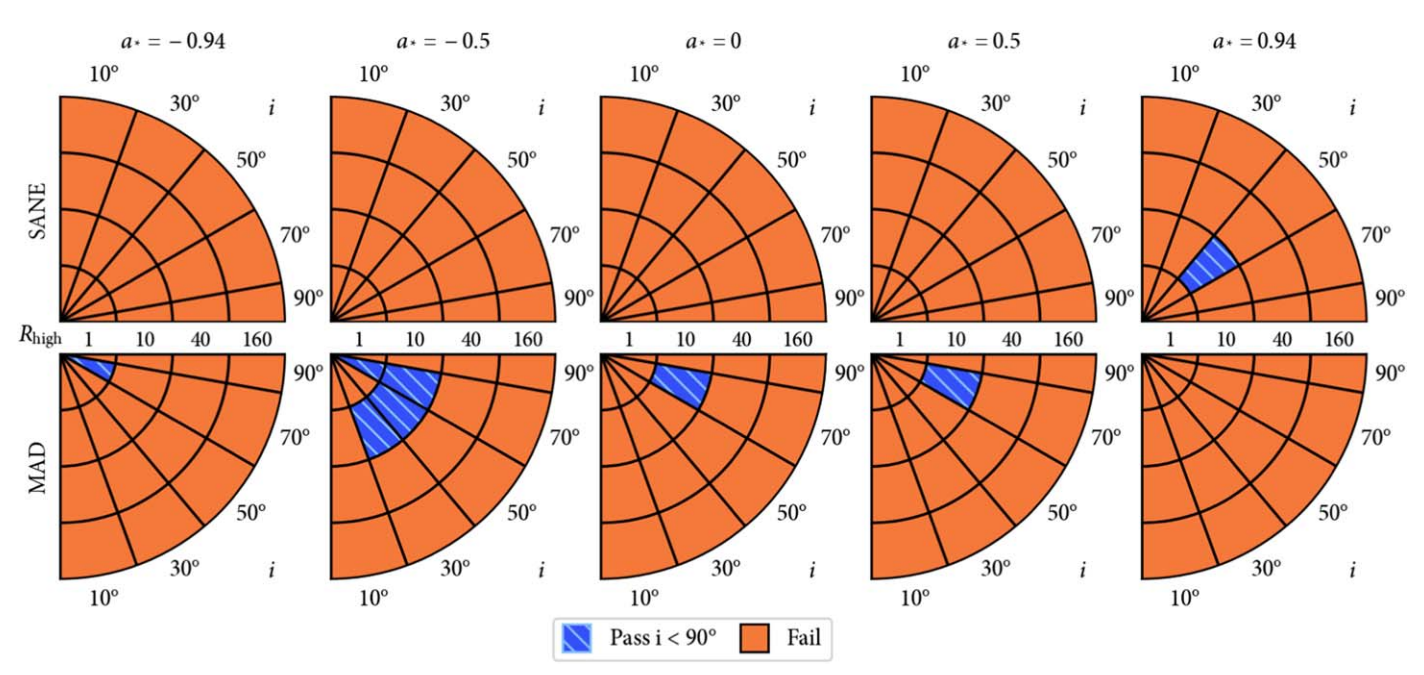


Figure 7. Same as Figure 6, but including the constraint on the phase ith four terms of the phase ith derotation. Only models with counterclockwise motion (i < 90°) pass. There is no model that passes all polarimetric and total intensity constraints utilized in Paper V.

Appendix H), allowing them to pass the $\langle |m| \rangle$ constraintfor larger values of Righ. We refer readers to Appendix B for a more detailed breakdown of each constraint considered individually.

5.2. Constraints Including ∠β without RM Derotation

First, we discuss the ∠β constraint if RM derotation is not performed. It is possible that the RM may be attributed entirely to Faraday rotation captured within our simulation domain. GRMHD models are capable of producing the correct magnitude of RM from Faraday rotation on event horizon scales, but they tend to produce RM sign flips that are not consistentwith decades of Sgr A* observations that produce negative values of the RM (Ricarte et al. 2020; M87 Paper VII; Wielgus et al. 2024). However, it is possible that this problem is related to the excess variability in our models identified in Paper V. We further discuss the uncertainties surrounding our interpretation of the RM in Appendix C.

If one attributes the RM entirely to internal Faraday rotation, then our constraint on $\angle \beta_2$ spans the interval (125°, 160°). Adding this constraint to Figure 6 results in Figure 7. A selection for i < 90° arises because the handednesof the polarization spiral is opposite that of the magnetic field, which inherits the handedness of the inflowing and emitting gas (see value of \acute{a} RM $\~{n}$ = -4.65 $^{\circ}_{1.18}$ $^{\circ}$ 10 $^{\circ}$ rad m $^{\circ}$ has been Section 3.3 and Appendix A.3). This corresponds to counterclockwise motion, which disagrees with hot spot interpretations $24RM\tilde{n}/2 = -92.0^{+24.7}_{23.4}$ deg if this RM is interpreted as an of polarized flares both in the near-IR (NIR; GRAVITY Collaboration et al. 2018, 2020a, 2020b) and in the submillimeter(Vos et al. 2022; Wielgus et al. 2022b). That is, consistency with clockwise motion would require $-180^{\circ} < \angle \beta_2 < 0^{\circ}$ if we assume that $\angle \beta_2$ traces magnetic field lines with outgoing Poynting flux (Chael et al. 2023), which does not agree with the linearly polarized morphology as If one attributes the mean RM of a given day entirely to an observed on the sky.

Without RM derotation, no model can simultaneously pass all total intensity and polarimetric constraint shis is because the a* = 0.94 best-betmodel of Paper V produces an EVPA pattern thatis too radial (see Appendix A.2) All models that pass our polarization constraintsin Figure 7 fail multiple constraints on the total intensity. In particular, all eight models shown in Figure 7 produce too much flux in the infrared to match observation and all but the SANE model at a = 0.94 overproduce the X-ray flux (Paper V). Both of these are serious failures, as both the IR and X-ray fluxes estimated by our models are lower limits owing to our lack of nonthermal electrons and smalbimulation domain relative to the X-rayemitting area. Five of the models additionally fail to match the observed size and flux of the source at 86 GHz (Issaoun et al. 2019). All of these models also fail at least one total intensity structuralconstraint(m-ring and visibility amplitude morphology tests in Paper V). In conclusion, we cannot find a concordance model of Sgr Awithout RM derotation.

5.3. Constraints Including ∠β with RM Derotation

Alternatively, in this section we interpret the mean RM as an external Faraday screen, motivating derotation. As discussed in Section $2, \angle \beta_2$ depends on twice the RM for which a mean obtained. This potentially results in a shift in $\angle \beta_2$ of external Faraday screen. In this picture, a relatively stable external screen explains the constant sign of RM that has been observed for decades (nevertheless with variation on the order of ~10⁵ rad m²). Then, an additional componenton event horizon scales, which is already included self-consistently in our models explains the subhour time variability.

external screen, then our constraint onspans (-168°, -85°).

All Polarimetric Constraints

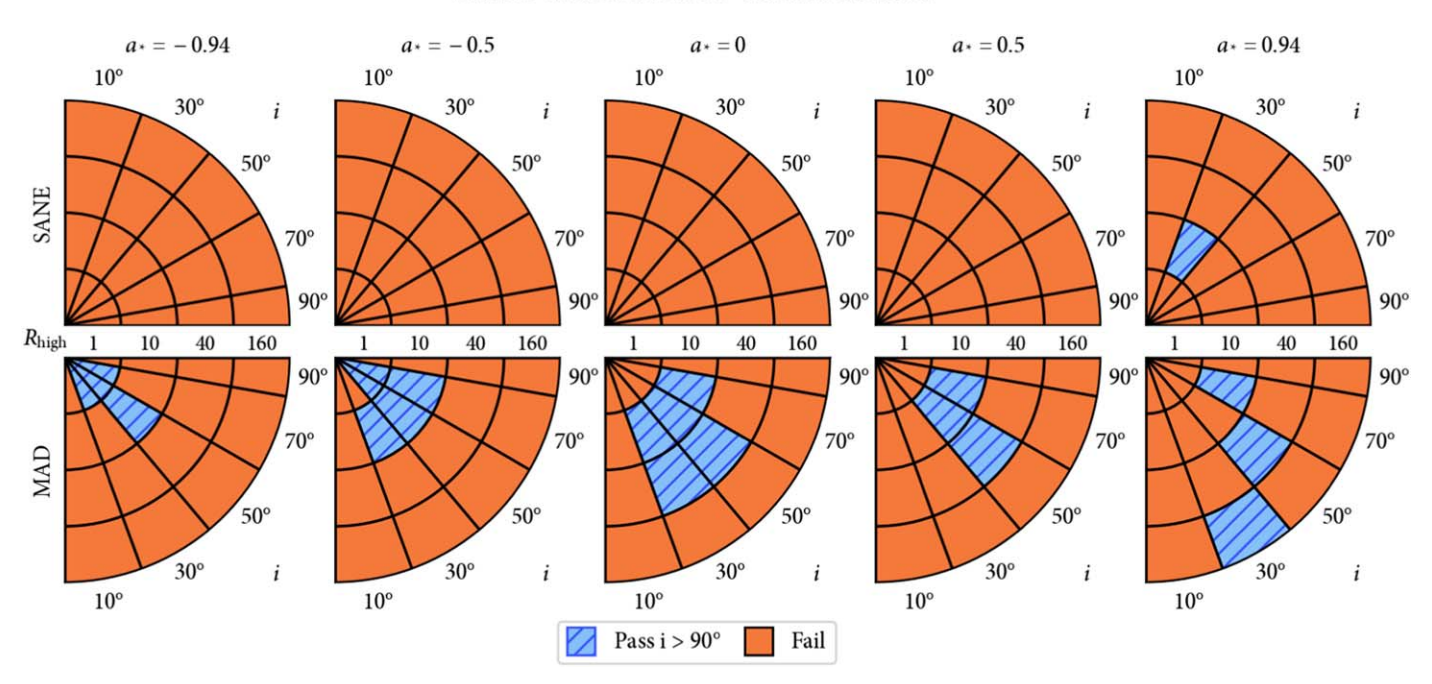


Figure 8. Same as Figure 6, but including the constraint on the phasewith RM derotation. Only models with clockwise motion (i > 90°) pass. A best-bet model from Paper V passes all total intensity and polarimetric constraints: MAD=a0.94, R_{high} = 160, i = 150° aligned.

Adding this constraint to Figure 6 results in Figure 8. Performing more diffuse jet funnel region. Computing an emissionthis cut requires inclination angles >90°, correspondingo clockwise motion on the sky, which now agrees with the

With RM derotation, one of the best-betmodels from our total intensity analysis passes alapplied total intensity and polarimetric constraints. This is the MAD a* = 0.94, R_{high} = 160, i = 150° aligned model. The second best-bet model from Paper V had a * = 0.5 and otherwise identical parameters. This second model passes all constraints except (|m|), which it underproduces by ~3%. In order for the a∗ = 0.94 best-bet model to pass, at least 97% of the measured At a radius of 7.3 g, we compute a mass-weighted average RM must arise from an externascreen. Notably, the best-bet model fails if the smaller RM measured at 86 GHz a few days prior, $(-2.14 \pm 0.51) \times 10^{5}$ rad m⁻² (Wielgus et al. 2024), is instead interpreted as the external screen.

In Figure 9, we visualize the best-bet model (BHAC shown) that survives with RM derotation the left two columns, we plot its full polarimetric image in the style of Figure 5. No blurring is applied in the leftmost column, and a 20 µas FWHM and has an accretion rate of 5 × 90Me yr -1. This model has Gaussian kernels convolved with the image in the second column to approximate EHT resolution his model features a bright photon ring, and in our image without blurring, we omit total intensity contours from the circularpolarization map to reveal a photon ring sign inversion (discussed in Mościbrodzka et al. 2021; Ricarte et al2021).

On the right, we produce a map of the density of the observed emission in the equivalent KHARMA simulation normalized such that its peak value is unity, and it is visualized an ordered, rotationally symmetric EVPA pattern. Through (using Kerr-Schild coordinates). The emission density map is in logarithmic scale with 3 orders of magnitude in dynamic range. Our line of sight is indicated by the green arrow, and a white contour encloses 90% of the total emission. This reveals that while the emission is peaked at small radius near the disk midplane, a substantial fraction of the emission originates from

weighted characteristic emission radius $\circ \ \partial^{x} dV / \partial dV$ where ò is the emission density and x is the radius in cylindrical aforementioned models of polarized NIR and submillimeter flares ordinates, we find x = 7.3. We note that our choices to include only thermal electron distribution functions and cut out regions with $\sigma > 1$ in this work minimize the potential contribution of a jet to the total emission (e.g., Figure 12 of Fromm et al. 2022). A significant jet componentmay be necessaryto reproduce the flat spectral index at these frequencies(Falcke et al. 1993; Falcke & Markoff 2000; Mościbrodzka & Falcke 2013).

> magnetic field strength 26, where the range quoted here corresponds to the 16th to 84th percentile values obtained in the time series. This value agrees reasonably well with the onezone model discussed in Section 3.1, although we note that this value evolves substantially with radiuseaching 67+8 G at a radius of $4r_a$ and 560^{+80}_{80} G at the horizon.

This model produces an outflow power of $4 \times 10^{\circ}$ erg \bar{s}^1 a very large jet efficiency of approximately 150% powered by the Blandford & Znajek (1977) mechanism. Yet despite its efficiently, the jet's power is not high enough to expect global effects on the evolution of our Galaxy (e.gSu et al. 2021).

6. Discussion and Conclusion

The first polarized image of Sgr *Aon event horizon scales exhibits a high resolved polarization fraction of 24%-28% and semianalytic arguments and comparisons to GRMHD simulations, we come to the following conclusions:

1. The large resolved polarization fraction implies that the magnetic field on eventhorizon scales cannobe very tangled on scales smallerthan beam, nor can Faraday

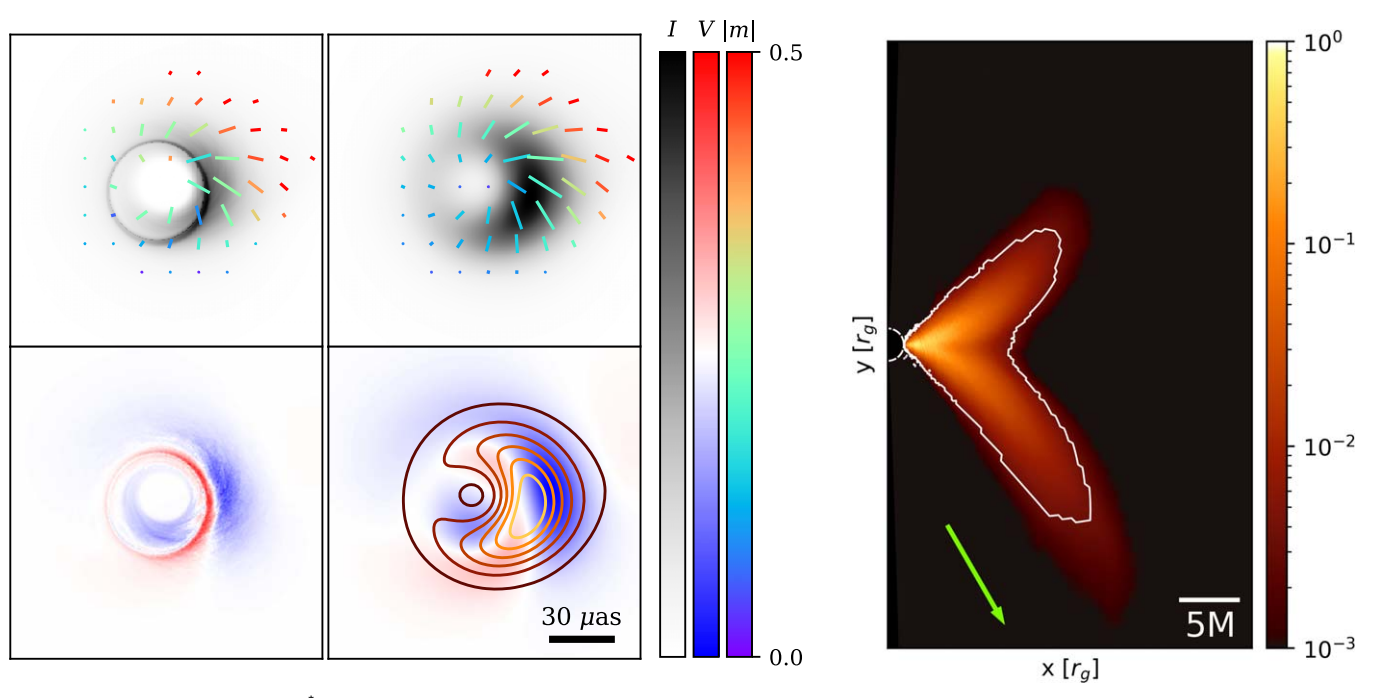


Figure 9. The best-bet model of Sg^*zMAD a* = 0.94, R_{high} = 160, i = 150° aligned. In the left two columns, we plot its simulated image in the style of Figure 5. Images in the first column are unblurred, and images in the second column are blurred with a Gaussian with an FWHM of 20 μ as, approximating EHT resolution. In the right panel, we provide a map of the emission in this model. The white contour encloses 90% of the total emission, the dashed white circle demarcates the horizont the green arrow indicates our viewing angle. While the emission peaks close to the BH in the midplane, a significant fraction of emission originates from a mort diffuse region, including the jet sheath.

rotation add too much additional disorder to the EVPA structure. The disparity between the spatially resolved (24%–28%) and unresolved (2.0%–7.3%) inear polarization fractions can be attributed to cancellations due to the symmetric nature of the image.

- Driven mostly by the spatially resolved polarization fraction, our constraints strongly favor MAD models over their SANE counterparts in M87 Paper VIII.
- 3. If we rely on internal Faraday rotation to produce the observed RM and do not perform derotation, then there is no model that passes altotal intensity and polarimetric constraints.
- 4. On the other hand, if we assume thatthe RM can be attributed to an externascreen and derotate the EVPA pattern, then we find one model that passes allapplied total intensity and polarimetric constraints: MAD a* = 0.94, Rhigh = 160, i = 150° aligned.

While our ideal GRMHD simulations containing only thermal electron distributions have done remarkably wellat reproducing many of the observed quantities of Sgr Athey nevertheless have many known imperfection so of these models overestimate time variability, including the best-bet model (Paper V), and we caution that the values inferred from our best-bet model should not be interpreted as measurements. Known areas where these simulations can be improved include the following:

 Initial Conditions: All of our simulations are initialized with tori that are either perfectly aligned or antialigned with the BH angular momentum axisimulations feeding the BH via stellar winds have different/variability characteristics (Murchikova etal. 2022) and can self-consistently predict an externalFaraday screen (Resslet al. 2019, 2023).

- Tilted disk models (e.g.Fragile et al. 2007; Liska et al. 2018; Chatterjee et al. 2020) may lead to different Faraday rotation characteristicswing to their geometry atlarge radii.
- 2. Electron Thermodynamics: The Mościbrodzka et al. (2016) prescription that we adopt to set the electron temperature broadly captures the trends seen in kinetic simulations that explicitly model heating and cooling (e.g., Chael et al. 2018; Dexter et al. 2020; Mizuno et al. 2021; Dihingia et al. 2023) but does not reproduce them in much detail. More generally, a nonthermal contribution to the electron distribution function is believed to be necessary to reproduce the spectrahergy distribution (Özel et al. 2000; Markoff et al. 2001; Davelaaret al. 2018) and is naturally predicted by particle-in-cell simulations (Kunz et al. 2016; Ball et al. 2018). Nonthermal electron distribution functions can have significantimpacts on both totalintensity and polarized properties (e.g., Markoff et al. 2001; Mao et al. 2017; Davelaaret al. 2018; Cruz-Osorio et al. 2022; Fromm et al. 2022; Paper V) and are a promising avenue to continue theoretical exploration.
- 3. Plasma Composition: Wong & Gammie (2022/demonstrate that models fed by helium rather than hydrogen may have substantially different mission morphologies, tending toward higher temperatures and lower densities and thus higher polarization fractions. Meanwhile, the presence of electron-positron pairs can significantly alter Faraday effects leading to potential signatures in both linear and circular polarization that ave not been fully explored (Anantua et al. 2020; Emami et al. 2021, 2023a; M87* Paper IX).

Several ongoing developments within the EHT will impactful for testing our present interpretation, especially explorations in time and frequency An effort is ongoing to produce dynamical movies of Sgr, Adespite the challenges of very sparse snapshoti,v) coverage (Tiede et al. 2020; Farah et al. 2022; Levis et al. 2023). Measurements of the apparent angular velocity or potentially the motion of hot spots will et al. 2022b; Conroy et al. 2023). The dynamic reconstruction Scholarship; the Consejería de Econología poimiento Empreand geometric modeling of these data by Knollmüller et al. (2023) are consistent with the inferred inclination and clockwise motion of our best-betmodel. On longer timescales (of years), it will be important to obtain averages of quantities such. WheelerChair at PerimetelInstitute; Dirección Generalde as $\angle \beta_2$, which varies little in our models owing to its tight link with BH spin.

In the frequency domainfuture EHT data sets will include 345 GHz data. The wavelength dependence of the scattering screen toward the Galactic center inhibits imaging of SgatA lower frequencies below 86 GHz (Johnson et al. 2018; Issaoun_{1292.19.202)} of the research program the National Science et al. 2019, 2021). On its own, a 345 GHz polarized image would already strongly mitigate one of our largestystematic by a factor of 2, as it is proportional to v. These images will also have intrinsically higherresolution by a factor of 50%. Simultaneous dual-band observations could enable the production nomical Mega-Scienc Chinese Academy Sciences and the tion of RM maps, which would be our best tool for characterizing the Faraday screen and disambiguating our approach to derotation.If the RM truly originates from an external Faraday screen and the emission origin does not significantly change then at 345 GHz we should observe a spatially uniform EVPA rotation of ~20° clockwise relative to our 230 GHz image (roughly halfway between the top two rows in Figure 1). Meanwhile, RM due to internal Faraday rotation may exhibit more spatial variation and potentially sign flips owing to turbulence in the inner accretion flow (Ricarte et al. 2020).

Given the vastness of parameter and modeling space available to theoreticainterpretation, we expect the polarized image of Sgr A to continue to constrain models for many studies to come. This growing EHT data setwill continue to challenge theoretical models and provide insights into the nature of BHs, accretion, and plasma physics.

Acknowledgments

The Event Horizon TelescopeCollaborationthanks the following organizations and progranting Academia Sinicalne Academy of Finland (projects 274477, 284495, 312496, 31572PpstdoctoraFellowship (research atthe Flatiron Institute is the Agencia Nacional de Investigación y Desarrollo (ANID), Chaépported by the SimonsFoundation)the Japan Ministry of via NCN19 058 (TITANs), Fondecyt1221421 and BASAL FB210003the Alexander von Humboldstiftung;an Alfred P. Sloan ResearchFellowship; Allegro, the EuropeanALMA RegionalCentre node in the Netherlandsthe NL astronomy research network NOVA and the astronomy instituted the University of Amsterdam, Leiden University, and Radboud University; the ALMA North America Developmen Fund; the Astrophysics and High Energy Physics program by MCIN (withLeverhulme Trust Early Career ResearchFellowship; the funding from European Union NextGenerationEU, PRTR-C17I1Nax-Planck-GesellschaftPG); the Max Planck Partner Group the Black Hole Initiative, which is funded by grants from the Jolof the MPG and the CASthe MEXT/JSPS KAKENHI (grants Betty Moore Foundation (GrantGBMF-8273)—although the opinions expressed in this work are those of the author and do Research Projects PID2019-108995GB-C22and PID2022necessarily reflect views of these Foundation the Brinson

Foundation: "la Caixa" Foundation (ID 100010434) through fellowship codes LCF/BQ/DI22/11940027 and LCF/BQ/DI22/ 11940030Chandra DD7-18089X and TM6-17006 Me China Scholarship Counciline China PostdoctorScience Foundation fellowships (2020M671266, 2022M712084); Consejo Nacional de HumanidadesCiencia y Tecnología (CONAHCYT, Mexico, projects U0004-2460830004-259839,0003-272050M0037provide additional constraints on spin and inclination (Wielgus 279006, F0003-281692, 104497, 275201, 263356); the Colfuturo sas y Universidad of the Junta de Andalucía (grant P18-FR-1769); the Consejo Superior de InvestigacionesCientíficas (grant 2019AEP112); the Delaney Family via the Delaney Family John Asuntos del Personal Académico-Universidad Nacional Autónoma de México (DGAPA-UNAM, projects IN112820 and IN108324); the Dutch Organization foScientific Research (NWO) r the VICI award (grant 639.043.513), the grant OCENW.KLEIN.113, and the Dutch Black Hole Consortium (with project). NWA Agenda; the Dutch National SupercomputersCartesiusand Snellius (NWO grant 2021.013); the EACOA Fellowship awarded uncertainties, the RM; the total EVPA rotation would decrease by the East Asia Core Observatories Association, which consists of the Academia Sinica Institute of Astronomy and Astrophysics, the National Astronomica Observatory of Japan, Centerfor Astro-Korea Astronomy and SpaceScienceInstitute: the European Research Council (ERC) Synergy Grant "BlackHoleCam: Imaging the Event Horizon of Black Holes" (grant 610058); the European Union's Horizon 2020 research and innovation program under grant agreements RadioNet (No. 730562) and M2FINDERS (No. 101018682); the Horizon ERC Grants 2021 program under grant agreements. 101040021the European Research Courfoit advanced grant "JETSET: Launching, propagation and emission of relativistic jets from binary mergers and across mass scales" (grant No. 884631); the FAPESP (Fundação de Amparo á Pesquisa do Estado de São Paulo) under grant 2021/01183-8; the Fondo CAS-ANID folio CAS220010;the GeneralitatValenciana(grants APOSTD/2018/177 and ASFAE/2022/018) and GenT Program (projectCIDEGENT/2018021); the Gordon and Betty Moore Foundation (GBMF-3561, GBMF-5278, GBMF-10423); the Institute for Advanced Studythe Istituto Nazionale di Fisica Nucleare (INFN) sezione Miapoli, iniziative specifiche TEON-GRAV; the InternationalMax Planck ResearchSchool for Astronomy and Astrophysicst the Universities of Bonn and Cologne: DFG research grant "Jet physics on horizon scales and beyond" (grant No. 443220636); Joint Columbia/Flatiron Education, Culture, Sports, Science and Technology (MEXT; grant JPMXP1020200109); the Japan Society for the Promotion of Science (JSPS) Grant-in-Aid for JSPS Research Fellowship (JP17J08829) pe JointInstitute for Computation undamental Science Japanthe Key Research Program of Frontier Sciences. Chinese Academy of Sciences (CAS, grants QYZDJ-SSW-SLH057, QYZDJ-SSW-SYS008,ZDBS-LY-SLH011); the Templeton Foundation (60477, 61497, 62286) and the Gordon 1816K0090, JP21H01137, JP18H03721, JP18K13594, 18K03709, JP19K1476118H01245,25120007,23K03453),the MICINN 140888NB-C22the MIT InternationaScience and Technology

Initiatives (MISTI) Funds; the Ministry of Science and Technology 1, AYA2016-80889-PPID2019-108995GB-C2PID2020-(MOST) of Taiwan (103-2119-M-001-010-MY205-2112-M-2119-M-001-013,106-2119-M-001-027106-2923-M-001-005. 107-2119-M-001-017107-2119-M-001-020107-2119-M-001-041, 107-2119-M-110-005,07-2923-M-001-009,08-2112-M-M-001-025.109-2124-M-001-005109-2923-M-001-001110-2112-M-003-007-MY2110-2112-M-001-03310-2124-M-001-Aeronautics and Space Administration (NASA, Fermi Guest Investigator grant 80NSSC20K1567, NASA Astrophysics TheoResearch Chairsnitiative, through the South African Radio Program grant 80NSSC20K0527,NASA NuSTAR award contractNAS5-26555the Nationalnstitute of NaturaSciences (NINS) of Japanthe NationalKey Research and Development Program of China (gran2016YFA04007042017YFA0402703, (NSTC, grants NSTC 111-2112-M-001-041, NSTC 111-2124-Mand the YCAA Prize Postdoctoral Fellowship. Foundation (NSF grants AST-0096454 AST-0352953 AST-0521233,AST-0705062AST-0905844AST-0922984AST-1126433,OIA-1126433,AST-1140030,DGE-1144085,AST-1207704, AST-1207730, AST-1207752, MRI-1228509, OPP-1248097,AST-1310896,AST-1440254,AST-1555365,AST-1614868,AST-1615796,AST-1715061,AST-1716327,AST-1726637,OISE-1743747,AST-1743747,AST-1816420,AST-1952099, AST-1935980, AST-2034306, AST-2205908, AST-2307887); NSF Astronomy and Astrophysics Postdoctoral Fellowship (AST-1903847the NaturalScience Foundation of China (grants1165011042710625314,11721303,11725312, 11873028, 11933007, 11991052, 11991053, 12192220, 12192223,12273022,12325302,and 12303021),the Natural Sciences and Engineering Research Council of Canada (NSER@pan (NAOJ). The NRAO is a facility of the NSF operated including a Discovery Grant and the NSERC Alexander Graham BellCanada Graduate Scholarships-DocRoragram); the National Youth Thousand Talent Program of China; the National ResearchFoundation of Korea (the Global PhD Fellowship Grantgrants NRF-2015H1A2A1033752e Korea Research Fellowship Program: NRF-2015H1D3A1066561, BraffeDER infrastructure, with project code IDIFEDER-2021-Pool Program: 2019H1D3A1A01102564,Basic Research SupportGrant 2019R1F1A105972 2021R1A6A3A01086420. 2022R1C1C1005255, 2022R1F1A1075115) Netherlands Research School Astronomy (NOVA) Virtual Institute of Accretion (VIA) postdoctorafellowships; NOIRLab, which is managed by the Association of Universities for Research in Astronomy (AURA) under a cooperative agreementith the NationalScience Foundatio@nsala Space Observatory (OSO) national infrastructure for the provisioning of its facilities/ observational support (OSO receives funding through the Swe@dsservatory (Swederl)he SMA is a joint projectbetween the for Theoretical Physics (research at Perimeter Institute is supparted the Academia SinicaThe JCMT is operated by the East by the Governmentof Canadathrough the Departmentof Innovation, Science and Economic Development and by the Province of Ontario through the Ministry of Research, Innovation incomplete National Key Research and Development and Science);the Princeton Gravity Initiative; the Spanish

117404GB-C21); the University of Pretoria for financial aid in the 001-025-MY3, 105-2119-M-001-042, 106-2112-M-001-011, 106 yovision of the new Cluster Server nodes and SuperMicro (USA) for a SEEDING GRANT approved toward these nodes in 2020: the Shangha Municipality orientation program of basic research for international scientists (grant No. 22JC1410600); the Shanghai 001-048, 108-2112-M-001-051, 108-2923-M-001-002, 109-2112 Hot Program for Basic Resear Chinese Academy of Science, ShanghaBranch (JCYJ-SHFY-2021-01th) State Agency for Research of the Spanish MCIU through the "Center of Excellence 007, and 110-2923-M-001-001); the Ministry of Education (More-evero Ochoa" award for the Instituto de Astrofísica de Andalucía of Taiwan Yushan Young Scholar Program; the Physics Divisio(SEV-2017-0709); the Spanish Ministry for Science and Innova-National Center for Theoretical Sciences of Taiwan; the National Center for Taiwan; the Nation 501100011033; the Spinoza Prize SPI 78-409; the South African Astronomy Observatory (SARA@rantID 77948), which is a 80NSSC20K0645); NASA Hubble Fellowship grants HST-HF2-facility of the National Research Foundation (NRF), an agency of 51431.001-A and HST-HF2-51482.001-A awarded by the Spacke Department of Science and Innovation (of South Africa: Telescope Science Institute, which is operated by the Associatible Toray Science Foundational Swedish Research Council of Universities for Research in Astronomy, Inc., for NASA, undelvR); the UK Science and Technology Facilities Cou(ggriant No. ST/X508329/1); the US Department Energy (USDOE) through the Los Alamos National Laboratory (operated by Triad National Security, LLC, for the National Nuclear Security 2016YFA0400702); the National Science and Technology Counced ministration of the USDOE ontract 89233218CNA000001); 001-005NSTC 112-2124-M-001-014); the US National Science We thank the staff at the participating observatories,

correlation centers, and institutions for their enthusiastic support. This paper makes use of the following ALMA data: ADS/JAO.ALMA#2016.1.01154.V. ALMA is a partnership of the European Southern Observatory (ESO; Europe, representing its member states NSF, and National Institutes of Natural Sciences of Japatogether with National Research Council (Canada), Ministry of Science and Technology (MOST; Taiwan), Academia Sinica Institute of Astronomy and Astrophysics (ASIAA; Taiwan), and Korea Astronomy and Space Science Institute (KASI; Republic of Korea), in cooperation with the Republic of Chile. The Joint ALMA Observatory is operated by ESO, Associated Universities, (AUI)/NRAO, and the National AstronomicaDbservatory of under cooperative agreement by AUI. This research used resources of the Oak Ridge Leadership Computing Facility at the Oak Ridge National Laboratory, which is supported by the Office of Science of the U.S. Department of Energy under contract No. DE-AC05-00OR22725: the ASTROVIVES 086; and the computing cluster of Shanghai/LBI correlator supported by the Special Fund for Astronomy from the Ministry of Finance in China. We also thank the Centerfor Computational Astrophysics, National Astronomical Observatory of Japan. This work was supported by FAPESP (Fundacao de Amparo a Pesquisa do Estado de Sao Paulo) under grant 2021/01183-8.

APEX is a collaboration between the Max-Planck-Institut Radioastronomie German), ESO, and the Onsala Space Research Council under grant 2017-00648); the Perimeter Inst AP and ASIAA and is funded by the Smithsonian Institution Asian Observatory on behalf of the NAOJ, ASIAA, and KASI, as well as the Ministry of Finance of Chin&hinese Academy of Program (No2017YFA0402700) of China and Natural Science Ministerio de Ciencia e Innovación (grants PGC2018-098915-E-oundation of China grant 11873028. Additional funding support for the JCMT is provided by the Science and Technologies JCMT EHT stations are located, has for the indigenous Facility Council (UK) and participating universities in the UK and awaiian people. Canada. The LMT is a project operated by the Instituto Nacional Software: eht-imaging (Chael de Astrófisica, Óptica, y Electrónica (Mexico) and the Universit(Harris et al. 2020), Scipy (Jones et al. 2001), Pandas of Massachusetts at Amherst (USA). The IRAM 30 m telescop

€McKinney 2010), Astropy (The Astropy Collaboration on Pico Veleta, Spain, is operated by IRAM and supported by CNRS (Centre Nationade la Recherche Scientifiquerance). MPG (Max-Planck-Gesellschaftermany) and IGN (Instituto Geográfico Nacional, Spain). The SMT is operated by the Arizofraather etal. 2021), BHAC (Porth etal. 2017; Olivares etal. Radio Observatorya part of the Steward Observatory of the University of Arizonawith financial support of operations from the State of Arizona and financiasupportfor instrumentation development from the NSF. Support for SPT participation in the EHT is provided by the National Science Foundation through award OPP-1852617 to the University of Chicago. Partial support is also provided by the Kavli Institute of Cosmological Physics at Using our GRMHD models, we explore a five-dimensional the University of Chicago. The SPT hydrogen maser was provided on loan from the GLT, courtesy of ASIAA.

Environmen(XSEDE), supported by NSF gran&CI-1548562, and CyVerse, supported by NSF grantsDBI-0735191,DBI-1265383, and DBI-1743442. XSEDE Stampede2 resourcet TACC was allocated through TG-AST170024 and TG-AST080026NXSEDE JetStream resource & TI and TACC was allocated through AST1700278his research is partif the Frontera computing projeat the Texas Advanced Computing Center through the Frontera Large-Scale Community Partnershipar the horizon than their MAD counterparts at a given allocation AST20023Frontera is made possible by National Science Foundation award OAC-1818253. This research was using services provided by the OSG Consortium (Pordest.et 2007; Sfiligoi et al. 2009) supported by the NationaScience Foundation award No2030508 and 183665Additionalwork used ABACUS2.0, which is part of the eSciencecenter at Southern Denmark University, and the Kultrun Astronomy Hybrodon, M87* Paper IX). Our SANE models are also colder Cluster (projects Conicyt Programa de Astronomia Fondo QuimpaperV), which further increases the efficiency of Faraday QUIMAL170001, Conicyt PIA ACT172033, Fondecyt Iniciacion rotation (Jones & O'Dell 1977; Quataert & Gruzinov 2000) 11170268, Quimal 220002). Simulations were also performed on In Figure 10, we explore the differences between our MAD the SuperMUC cluster at the LRZ in Garchiog, the LOEWE cluster in CSC in Frankfurt, on the HazelHen cluster at the HLR angled fields. In the top panels, we plot the time-averaged in Stuttgart, and on the Pi2.0 and Siyuan Mark-I at Shanghai JirriaRMA images in total intensity and linear polarization, Tong University. The computer resources of the Finnish IT Certiterred to a resolution of 20 µas. In the bottom panels, we for Science(CSC) and the Finnish Computing Competence Infrastructure (FCCI) project are acknowledged. This research magion, Faraday rotation depth, and β₂. In these and the enabled in part by support provided by Compute Ontario (http://following plots in this section, we display theoretical error and Compute Canada (http://www.computecanada.ca).

from Xilinx Inc., under the Xilinx University Program. The EHTC has benefited from technology shared under opensource license by the Collaboration for Astronomy Signal Processing and ElectronicsResearch (CASPER). The EHT project is grateful to T4Science and Microsemi for their assistance with hydrogen maseithis research has made use of NASA's Astrophysics Data System. We gratefully acknowledge the support provided by the extended staff of the ALMA, $(\langle |v| \rangle)$ owing to Faraday conversion (M87aper |X). Palumbo from the inception of the ALMA Phasing Projecthrough the observational campaigns of 2017 and 201/8e would like to thank A. Deller and W. Brisken for EHT-specific support with the use of DiFX. We thank Martin Shepherd for the addition of extra features in the Difmap software thatvere used for the CLEAN imaging results presented in this paper acknowledge the significance that Maunakea, where the SMA and

et al. 2016), Numpy et al 2013, 2018), Jupyter(Kluyver et al. 2016), Matplotlib (Hunter 2007), THEMIS (Broderick et al. 2020), IPOLE (Noble et al. 2007; Mościbrodzka & Gammie 2018), KHARMA 2019), H-AMR (Liska et al. 2022), RAPTOR (Bronzwaer et al. 2018, 2020), KerrBAM (Palumbo et al. 2022).

Appendix A Key Trends: Bridging Theory and Observations

parameter space, constrained by eight observable aspects of the polarized image that we believe are tied to the models in This work used the Extreme Science and Engineering Discoverysically understood ways. Below, we highlight the most sallent trends in our simulated image library to explain their physical origins. We focus on illustrative examples in this appendix, but we provide exhaustive distributions of observables calculated from our GRMHD models in Appendix H.

A.1. Magnetic Field State

By construction, SANE models have weaker magnetic fields accretion rate. As a result, once the fluid is rescaled to Perfoduce the observed millimeter flux, SANE models usually have larger mass densitie his translates directly to a larger Faraday rotation depth, which is directly implicated for scrambling/depolarizing EHT model images (Mościbrodzka et al. 2017; Jiménez-Rosales & Dexte2018; Ricarte et al. and SANE models with fixed*a= 0.5, Rhigh = 40, i = 50° and compare differences in resolved linear and circular polarization computeontario.ca), Calcul Quebec (http://www.calculquebec.ga)nges that are calculated based on differences between codes, time variability, and nearest neighbors in parameter space. The The EHTC has received generous donations of FPGA chips details of how these theoreticaerror bars are calculated are provided in Section 5.

Here we see thatthe SANE model has much lower linear polarization fraction ($\langle |m| \rangle$ and \mathfrak{B} , which can be attributed to a much larger Faraday depthá(r, n). 164 Much larger Faraday depths in SANE models than their equivalent MADs drive most of the differences between these two classes of models. SANE models can also produce larger circular polarization et al. (2020) showed that ∮βis a strong discriminant between MAD and SANE models of M87*. As expected, $|\beta_2|$ is significantly larger for the MAD model than for the SANE

¹⁶⁴ Faraday rotation depth is obtained by integrating the radiative transfer coefficient of Faraday rotation, along each geodesiand then performing an intensity-weighted average across the image (see, M87* Paper VIII).

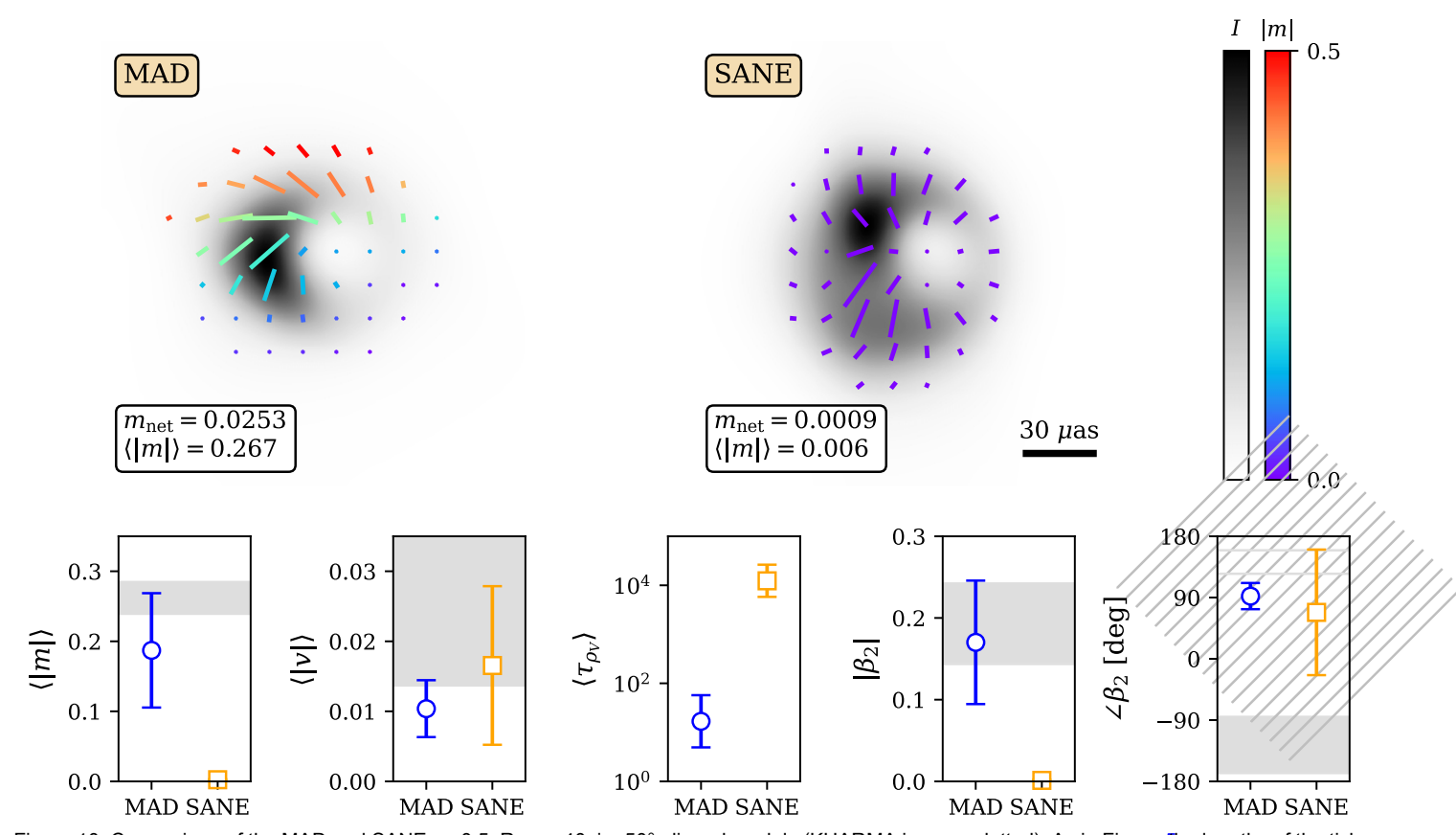


Figure 10. Comparison of the MAD and SANE a= 0.5, Rhigh = 40, i = 50° aligned models (KHARMA images plotted). As in Figure 5 he lengths of the ticks scale with the polarized flux in each pixel, normalized for each model individually. A selection of polarimetric observables are shown with theoretical error bars, alo with our observational constraints in gray. The constraint on prifer to RM derotation is shown with a hatched band instead of a filled band. With other parameters held fixed, SANE models typically have lower resolved linearpolarization owing to higher Faraday depths and can sometimes reach large values outfoular polarization.Large Faraday depths in SANEs result in lower values of (|m|) and |β

model. Interestingly, while SANE models of M87* usually exhibit $\angle \beta_2 \sim 0$, corresponding to radia EVPA patterns, the EVPA pattern in this SANE model acquires some twist owing to a tilted forward jet that we view in projection (top left).

A.2. Spin

The BH spin is a particularly interesting quantity to constrain spot model that favors a relatively face-on viewing angle owing to implications for its cosmic assembly and feedback processesA number of EHT-related studieshave recently explored signatures of spin, and resolved linearpolarization structure has been shown to be one of the most promising andits environment. accessible probe Palumbo et al. 2020; Chael et al. 2023; Emami et al.2023b; Qiu et al.2023; Ricarte et al2023).

In Figure 11, we plot the phase and amplitude of β as a function of spin for the subsetof the MAD R_{high} = 10, i = 30°/150° reversed models. The outer accretion disk rotates counterclockwise on the sky for i = 30° and clockwise on the sky for i = 150°, which is reflected by the sign of $\angle \beta_2$ (or rather, the sign of its imaginary component) As discussed in Section $3.3, \angle \beta_2$ evolves with spin owing to frame dragging, which results in changes in the magnetic field and velocity structure (Palumbo et al. 2020; Event Horizon Telescope Collaboration et al. 2021b; Ricarte et al. 2022; Chael et al. 2023; Emami et al. 2023b; Qiu et al. 2023). The mosthighly spinning prograde models acquire a strong azimuthal magnetic 2 90° for i < 90° and 2 92° for i > 90°. Finally, 2 10° for i > 90°. field componentresulting in more radial EVPA patterns (48) closer to 0°). Finally, \(\begin{aligned} \beta \ is stronger for symmetric and ordered \end{aligned} \)

progrades than fortheir messierretrograde counterparts (see also Qiu et al.2023).

A.3. Inclination

The inclination of Sgr Å is of particular interest because its polarized flaring activity can be interpreted with a polarized hot (GRAVITY Collaboration et al. 2020a, 2020b; Wielgus et al. 2022b). In addition, it is of interest whether or not the accretion disk or BH angular momentum axes align with any structure in

Inclination is imprinted on the polarized image in a variety of ways, and we plot most of our polarimetric observables as a function of inclination in Figure 12. Here MAD a* = 0.94, R_{high} = 10 models are considered. These models produce rotationally symmetric images when viewed face-and thus cancellation leads to opposite behavior of n_{p} and $\langle |m| \rangle$, the latter of which decreases with inclination owing to Faraday depolarization Intuitively, $|\beta_2|$, the amplitude of the rotationally invariant mode, is strongest for face-on viewing angles and weakestfor edge-on viewing angles. Meanwhile, the asymmetric β₁ mode has the largest amplitude for intermediate inclinations. The handedness of the linear polarization spiral is directly encoded in $sign(Im(b_2))$, and thus we see that sensitive to whether the poloidal field is pointed toward us or away from us, but note that it is not perfectly antisymmetric

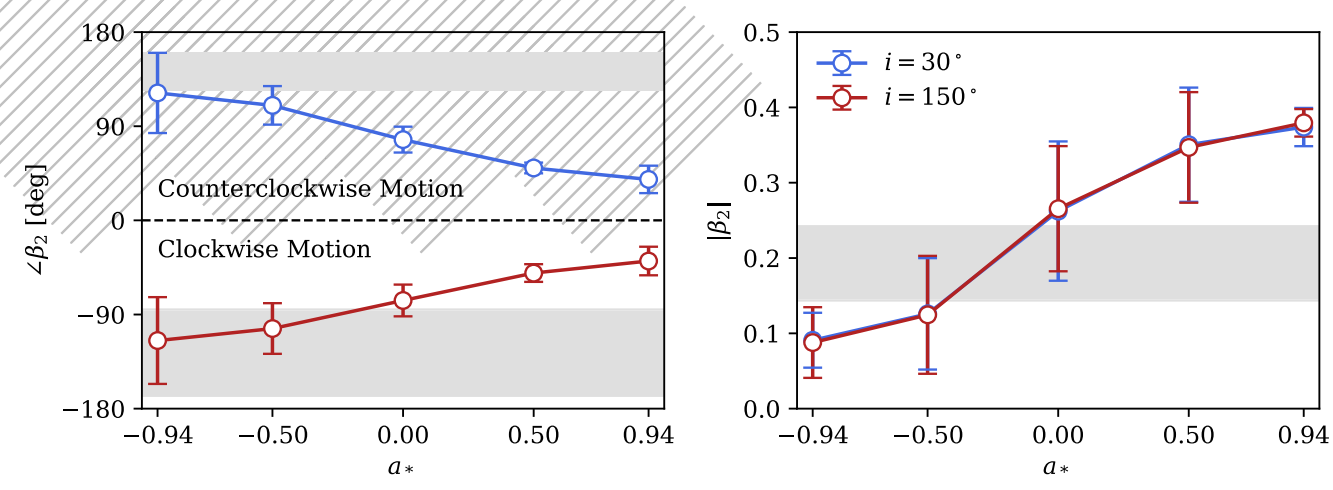


Figure 11. Rotationally symmetric linear polarization structure as a function of spin, encapsulated in the phase and ampliturate this plot, MAD R high = 10, i = 30°/150° reversed models are included, with either i = 30° in blue or i = 150° in red. Our observational constraints are shown as gray bands, and the constraint prior to RM derotation is shown as a hatched region. In this slice of parameter space, prograde models with spin values that are too large tend to produce polariza patterns that are too azimuthally symmetric and radially oriented compared to our observations.

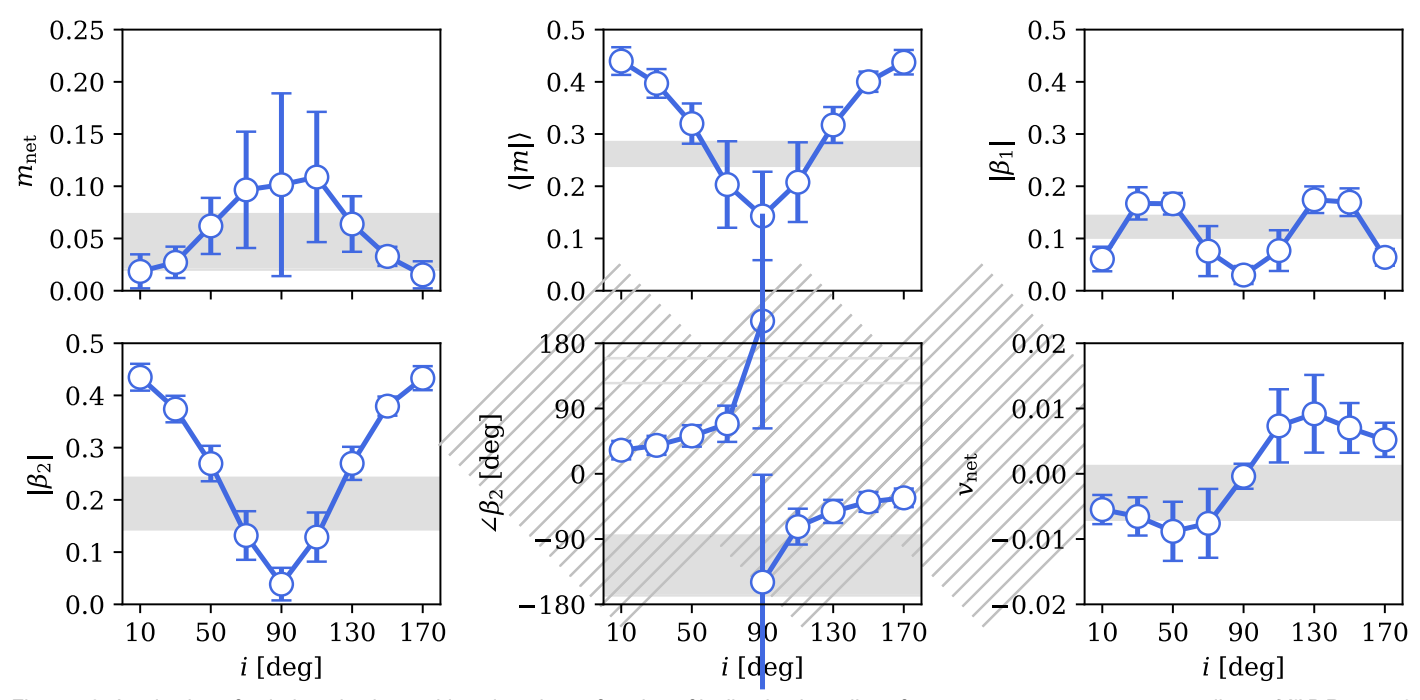


Figure 12. A selection of polarimetric observables plotted as a function of inclination in a slice of our parameter space corresponding to MAND Barich = 10 reversed models. In very ordered models such as this one, symmetry and cancellation lead to the smallest net linear polarization fractions for face-on viewing angl the same time that the resolved linear polarization fraction is highest. In this medelcades the direction of motion, and encodes the direction of the magnetic field with respect to the line of sight.

(Ricarte et al.2021).

A.4. R_{high} (Electron Temperature)

As described in Section 4, R_{high} sets the ratio of ion-to-electron temperature as plasma $\beta\to\infty$ (Mościbrodzka ełal. 2016). Increasing R_{sh} while fixing all other parameters makes the electrons of a given model cooler and less efficient emitters everal of their linear polarization observables. Increasing Thus, models with larger hand to have larger values of when rescaled to achieve the same targeflux. As a result, increasing Righ indirectly increases the Faraday rotation depth (Mościbrodzka etal. 2017; Jiménez-Rosales & Dexter 2018;

about i = 90° owing to contributions from Faraday conversion Ricarte et al. 2020; M87* PaperVIII). Increasing Righ also shifts emission away from the midplane and concentrates it toward the jet funnel region (Paper V; Wong et al. 2022). This effect is much weaker for MADs than for SANEs, since MAD models intrinsically have smaller plasma β on horizon scales.

> In Figure 13, we plot time-averaged BHAC MAD*a= 0.5, i = 130° aligned field models as a function of R_m as well as Faraday depolarization explains the declines in ⟨|m|⟩ anຝ||β with R_{high}. The polarization grows more asymmetric as_{high} increases, because at this inclination the Faraday thick midplane is at the top half of the imageThis, combined with

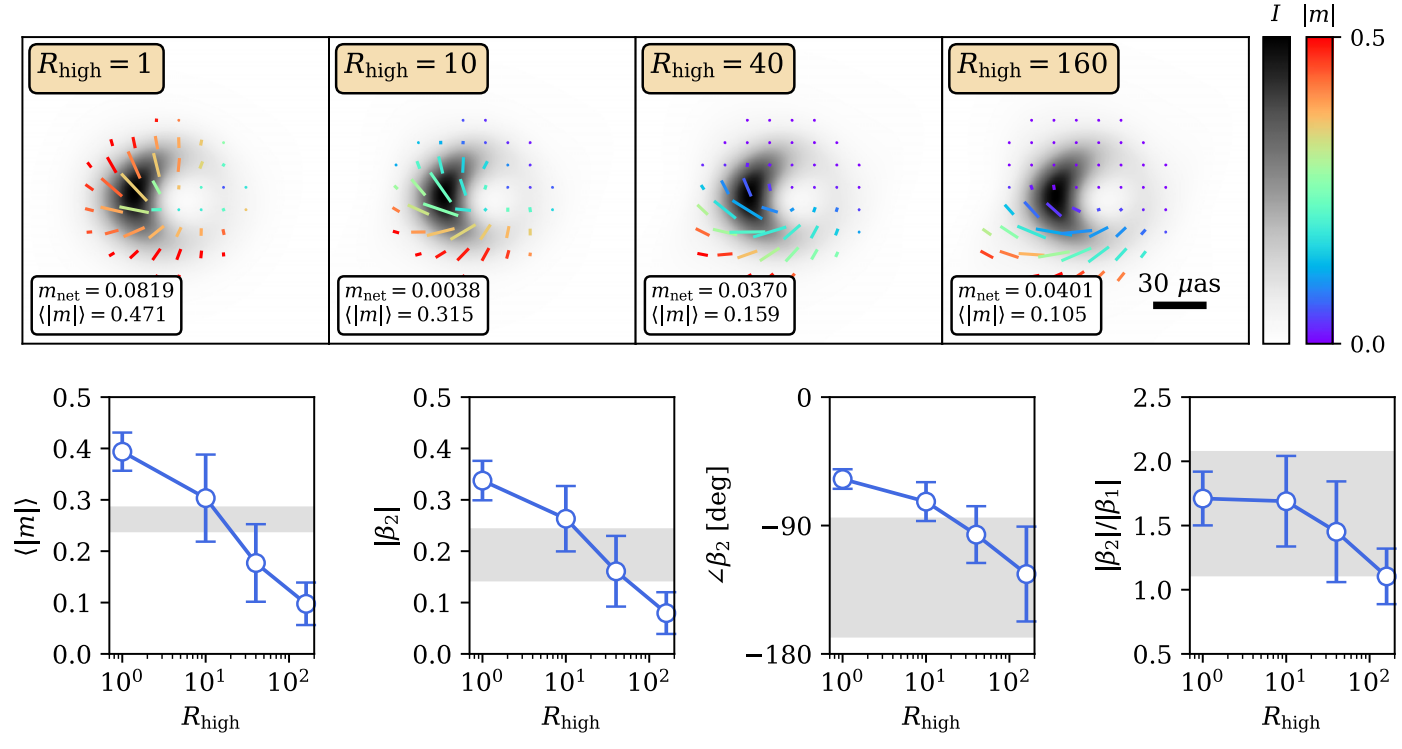


Figure 13. Time-averaged images and a selection of polarimetric observables as a function of the slice of our parameter space corresponding to MAD a* = 0.5, i = 130° aligned models (BHAC images plotted). In this slice of parameter space, Faraday rotation has a clear effect, since ingressing the smaller linear polarization fractions and correspondingly [At this inclination, sight lines at the top of the image pass through the Faraday thick-disk midplane, increasing the polarization asymmetry as [At this inclination] B 1. Both line-of-sight Faraday rotation and changing emission regions lead to a tread in 2β

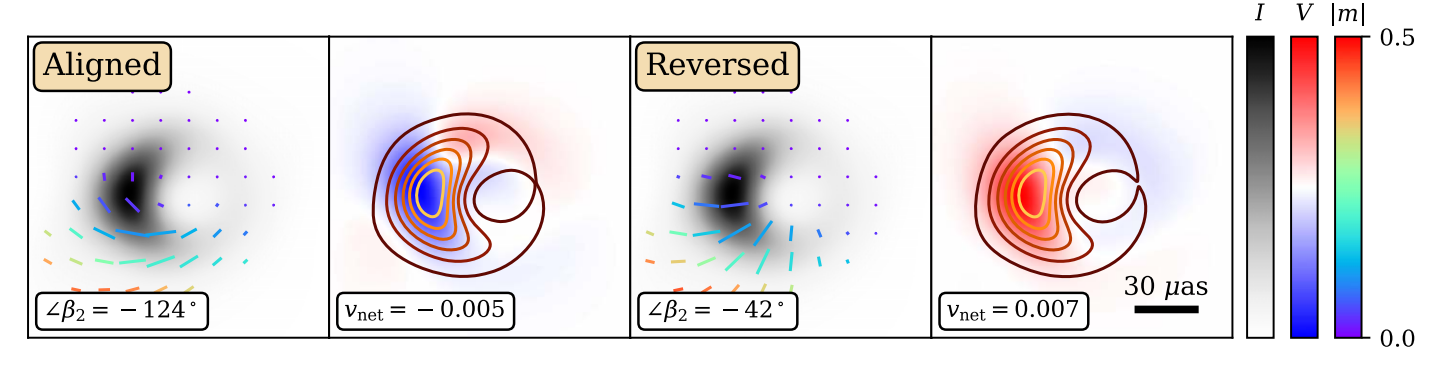


Figure 14. Impact of reversing the polarity of the magnetic field on the time-averaged KHARMA MAD=R160, a* = 0.5, i = 130° model. In radiative transfer, the handedness of Faraday rotation and intrinsic circularly polarized emission flip sign when the magnetic field flipped. This can lead to changes in the morphologi of both linearly and circularly polarized images.

increased Faraday rotation that slightly turns ticks clockwise, \$^{165}\$ leads to a shift in $\angle \beta$. In addition, $|\beta_2|/|\beta_1|$ decreases as the polarization grows more asymmetric.

A.5. Magnetic Field Polarity

In ideal GRMHD, the equations governing the evolution of a magnetized fluid are invarianto a sign flip of the magnetic field direction. However, the equations of GRRT are not, leading to potential polarimetric signatures of the poloidal field direction. When performing radiative transfer, j_V (intrinsic circular polarization of emitted radiation) and ρ_V (Faraday rotation) are each sensitive to the direction of the field with

respectto the photon wavevector. The historically negative Stokes V of Sgr Å is suggestive of a magnetic field oriented away from us. However, MåPaper IX discusses how flipping the magnetic field direction can have nontriviaffects on the circularly polarized image (beyond a simple sign flip) and noticeable effectson $\angle \beta_2$ due to Faraday effects (see also Ricarte et al 2021: Emani et al 2023b)

In Figure 14, we highlight the differences between aligned and reversed field models for the time-averaged KHARMA MAD a \star = 0.5, R_{high} = 160, i = 130° models. Each modelis blurred with a 20 µas FWHM Gaussian beam shown in total intensity and linear polarization ticks on the left and circular polarization and total htensity contours on the rightwe write $_{\rm Z}\beta_{\rm 2}$ and $_{\rm Yhet}$ for each model in the lower left corner evealing significant and unpredictable differences, motivating independent

 $[\]overline{^{165}}$ For an aligned field model with i > 90°, the poloidal field is pointed away from us, leading to a systematic clockwise shift.

ray-tracing for each magnetic field polarity. In linear polarizations ubstantially lower (and less consistent with the light curve) in the difference comes from reversing the direction that aday rotation shifts the EVPA pattern. The magnitude of this effect istighter met constraintfrom THEMIS had been adopted on its larger than that reported in Maraper IX because Maraped in Maraped IX are oriented almost completely face-on, viewed through an evacuated funne(Ricarte et al. 2020). Models of Sgr A can accumulate largeFaraday rotation depths as radiation passes through more of the disk at larger inclinations. In circular polarization, this particular model is mostly characterized by anGRMHD models produce (|v|) lower than the upper limit overall sign flip, but this is not uniform across the image, leadingsimilar to M87* Paper IX). Our constraint on vnet is also not to a small difference in Yet This is because the coefficient Faraday conversion, which exchangeslinear and circular polarization, is invariant to a sign flip in the magnetic field direction.

Appendix B Impacts of Individual Observational Constraints

In Section 5, we included a limited selection of plots reflecting which of our models passed each of the polarimetric constraining as most models naturally produce $\beta > \beta_1$, in observationabonstraints on Sgr A Here we break down the impact of each constraint individually.

In Figure 15, we plot the impact of our (|m|) constraint, which we find is the most important for model selection. precisely and the two methods agree very well he Faradav rotation depth explains the trends in this figure (see Appendix H). More Faraday depolarization tends to occur if R_{high} is larger, if the inclination is larger, or if the model is SANE. Of the models that fail the (|m|) constraint, most are toolikely to fail, such as face-on prograde MAD models (see depolarized, but some lown Rh, high-spin, face-on models are ruled out for predicting values of (|m|) that are too large. We find that \(|m| \) is much more constraining than (Figure 16), which is measured much lessprecisely. Recall that mnet is

the m-ring model than HEMIS. We find that if the higher and own, then this would have ruled out many face-on models (explained in Section 3.3 and Appendix A.3), including the a* = 0.94 best-bet model.

Our circular polarization constraints are not very impactful. Our upper limit on $\langle |v| \rangle$ rules out no models (Figure 17), as all very impactful (Figure 18), but while not visible with our plotting schemeit does rule out many retrograde models that have aligned fields. These models produce preferentially positive v_{net} while decades of Sgr A* observations produce $v_{net} < 0$.

Our constraints on $|\beta|$ (Figure 19), $|\beta_2|$ (Figure 20), and $|\beta_2|/|\beta_1|$ (Figure 21) are impactful, but they are correlated with each other and (|m|). Compared to (|m|), || **8** dditionally rules out some i = 90° models. The ratio $|\beta_2|/|\beta_1|$ is not very agreementwith the observations. While some methods in Paper VII produced ratios up to ~5, which would have pushed our selection toward more face-on inclinations, the two methods retained in this paper produced more modestues. Compared to the other constraints, $\langle |m| \rangle$ is measured relatively Interestingly, a few face-on models are ruled out for being too dominated by the rotationally symmetric mode.

> Finally, we consider the effect of ∠βboth with and without RM derotation in Figures 22 and 23, respectively. In either case, models with preferentially radial EVPA patterns are most Appendix A.2). With derotation, this constraint produces a preference for clockwise motion on the sky (i > 90°). Without derotation,the opposite is trueand more models faibutright since the constraint is tighter.

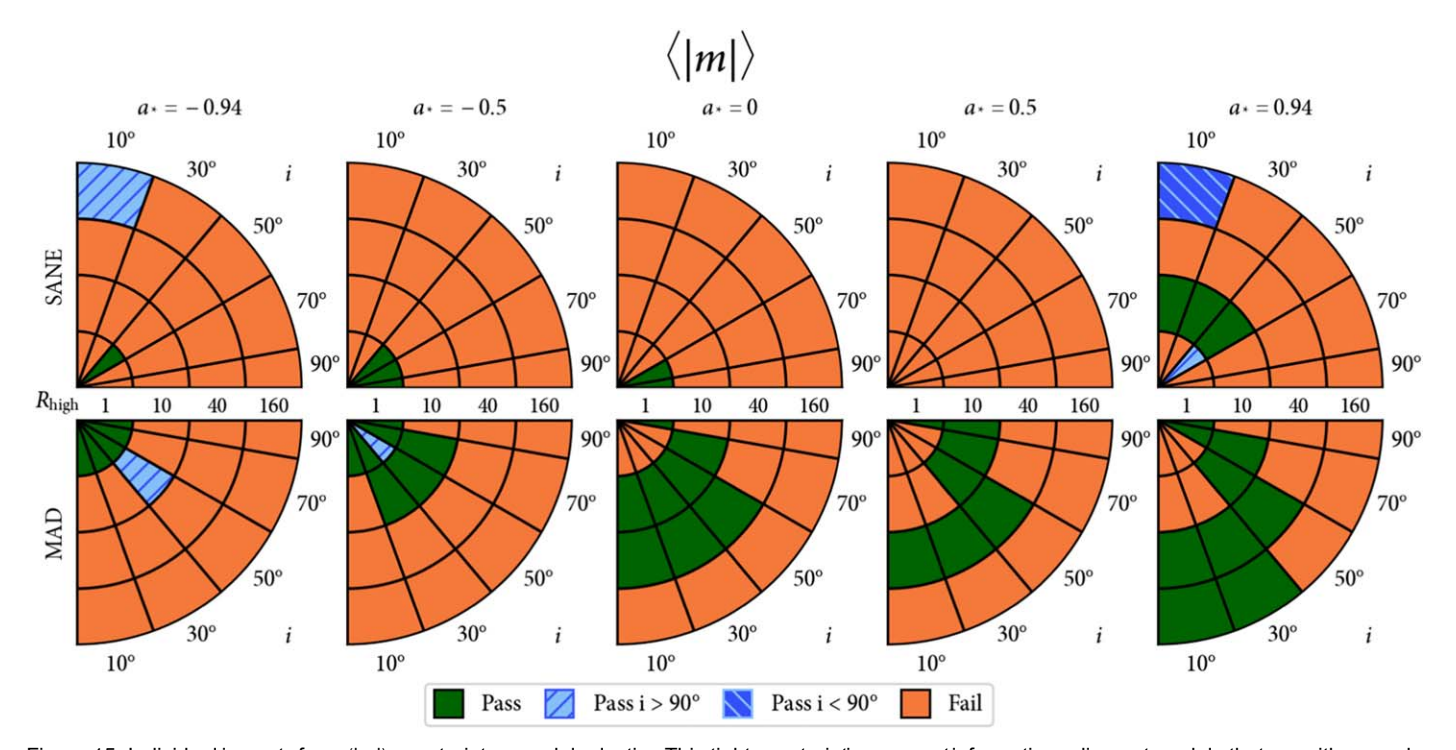


Figure 15. Individual impact of our (|m|) constraint on model selection. This tight constraint is our most informative, ruling out models that are either overly or insufficiently Faraday depolarized.

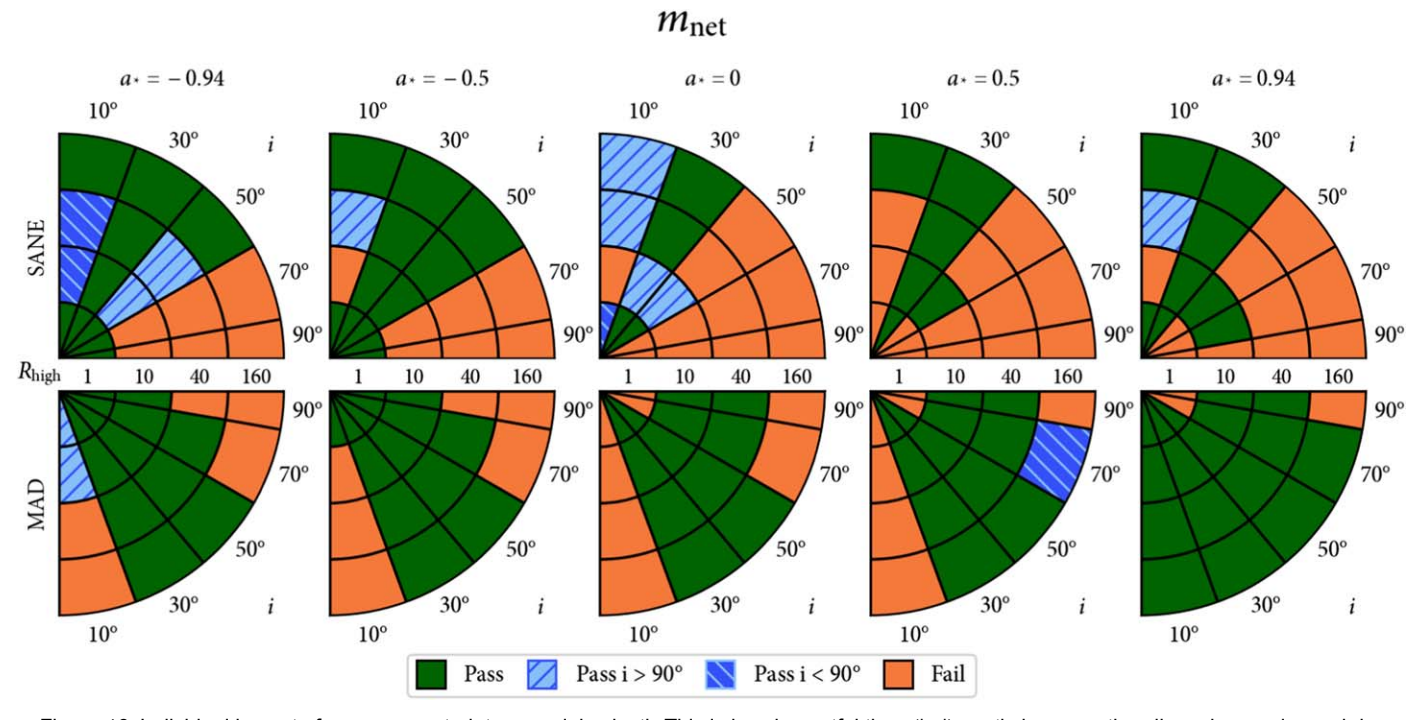


Figure 16. Individual impact of our met constraint on model selection his is less impactful than (|m|) mostly because the allowed range is much larger.

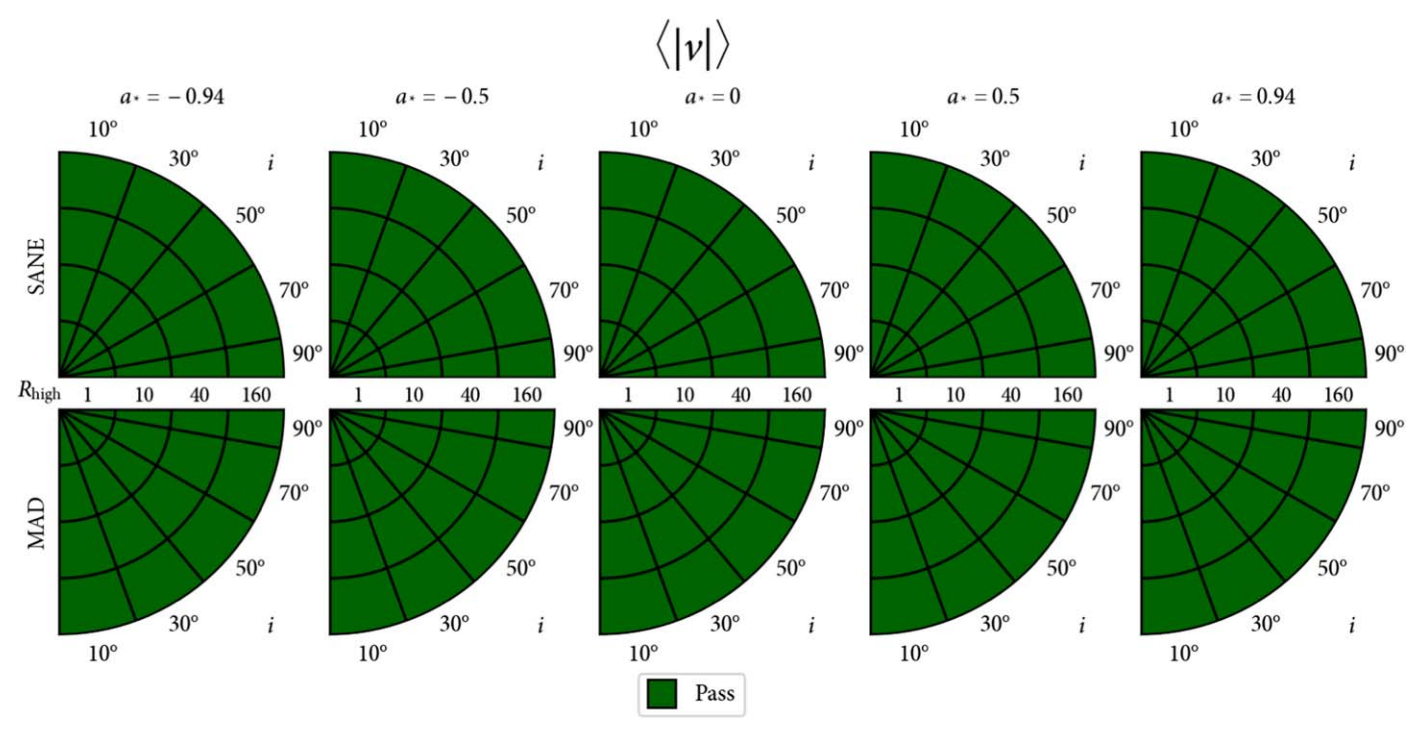


Figure 17. Individual impact of our $\langle |v| \rangle$ constraint on model selection, hich is treated as an upper limital models naturally produce smaller resolved circular polarization fractions than this constraint.

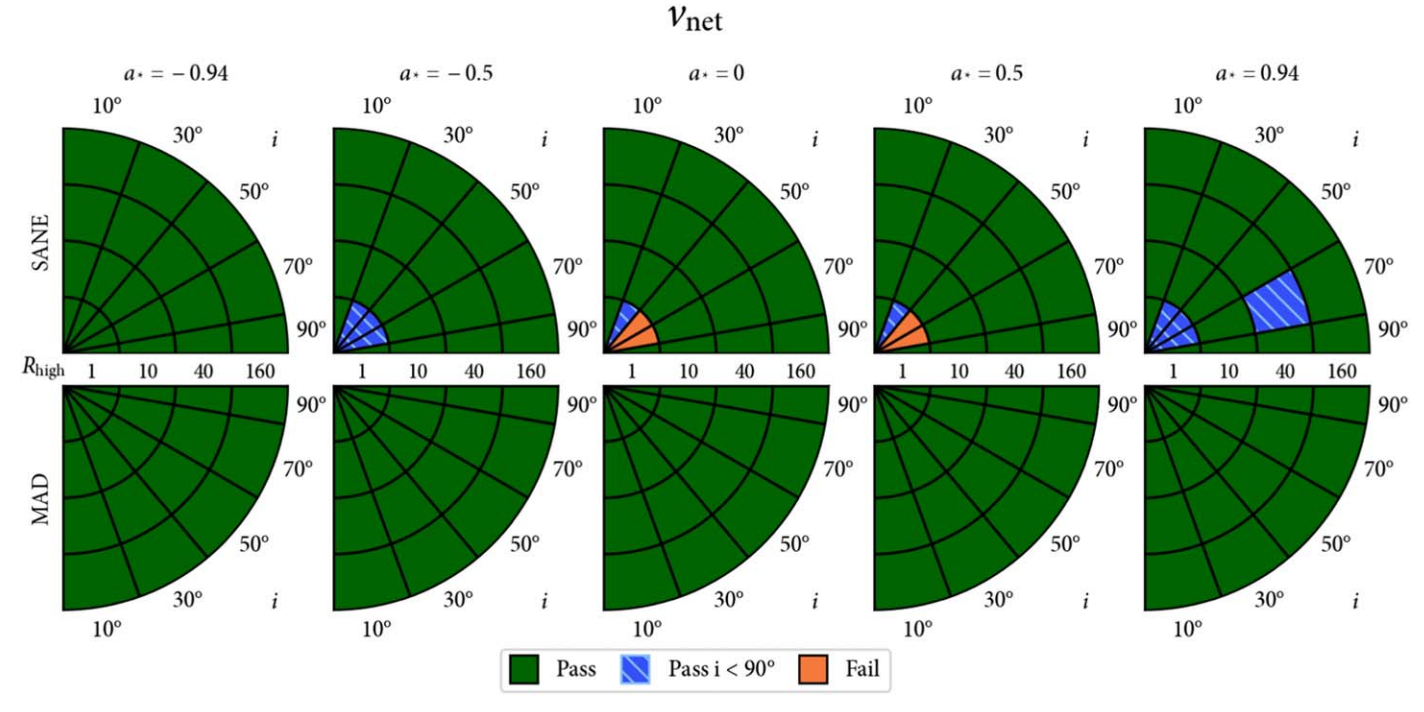


Figure 18. Individual impact of our to out models whose distributions cake wed toward positive values.

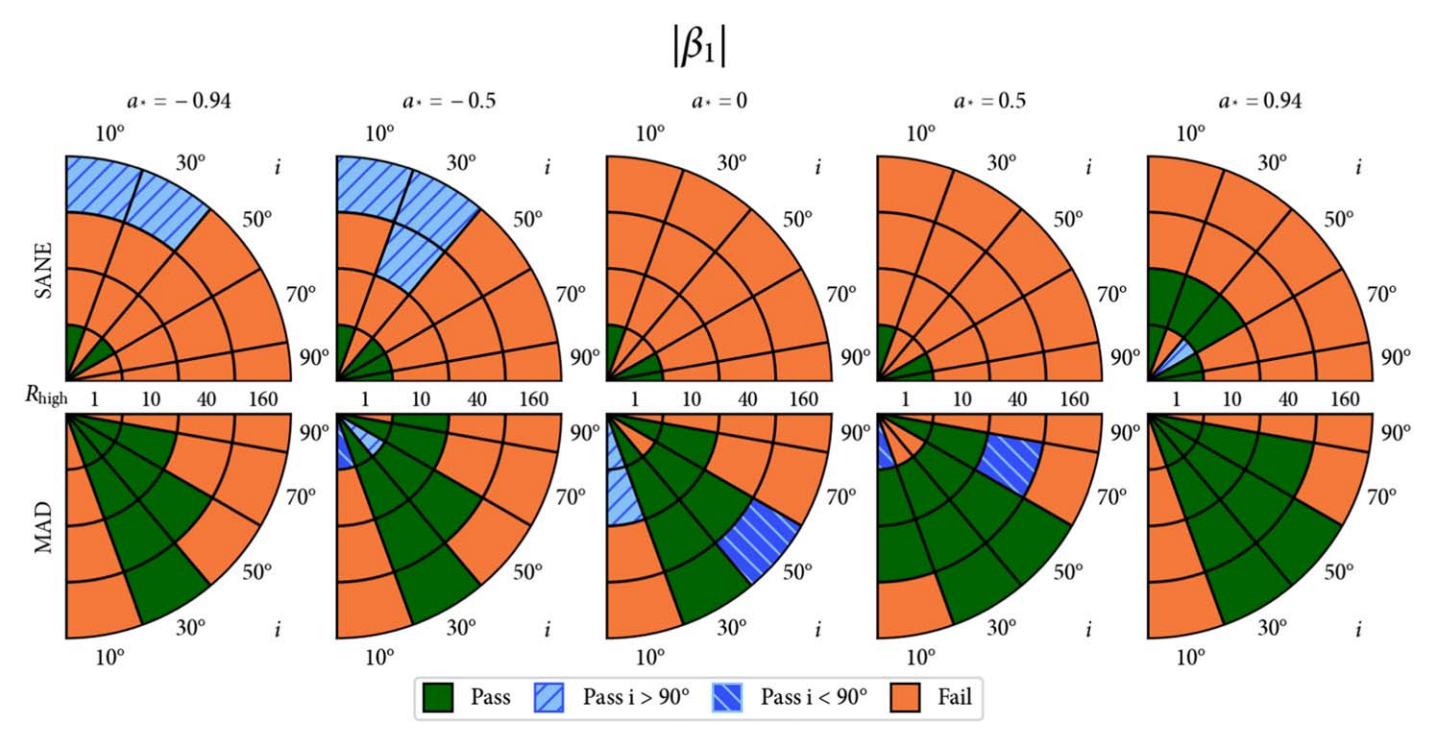


Figure 19. Individual impact of our $|\beta|$ constraint on model selection.

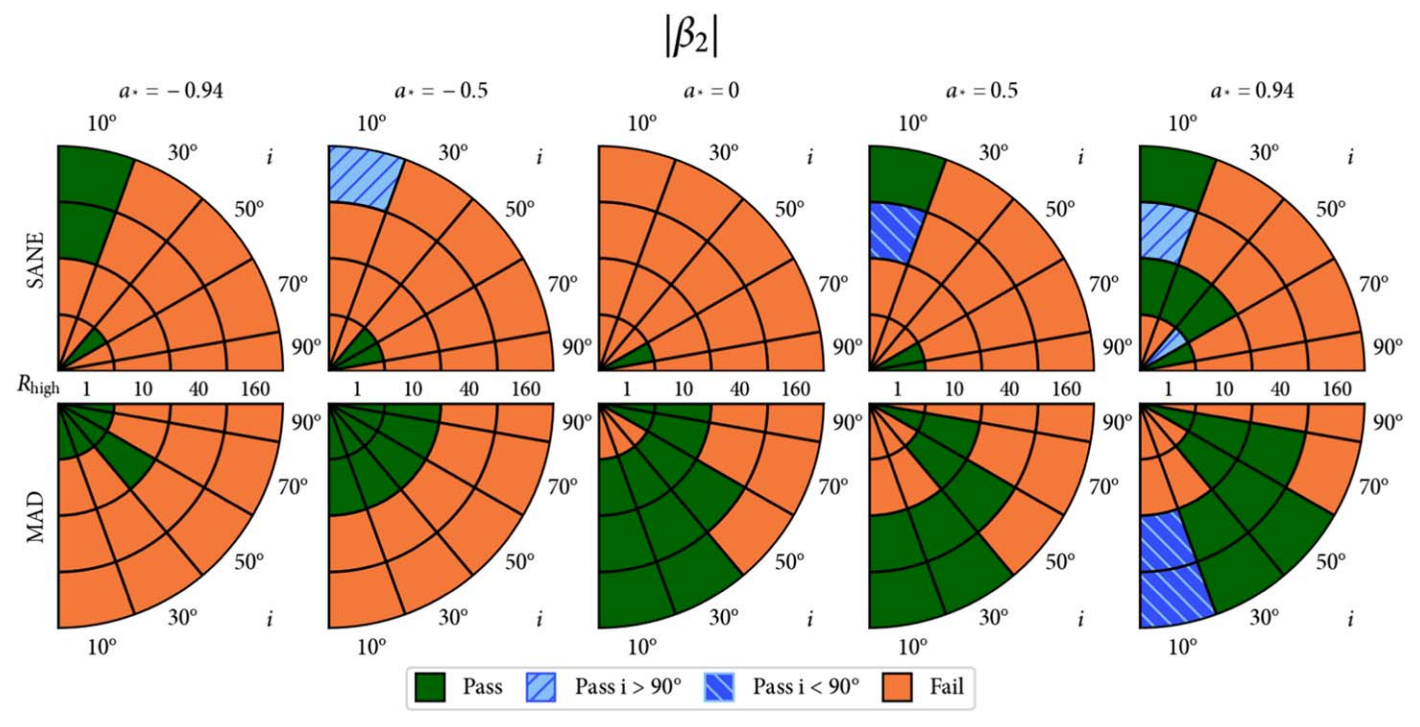


Figure 20. Individual impact of our $|\underline{\beta}|$ constraint on model selection. This observable is correlated with $\langle |m| \rangle$ and behaves similarly.

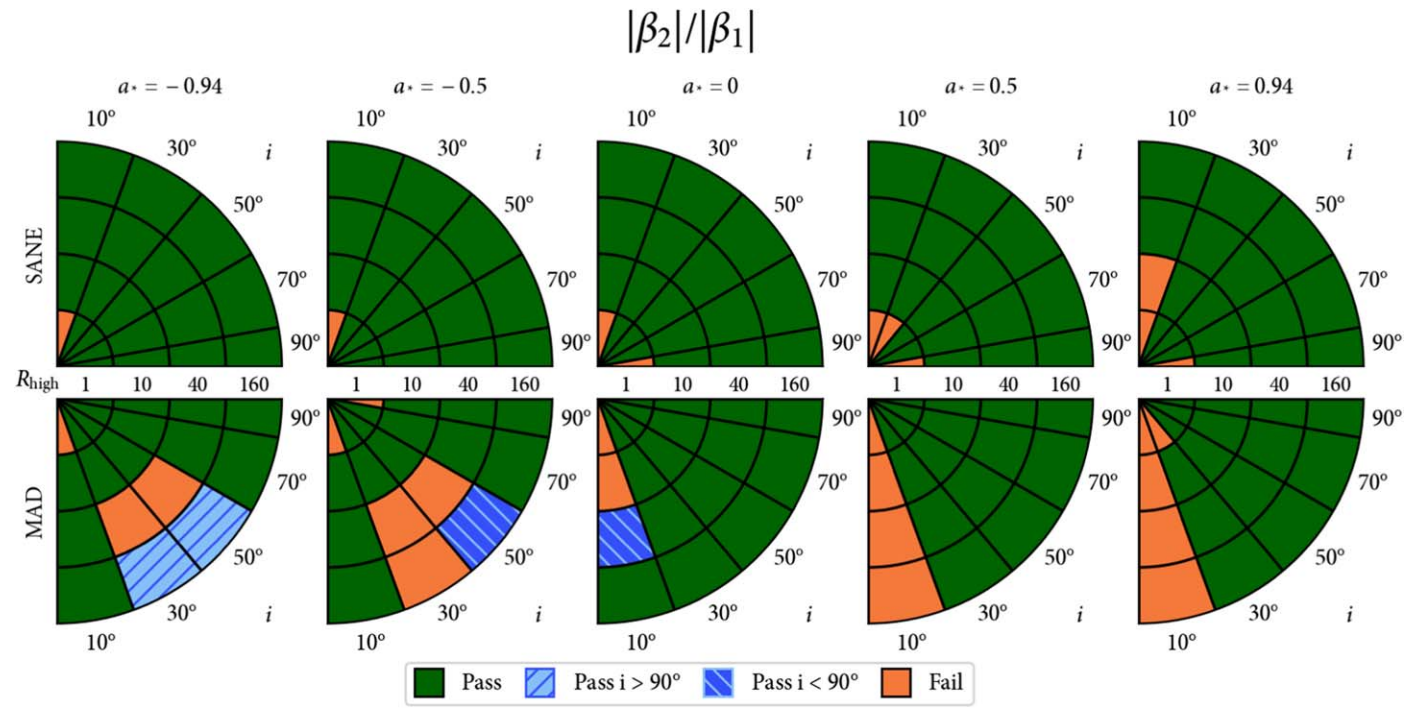


Figure 21. Individual impact of our |\(\beta_1\) constraint on model selection. This only rules out a few face-on models that are too rotationally symmetric.

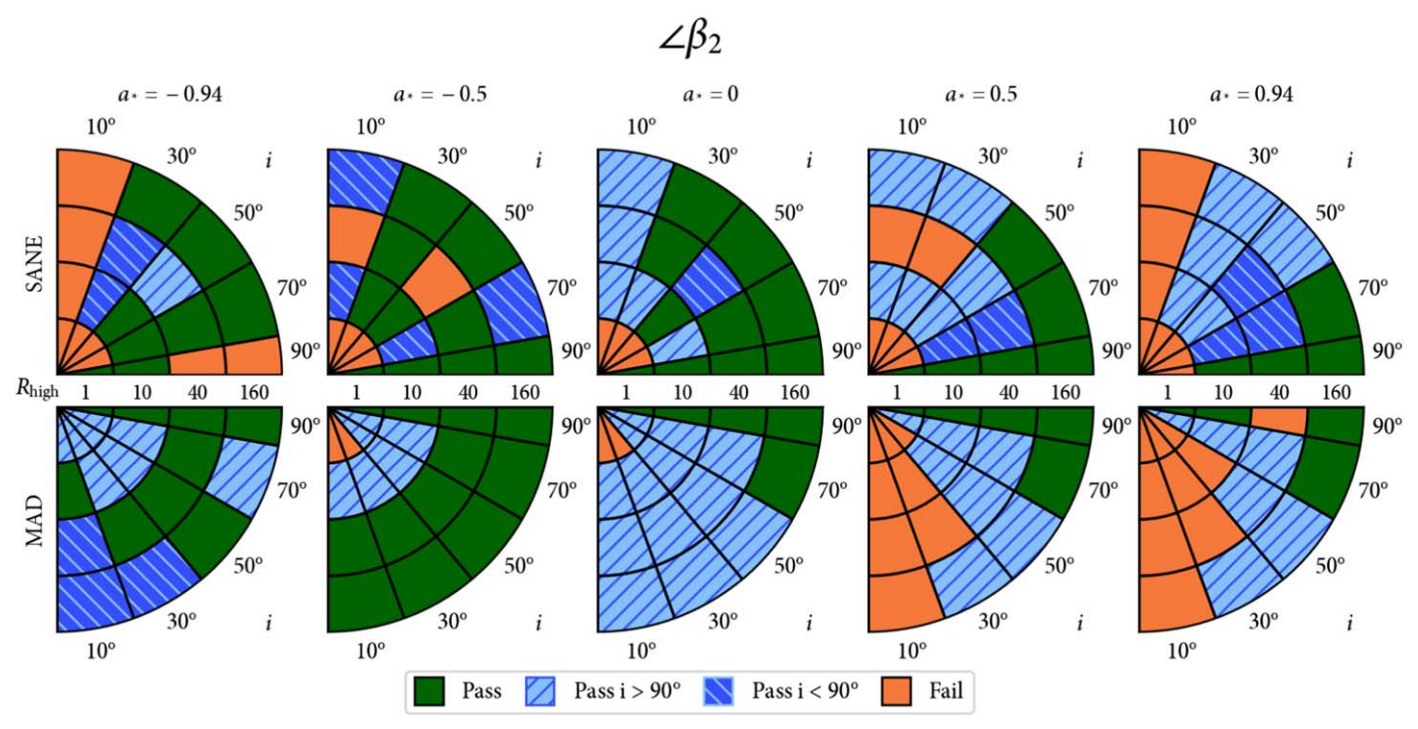


Figure 22. Individual impact of our ∠β₂ constraint with RM derotationThis constraint produces a preference for i > 90°.

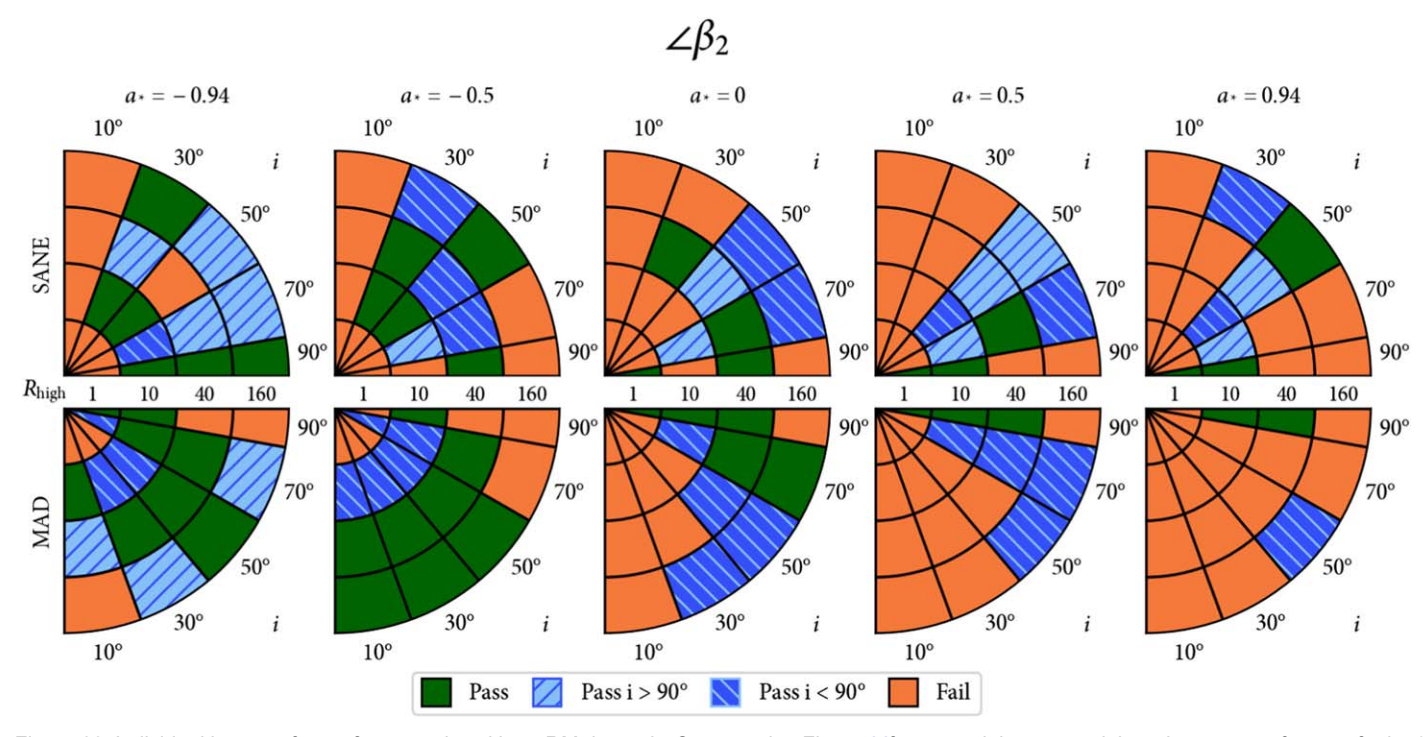


Figure 23. Individual impact of our ∠β₂ constraint without RM derotationCompared to Figure 22fewer models pass and there is now a preference for i < 90°.

Appendix C Rotation Measure

work, affecting our interpretation of ∠ The RM is defined as

RM °
$$\frac{Dc}{DI^2}$$
, (C1)

where χ is the EVPA and λ is the wavelength. If the EVPA of the polarized emission does not intrinsically change with

wavelength (due to optical depth), and the polarized emission is situated entirely behind a Faraday screen that is uniform The RM of Sgr Åis a significant systematic uncertainty in our relative to the size of the emitting region, then the RM is related to a path integral along the line of sight via

RM = 8.1 ′ 10⁵ rad m
2
 $\grave{Q}_{\text{source}}^{\text{observer}} f_{\text{rel}}(Q_{\text{e}}) \frac{n_{e}}{1 \text{ cm}^{-3}} \frac{B_{||}}{G} \frac{ds}{\text{pc}},$
(C2)

RM [rad m^{-2}]

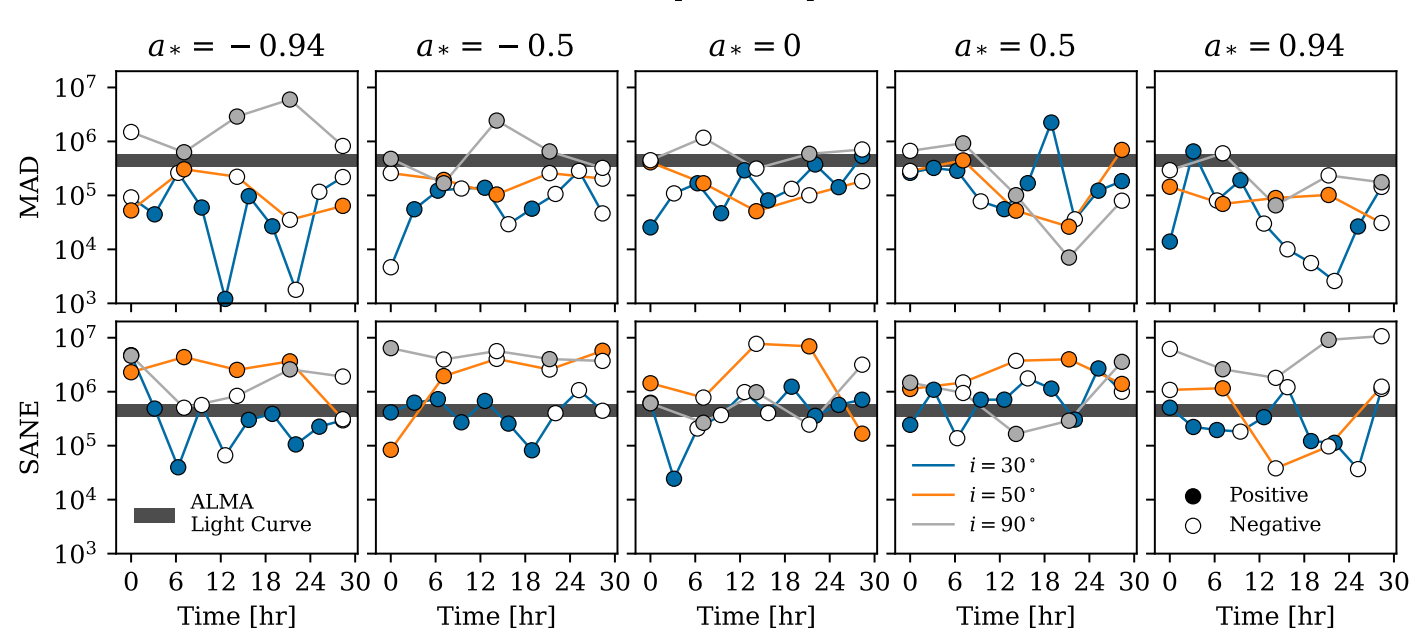


Figure 24. RM as a function of time for a selection of KHARMA model snapshotseach with R_{high} = 40 and aligned magnetic fieldsOur models can roughly reproduce the observed magnitude of the RM but predict rapid sign flips (colored/hitte markers) that are not observed.

where n_e is the electron number density, B_{II} is the local magnetic field parallel to the photon wavevector, and $f_{\rm rel}(Q_e)$ » $\log(Q_e)/(2Q_e^2)$, a factor causing lower efficiency as electrons become too relativistic (Jones & O'Dell 1971f). the two assumptions above are correct, then the "intrinsic" EVPA pattern can be easily recovered by derotating the EVPA by RM λ^2 .

Sgr A has exhibited a constant sign of RM for decades (Bower et al. 2018), which supports the interpretation of a stable external Faraday screen. GRMHD simulations including $(\rho_V = 0)$ in some of these models this suggests that evolving RM from event horizon scales predict ubiquitous sign flips on subhour timescales thate notobserved (Ricarte et al. 2020; Ressler etal. 2023; Wielgus et al. 2024). On the other hand, Sgr A* exhibits non- \Re evolution of the EVPA when comparing the 86 GHz and 230 GHz bands At 86 GHz the RM on nearly simultaneous days to our observations is only -2 × 10⁵ rad m² compared to -5 × 10 rad m² at 230 GHz (Wielgus et al. 2024). In addition to subhour time variability, this suggests that at least some of the RM must also come frorhorizon scales, and our GRMHD models overpredict the internal Faraday rotation on event horizon scales.

Carefully predicting the RM directly for all of our GRMHD simulations would increase the computational cost by factors ofmaging of Sgr Å will be critical; 345 GHz is less affected by a few (more than 2) with the software utilized in this work. This Faraday rotation by a factorof (345/230) ≈ 2. In addition, is because ray-tracing must be performed at different frequencies attonuniform spacings to resolve potential hase wrapping and non-λ behavior of the EVPA. Nevertheless, we check the RM for a few snapshots of our models in Figure 24, where the RM is estimated by ray-tracing at 213, 215, 227, and 229 GHz (emulating observations) and then fitting for the slope RM = $d\chi/d\lambda^2$. MAD models are plotted in the top row, and SANE models are plotted in the bottom row. Three inclinations Faraday rotation can originate atmuch larger radius in our are shown:30° in blue, 50° in orange, and 90° in gray. All models are at R_{gh} = 40 and in an aligned field configuration. Note that these simulations only include material within 1,00r but ab initio simulations of the accretion of Sgr from stellar

winds suggest that a steady Faraday screen could potentially be situated at even larger radii (Ressler et 2019, 2023).

We find that most of our models naturally produce |RM| ~ 10⁵ rad m² at at least one point in time, in rough agreement with the observed value. The SANE models, as well as the MADs at 90°, tend toward larger values, similar to models of M87 (Ricarte et al. 2020). However, as in previous works, the RM flips sign in every model at least once. Interestingly, we find similar order-of-magnitude values of RM if Faraday rotation is explicitly switched off during ray-tracing emission origin as a function of frequency may contribute to the inferred RM and its variability.

Our findings in Figure 24 are broadly consistentwith an interpretation wherein the rapid time variability of RM is caused by variability on event horizon scales the stability of sign is maintained by an external Faraday screen along the line of sight, motivating derotation of ∠ß On the other hand, it may also be possible that all of the RM originates from event variability in RM in the same way that they overpredict variability in total intensity (Paper V). To resolve this, 345 GHz RM maps produced via simultaneous multifrequency imaging will help determine the nature of the Faraday screen.

Appendix D Impact of Outer Integration Radius

Although we are confident that most of the emission in our models originates close to the event horizon (r \square 10r), models, more so as the inclination increases (Dexter et al. 2020; Ricarte et al. 2020). This is especially problematic because materialat these radiimay not have had enough time in the simulation to reach equilibrium. This concern is more

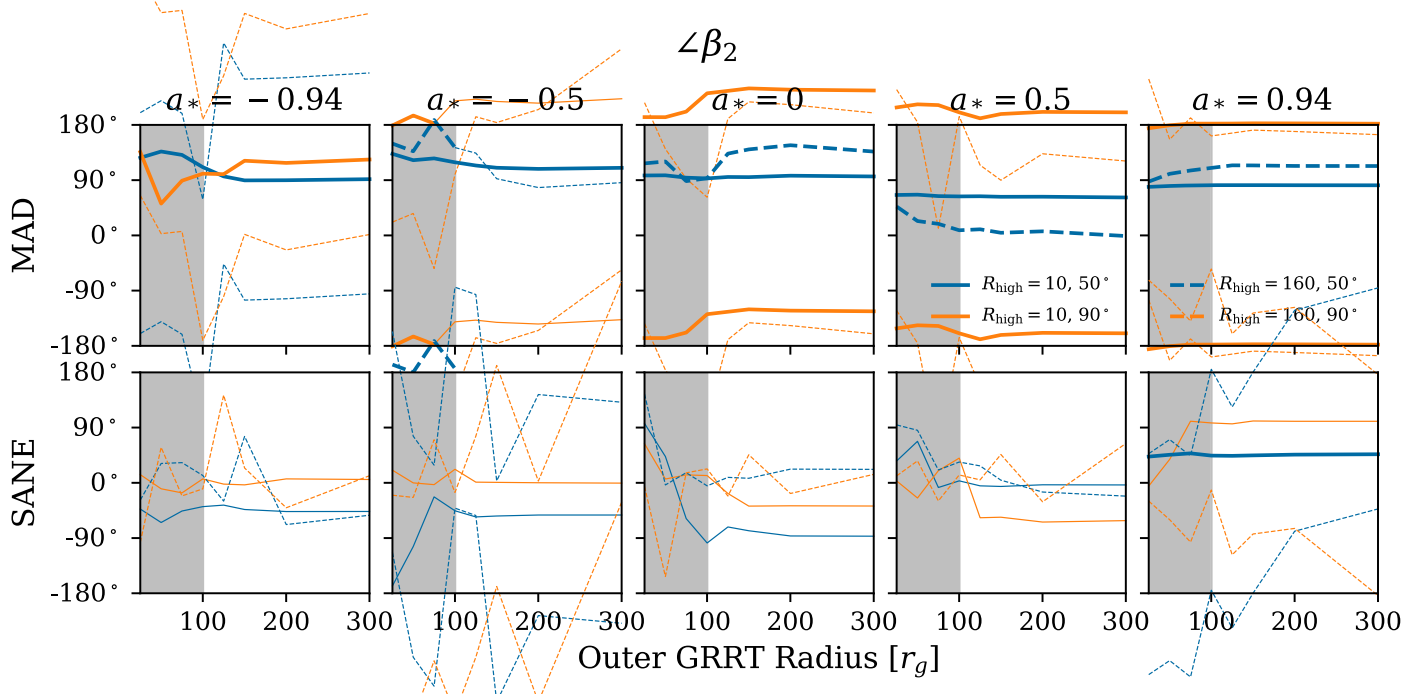


Figure 25. ∠β₂ as a function of outer integration radius for a selection of KHARMA models. The GRRT in our work includes material at τ, entabolited by the gray band Lines transition from thick to thin at the first radius at which $\frac{1}{2}$ 8 o .05. For models with $\frac{1}{2}$ 9 o .05, $\frac{1}{2}$ 9 o .05, $\frac{1}{2}$ 9 ypically converges by $\frac{1}{2}$ = 100 $\frac{1}{2}$ 1.

important for studies of Sqr Athan for M87 because we view M87 at an inclination of only 17° through an evacuated funnel.

We test the impact of the outer radiative transfer integration radius in Figure 25, where we ray-trace a few KHARMA snapshots at a variety of radii ranging from 300 300rg. We focus on ∠β₂, which should be directly affected by Faraday rotation on large scalesInclinations of both 50° and 90° are considered, with R_{gh} values of both 10 and 160. Fortunately, we find that $\angle \beta_2$ appears to have converged for most of these models before 100r where we perform the ray-tracing in this paper. We find that the models that do exhibit substantial evolution with outer integration radius all produce (|m|) lower than observed. Note that SANE models at 90° inclinations with This choice is only safe when no σ R_{high} = 160 are the mostFaraday-thick models in our library. Models at i = 90 and/or high R_{high} appear to have the most evolution with respect to the integration radius. This is consistentwith the expectation that higher inclinations and higher Righ values will increase the amount of Faraday rotation however, finite-resolution effects in the GRMHD simulations. owing to more photons traveling through dense, cold regions irresolved interchange instabilities and potentially strong disk the GRMHD domain.

While $\angle \beta_2$ appears to show evolution for some modelse other polarimetry metrics are well converged and show minimal change for all models across integration radius. However, although we have checked the GRRT steprecall that our GRMHD models are only converged within r \square 30r owing to computationallimitations. Exploration with simulations that are valid to larger radii that may produce an external Faraday screen self-consistently (e.g.Ressleret al. 2023) would be an interesting avenue for future analysis.

Appendix E Impact of Cutting Jet Center ("o cut")

The polar funnelin the GRMHD simulations is filled with horizon-penetrating field lines and thoughto contain plasma with orders of magnitude lower density than the accretion disk dominate in the model.

By the same token, the funnel magnetization $\sigma := B^2/\rho$ is believed to be much larger than the magnetization in the disk. Since there are very few emitting particles in the funnelits contribution to the overall image is expected to be negligible. In practice, to keep the numerical GRMHD evolution stable, σ is not allowed to assume realistic values but is instead capped at moderate values $\sigma \square 50-100$ by artificially injecting mass (e.g., Porth et al. 2019). Hence, we cannot trust the inflated mass density in this region. Assuming that emission in the σ ? 1 funnel should in reality be negligible, we follow the common practice and set all radiation transport coefficients to zero when the magnetization exceeds a critical value ₹1. 1 regions form naturally in the disk and when the mixing of disk and funnel plasma at the jet wall is inefficient. In this case the gradient in magnetization is steep which means that whether we adopt σ_{cut} = 1 or, e.g., σ_{ut} = 25 does not affect the results. In reality,

magnetization can cause a dependence on the adopted threshold value.

Using the BHAC/RAPTOR datawe have carried outspot checks with two "best-bet" models whereby we increase the threshold to σ_{cut} = 25: model 1 is MAD a * = 0, R_{high} = 40, i = 150° aligned, and model 2 is MAD∗æ 0.94, R_{high} = 160, i = 30° aligned. In either case, the constraints change only by a few percent, e.g., in model 2 the average

β phase changed from 63° to 66° and the average nepolarization wentdown from 2.9% to 2.7%. In model 1, the change in average as is somewhat larger (going from -97° to -109°), but still small compared to the overall spread of the distributions. This shows that the results on polarized submillimeter emission are quite robust against change in the adopted value of the σ_{cut} and emission ator within the highly magnetized funneldoes not

Appendix F Impact of Nonthermal Electrons

Throughout this work, we have considered only thermal eDFs when performing GRRT. Here we briefly explore the impact of nonthermal electrons in the polarimetric properties one GRMHD model: MAD a *=0, $R_{high}=40$, $i=150^{\circ}$ aligned. Two nonthermal prescriptions are explored:

- 1. Variable κ : In each cell, a κ distribution (Vasyliunas 1968; Xiao 2006) is applied, using a $\kappa(\sigma, \beta)$ prescription originating from particle-in-cell simulations (Ball et al. 2018; Davelaar et al2019).
- 2. κ = 5: A κ distribution with a constant value of κ = 5 is applied globally (Davelaar et aP018).

We ray-trace 300 snapshotsfor each of these cases and compare with the thermal model snapshots accretion rate is kept fixed, but we find that the average flux density is 2.3 Jy for all cases. In Figure 26, we plot a selection of polarimetric quantities for these models. Each marker is placed at the median, and the error bars extend to the 16th and 84th percentiles. Overall, we find only subtle differences between these different eDF models. Ve find that $\langle |m| \rangle$ declines in the nonthermal eDF models, coincident with increases in the Faraday rotation depth (2.2,2,and 6.3 for thermal. Variable κ , and κ = 5 models, respectively). Interestingly ω_{net} switches sign in the κ = 5 model, while ω varies only slightly, due to its link with the underlying field geometry. Overall, images with nonthermal eDFs will be useful to study in future work.

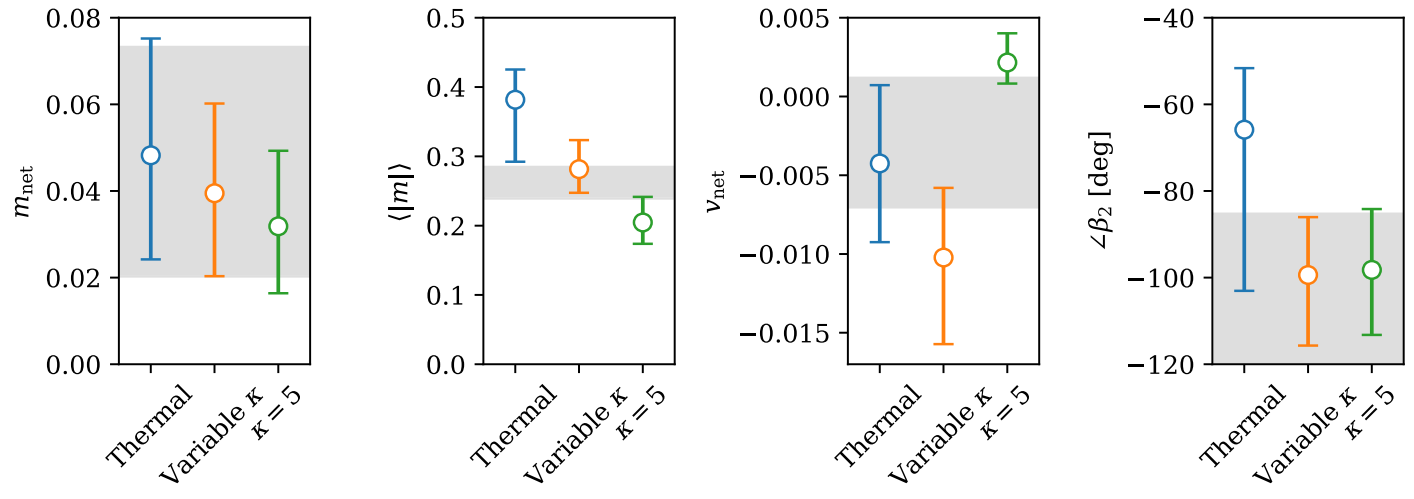


Figure 26. Comparison of thermal and nonthermal eDFs for MADQ, R_{high} = 40, i = 150° aligned models. Changes in the distributions of polarimetric quantities motivate future exploration in this area.

Appendix G An Interpolative Scoring Scheme

With our GRMHD models, we coarsely sample a fivedimensional parameter spaceere we investigate the possibility that this sparse sampling misses potentially passing models evolve rapidly between adjacent models. In addition, this by performing scoring using expanded theoreticatror bars. We conceptualize each combination of *, Rhigh, and i as a volume in three-dimensional parameter space. For each neighbor in parameter space, if the 90% quantiles of the

neighbor do not overlap, we linearly interpolate the lower and upper ranges of each observable to the midpoints of their nearest neighbors. This scheme helps mitigate sparse sampling but, as we discussmay lead to false positives if observables methodology fails to consider correlated evolution between observables.

In Figures 27 and 28, we show the results of our interpolative scoring scheme considering all polarimetric

All Polarimetric Constraints

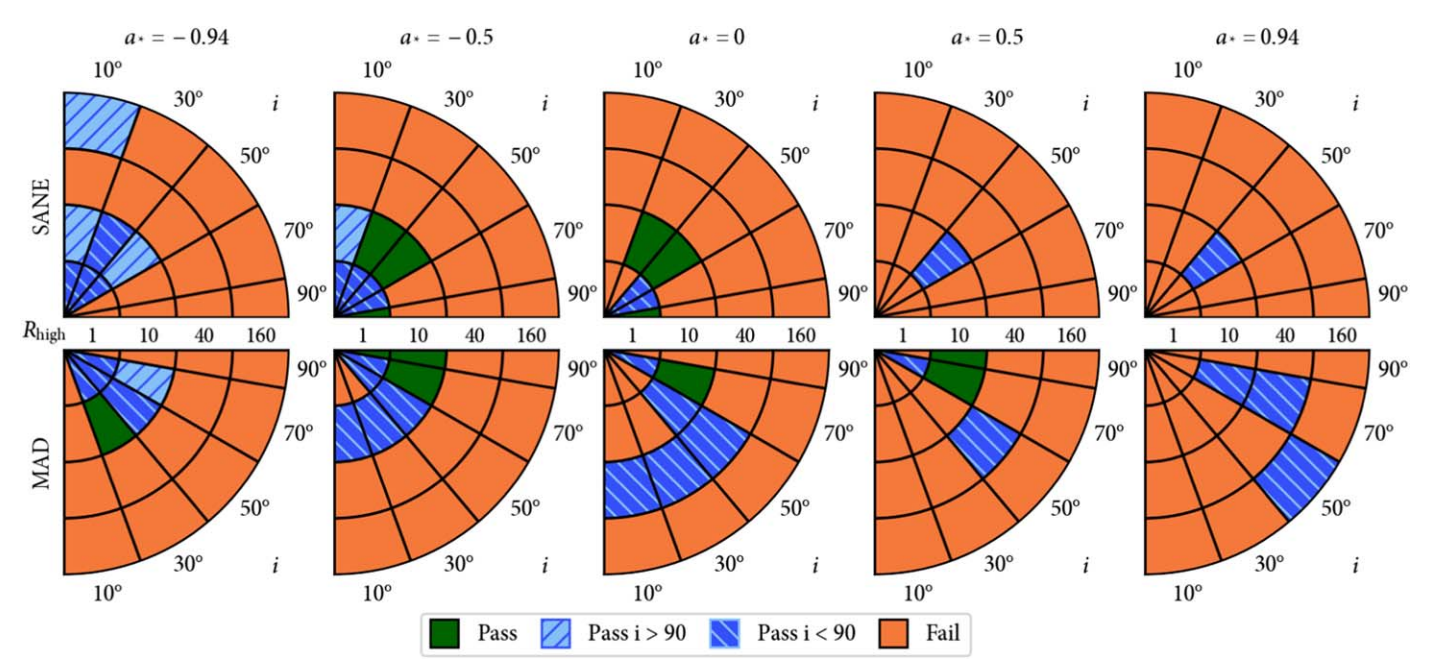


Figure 27. Same as Figure 7but using the interpolative scoring scheme described in Appendix G.

All Polarimetric Constraints

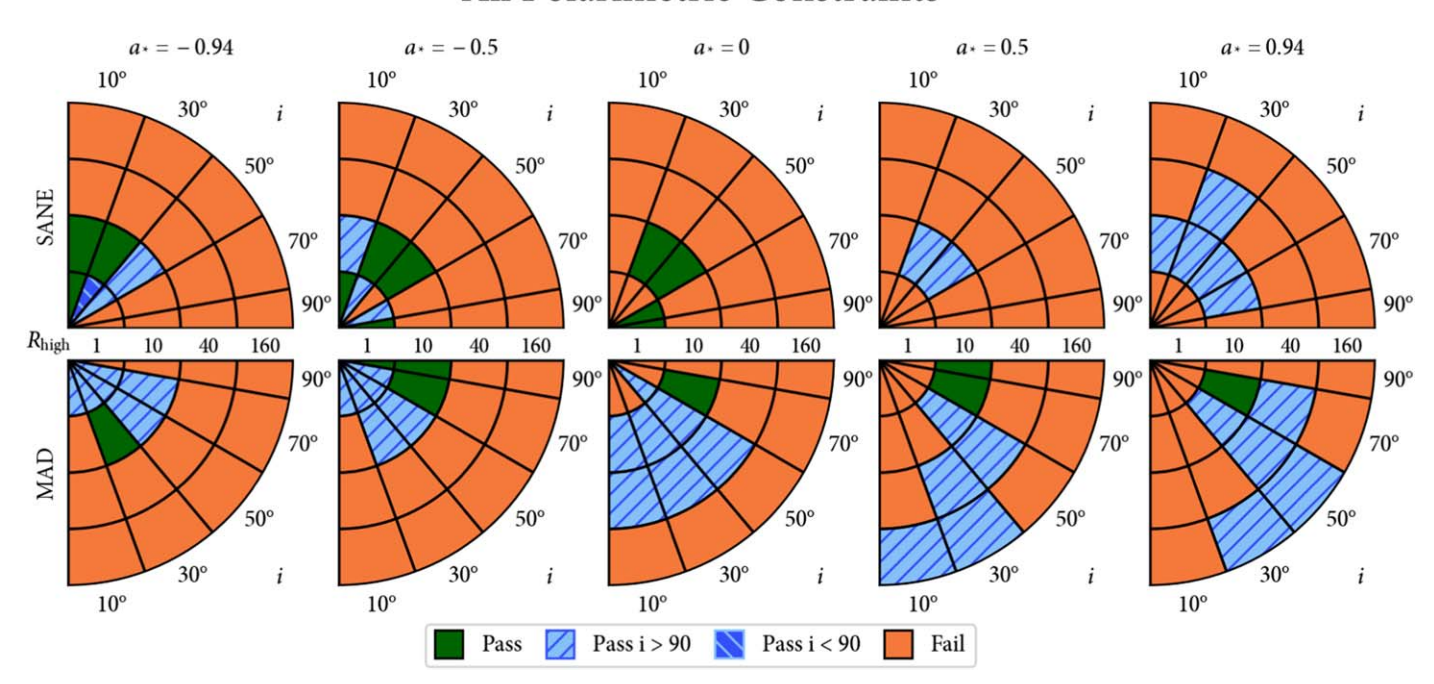


Figure 28. Same as Figure 8but using the interpolative scoring scheme described in Appendix G.

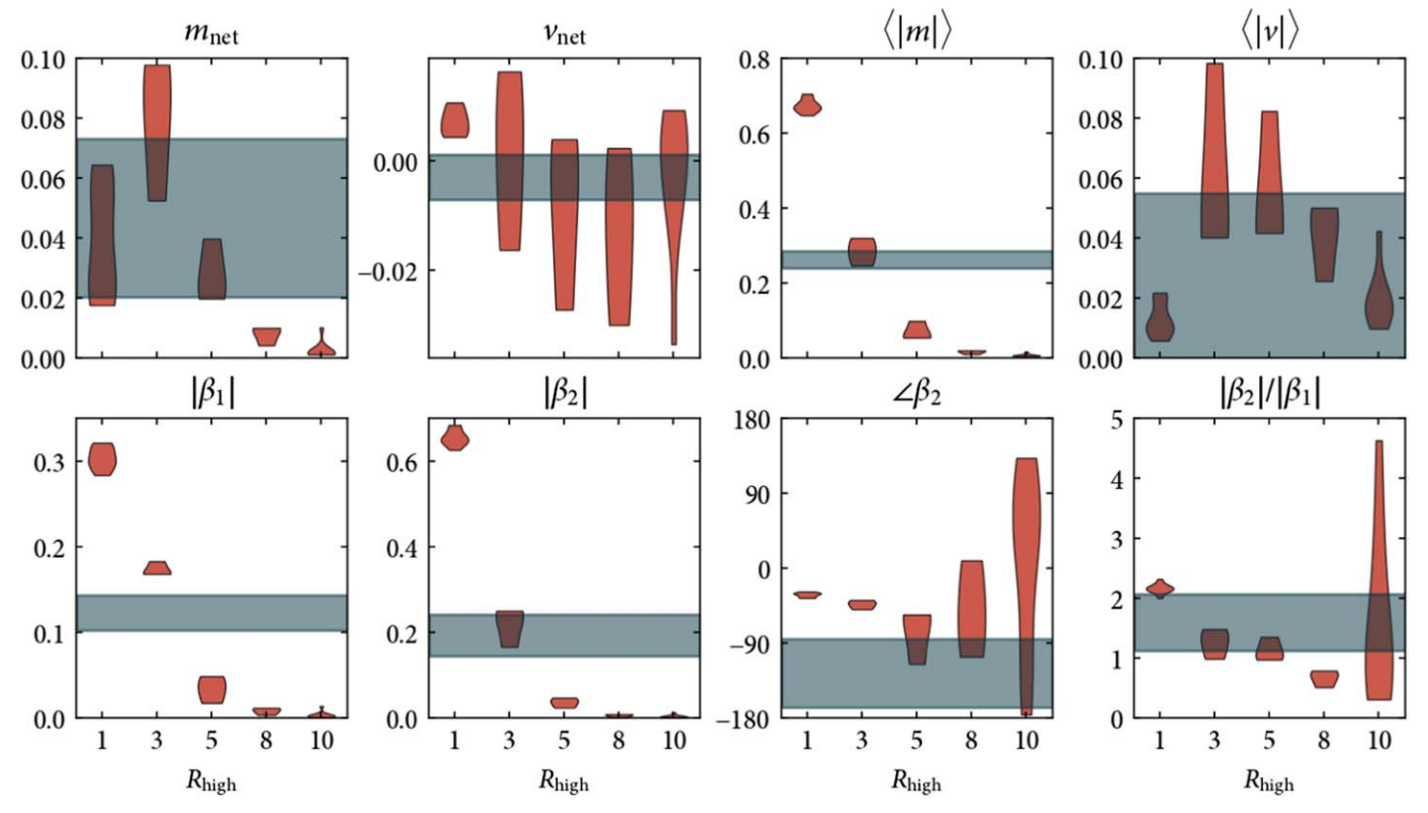


Figure 29. Distributions of observables for a selection of SANE models ray-traced with greater resolution between 1 and 10. These correspond to KHARMA SANE a* = -0.5, i = 150° aligned models. We find rapid evolution in this part of parameter space.

constraints without and with RM derotation, respectively As expected, many more models pass in both cases. The preference forclockwise motion with derotation or counterclockwise motion without derotation is less dramatic with this scheme. Without derotation, both best-bet models still fail. With derotation, the second best-betmodel from Paper V. MAD a * = 0.5, R_{high} = 160, i = 30°/150°, also passes in this scheme. Without interpolation, this model had only failed by producing too little (|m|).

This interpolative scoring scheme does not produce as clea of a preference for MAD over SANE models. We find that this difference is driven by a shortcoming of this methodSANE models evolve very rapidly with R $_{\rm high}$, especially between R_{high} = 1 and R_{high} = 10, leading to very large theoretical error bars. We explore one example in Figure 29, where a set of KHARMA SANE a * = -0.5, i = 150° aligned field models are ray-traced at intermediate values of Rä {3, 5, 8}. Each of our eight polarimetric observables is plotted we better resolve the rapid evolution in these parameters with R. A noteworthy interaction occurs in our interpolation scheme with $\langle |m| \rangle$ and $\angle \beta_2$, two of our most constraining observables/le see that at \mathbb{R}_{igh} = 1 the model overproduces $\langle |m| \rangle$ but fails to reproduce ∠g, which is too radial. Meanwhile, SANE models with R_{high} = 10 have too low $\langle |m| \rangle$ and a uniformly distributed $\angle \beta_2$. Interpolation allows models in this region to pass because gray, where, as usual, the allowed range for $\angle \beta$ without RM our scoring system suggests that there might be a model with intermediate Rah that has both a correct ∠and a correct (|m|). However, with better resolution in Rgh, we do not find an individual model that would pass. Overall, this exercise shows thatour main conclusions are ndtkely driven by our sparse sampling of parameter space.

Appendix H **GRMHD Observable Distributions**

To visualize trends of our eight observablesin the fivedimensional parameterspace that we explore, we provide "violin" plots of our observables from our models as a figure set, the complete version of which is available in the online journal. In each figure, we considerone observable and one magnetic field state (either MAD or SANE models). One figure, the distributions of met for MAD models, is shown in Figure 30. Different spins are shown in different columns, and different values of R_{high} are shown in differentrows. Within each panel,we plot distributions as a function of inclination, where only five of the nine inclinations ray-traced in this work are included to improve readabilityAligned field models are shown on the left, and reversed field models are shown on the right. The distributions with opposite magnetic field polarity are usually very similar, with the notable exceptions of and, more subtly, $\angle \beta_2$. To display the relative agreementor disagreemenbetween codes, we plot BHAC models in red and KHARMA models in blue. H-AMR models, which are raytraced for a subset of models only for comparison here and not for scoring, are displayed as dashed distributions when available. Finally, the observation abonstraints are shown in derotation is shown as a hatched region.

Our last set of plots, distributions of the Faraday rotation depthá t_{r_v} $\tilde{\eta}$, are notdirectly observable butdrive many of our physical trends, as well as differences between code sor a detailed discussion of the physical trends present in these figures, we refer readers to Appendix A.

$m_{\rm net}$ (MAD models)

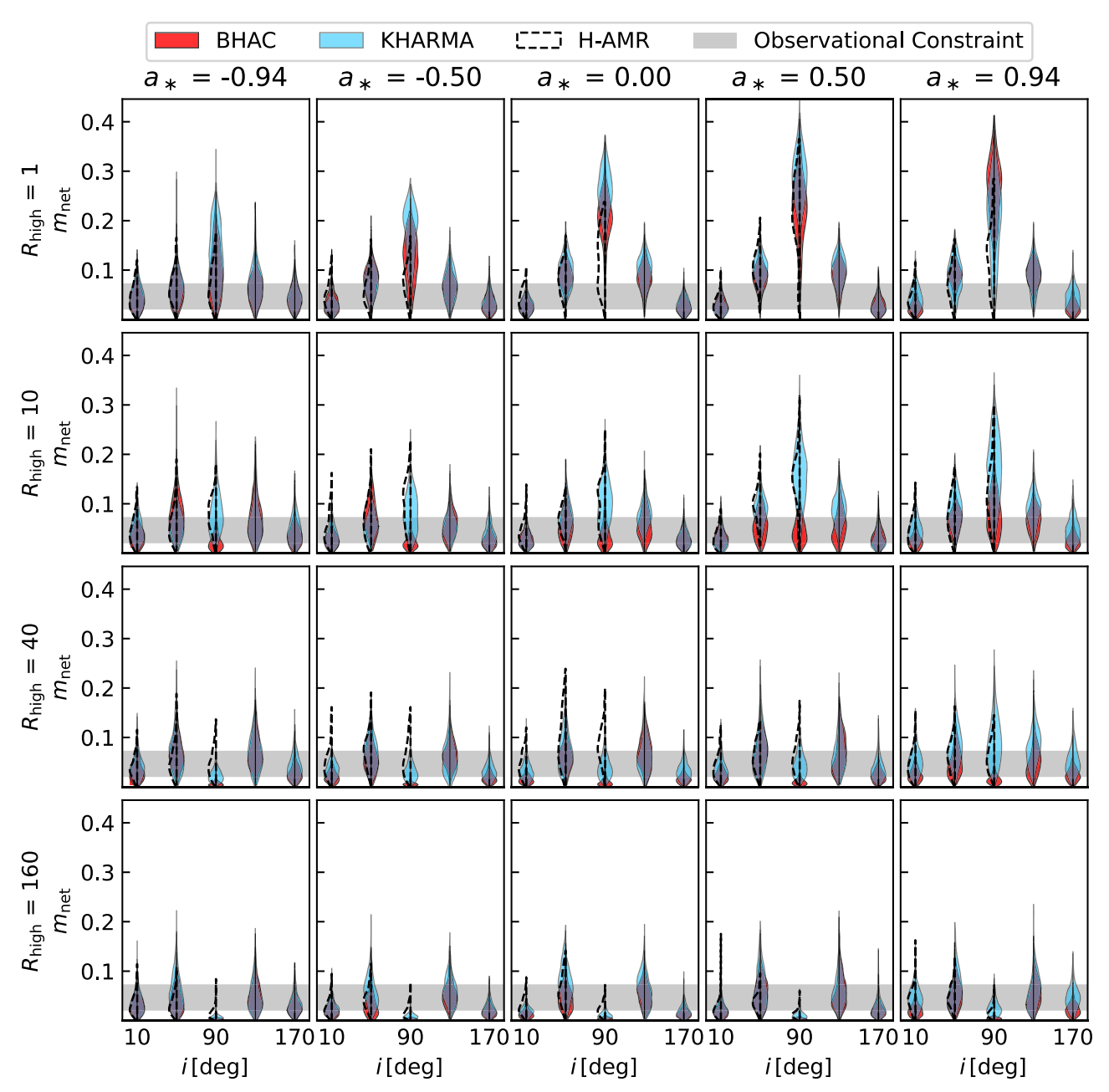


Figure 30. Distributions of observables for either MAD or SANE models. BH spirades in each column, and warries in each row. Inclination varies along the x-axis. BHAC and KHARMA GRMHD simulations are shown in red and blue in each case, respectively, with H-AMR shown as a dashed curve. Distributions plotted on the left represent aligned magnetic fields, while those plotted on the right represent reversed magnetic fields. Our observational constraint is shown in gray. The complete figure set (18 images) is available in the online journal.

(The complete figure set (18 images) is available.)

Differences between our KHARMA and BHAC models inflate our theoreticaerror bars in Section 5.We find that at leastpart of these differences arise from physicapproximations regarding the assignment electron temperature during the GRRT. One fluid with a single adiabatic index is evolved in our GRMHD codes, but it represents both relativistic electrons (with an adiabatic index of 4/3) and nonrelativistic ions (with an adiabatic index of 5/3). During the GRRT step of our

calculations, only the electron temperature is relevant the synchrotron emission that we observe. When assigning electron temperatures APTOR adopts (see.g., Davelaar et al 2018)

$$Q_{e} = \frac{u}{r} \frac{m_{p}}{m_{e}} \frac{1}{3(R+1)},$$
 (H1)

where Q_e is the electron temperature, is the internal energy, and $R = T_i/T_e$ given by Equation (8). Meanwhile, IPOLE

accounts for the difference in adiabatic indices by adopting

$$Q_{e} = \frac{u}{r} \frac{m_{p}}{m_{e}} \frac{(g_{p} - 1) (g_{e} - 1)}{(g_{e} - 1)R + (g_{p} - 1)}$$

$$= \frac{u}{r} \frac{m_{p}}{m_{e}} \frac{2}{3(2 + R)},$$
(H2)

where $\gamma_e = 4/3$ and $\gamma_p = 5/3$. Equation (H2) is physically justified, but it sacrifices internal consistency with the GRMHD Nicholas S. Conroyo https://orcid.org/0000-0003-2886-2377 simulations, where a single fluid with y = 4/3 is (Wong et al. 2022). When we set $\gamma_e = \gamma_p = \gamma = 4/3$ in Equation (H2), we recover Equation (H1) used by RAPTOR. Electron temperatures assigned by RAPTOR are systematically Geoffrey B. Crew https://orcid.org/0000-0002-2079-3189 colder, 3/4 as hot as the POLE prescription at R = 1 and 1/2 as hot as $R \rightarrow \infty$. This explains the systematically larger Faraday depths in our BHAC models relative to both KHARMAYuzhu Cui(崔玉竹 № https://orcid.org/0000-0001and H-AMR, which are both ray-traced with POLE.

Larger differencesare seen between SANE modelsthan MADs. A unique SANE model is not believed to exist, and differencesare known to occur at the GRMHD fluid level (Porth et al.2019).

ORCID iDs

Kazunori Akiyama https://orcid.org/0000-0002-9475-4254 Antxon Alberdi https://orcid.org/0000-0002-9371-1033 Juan Carlos Algaba https://orcid.org/0000-0001-6993-1696 Richard Anantua https://orcid.org/0000-0003-3457-7660 Keiichi Asada https://orcid.org/0000-0001-6988-8763 Rebecca Azulayo https://orcid.org/0000-0002-2200-5393 Uwe Bach® https://orcid.org/0000-0002-7722-8412 Anne-Kathrin Baczko https://orcid.org/0000-0003-3090-3975

Mislav Baloković https://orcid.org/0000-0003-0476-6647 Bidisha Bandyopadhyay https://orcid.org/0000-0002-2138-8564

John Barretto https://orcid.org/0000-0002-9290-0764 Michi Bauböck https://orcid.org/0000-0002-5518-2812 Bradford A. Benson® https://orcid.org/0000-0002-5108-6823

Lindy Blackburn https://orcid.org/0000-0002-9030-642X Raymond Blundello https://orcid.org/0000-0002-5929-5857 Katherine L.Bouman® https://orcid.org/0000-0003-

Geoffrey C.Bower https://orcid.org/0000-0003-4056-9982 Hope Boyce https://orcid.org/0000-0002-6530-5783 Christiaan D.Brinkerink https://orcid.org/0000-0002-2322-0749

Roger Brissenden https://orcid.org/0000-0002-2556-0894 Silke Britzen® https://orcid.org/0000-0001-9240-6734 Avery E. Broderick https://orcid.org/0000-0002-3351-760X

Dominique Broguier https://orcid.org/0000-0001-9151-6683

Thomas Bronzwae https://orcid.org/0000-0003-1151-3971 Sandra Bustamante https://orcid.org/0000-0001-6169-1894 Do-Young Byun https://orcid.org/0000-0003-1157-4109 John E.Carlstrom® https://orcid.org/0000-0002-2044-7665 Chiara Ceccobello https://orcid.org/0000-0002-4767-9925 Andrew Chaelo https://orcid.org/0000-0003-2966-6220 Chi-kwan Chan https://orcid.org/0000-0001-6337-6126 Dominic O. Chango https://orcid.org/0000-0001-9939-5257

Koushik Chatterjee https://orcid.org/0000-0002-2825-3590 Shami Chatterjee https://orcid.org/0000-0002-2878-1502 Ming-Tang Chen® https://orcid.org/0000-0001-6573-3318 Yongjun Chen (陈永军) https://orcid.org/0000-0001-5650-6770

Xiaopeng Chengo https://orcid.org/0000-0003-4407-9868 Ilje Cho https://orcid.org/0000-0001-6083-7521 Pierre Christian https://orcid.org/0000-0001-6820-9941 John E.Conway https://orcid.org/0000-0003-2448-9181 James M.Cordes[®] https://orcid.org/0000-0002-4049-1882 Thomas M.Crawford https://orcid.org/0000-0001-

Aleiandro Cruz-Osorio https://orcid.org/0000-0002-3945-6342

6311-4345

Rohan Dahale https://orcid.org/0000-0001-6982-9034 Jordy Davelaa https://orcid.org/0000-0002-2685-2434 Mariafelicia De Laurentis https://orcid.org/0000-0002-9945-682X

Roger Deane https://orcid.org/0000-0003-1027-5043 Jessica Dempsey https://orcid.org/0000-0003-1269-9667 Gregory Desvignes https://orcid.org/0000-0003-3922-4055 Jason Dexter https://orcid.org/0000-0003-3903-0373 Vedant Dhruv® https://orcid.org/0000-0001-6765-877X Indu K. Dihingia https://orcid.org/0000-0002-4064-0446 Sheperd SDoeleman https://orcid.org/0000-0002-9031-0904

Sean Dougallo https://orcid.org/0000-0002-3769-1314 Sergio A. Dzib https://orcid.org/0000-0001-6010-6200 Ralph P.Eatough https://orcid.org/0000-0001-6196-4135 Razieh Emamio https://orcid.org/0000-0002-2791-5011 Heino Falcke® https://orcid.org/0000-0002-2526-6724 Joseph Farah https://orcid.org/0000-0003-4914-5625 Vincent L. Fish https://orcid.org/0000-0002-7128-9345 Edward Fomalonto https://orcid.org/0000-0002-9036-2747 H. Alyson Ford https://orcid.org/0000-0002-9797-0972 Marianna Foschi https://orcid.org/0000-0001-8147-4993 Raquel Fraga-Encinas https://orcid.org/0000-0002-5222-1361

Per Friberg® https://orcid.org/0000-0002-8010-8454 Christian M. Fromm https://orcid.org/0000-0002-

Antonio Fuentes https://orcid.org/0000-0002-8773-4933 Peter Galison https://orcid.org/0000-0002-6429-3872 Charles F.Gammie[®] https://orcid.org/0000-0001-7451-8935 Roberto García https://orcid.org/0000-0002-6584-7443 Olivier Gentaz® https://orcid.org/0000-0002-0115-4605 Boris Georgiev https://orcid.org/0000-0002-3586-6424 Ciriaco Goddi

https://orcid.org/0000-0002-2542-7743 Roman Goldo https://orcid.org/0000-0003-2492-1966 Arturo I. Gómez-Ruiz https://orcid.org/0000-0001-9395-1670

José L.Gómez[®] https://orcid.org/0000-0003-4190-7613 Minfeng Gu (顾敏峰) https://orcid.org/0000-0002-4455-6946

Mark Gurwell https://orcid.org/0000-0003-0685-3621 Kazuhiro Hada https://orcid.org/0000-0001-6906-772X Daryl Haggard https://orcid.org/0000-0001-6803-2138 Michael H. Hecht[®] https://orcid.org/0000-0002-4114-4583 Ronald Hespen https://orcid.org/0000-0003-1918-6098

Dirk Heumann[®] https://orcid.org/0000-0002-7671-0047 Luis C. Ho(何子山)[®] https://orcid.org/0000-0001-6947-5846

Paul Ho® https://orcid.org/0000-0002-3412-4306
Mareki Honma® https://orcid.org/0000-0003-4058-9000
Chih-Wei L. Huang® https://orcid.org/0000-0001-5641-3953
Lei Huang (黄磊》 https://orcid.org/0000-0002-1923-227X
Shiro Ikeda® https://orcid.org/0000-0002-2462-1448
C. M. Violette Impellizzeri® https://orcid.org/0000-0002-3443-2472

Makoto Inoue® https://orcid.org/0000-0001-5037-3989 Sara Issaou® https://orcid.org/0000-0002-5297-921X David J. James® https://orcid.org/0000-0001-5160-4486 Buell T. Jannuzi® https://orcid.org/0000-0002-1578-6582 Michael Jansse® https://orcid.org/0000-0001-8685-6544 Britton Jeter® https://orcid.org/0000-0003-2847-1712 Wu Jiang (江悟》 https://orcid.org/0000-0001-7369-3539 Alejandra Jiménez-Rosaleshttps://orcid.org/0000-0002-2662-3754

Michael D. Johnson https://orcid.org/0000-0002-4120-3029

Svetlana Jorstad https://orcid.org/0000-0001-6158-1708 Abhishek V. Joshio https://orcid.org/0000-0002-2514-5965 Taehyun Jungo https://orcid.org/0000-0001-7003-8643 Mansour Karamio https://orcid.org/0000-0001-7387-9333 Ramesh Karuppusamo https://orcid.org/0000-0002-5307-2919

Tomohisa Kawashima https://orcid.org/0000-0001-8527-0496

Garrett K. Keating https://orcid.org/0000-0002-3490-146X Mark Kettenis https://orcid.org/0000-0002-6156-5617 Dong-Jin Kim https://orcid.org/0000-0002-7038-2118 Jae-Young Kim https://orcid.org/0000-0001-8229-7183 Jongsoo Kim https://orcid.org/0000-0002-1229-0426 Junhan Kim https://orcid.org/0000-0002-4274-9373 Motoki Kino https://orcid.org/0000-0002-2709-7338 Jun Yi Koay https://orcid.org/0000-0002-7029-6658 Prashant Kocherlakota https://orcid.org/0000-0001-7386-7439

Patrick M. Koch https://orcid.org/0000-0003-2777-5861 Shoko Koyamahhttps://orcid.org/0000-0002-3723-3372 Carsten Kramehhttps://orcid.org/0000-0002-4908-4925 Joana A.Kramerhhttps://orcid.org/0009-0003-3011-0454 Michael Kramerhhttps://orcid.org/0000-0002-4175-2271 Thomas P.Krichbaumhhttps://orcid.org/0000-0002-4892-9586

Cheng-Yu Kuo® https://orcid.org/0000-0001-6211-5581 Noemi La Bella® https://orcid.org/0000-0002-8116-9427 Tod R. Lauer® https://orcid.org/0000-0003-3234-7247 Daeyoung Le® https://orcid.org/0000-0002-3350-5588 Sang-Sung Le® https://orcid.org/0000-0002-6269-594X Po Kin Leung® https://orcid.org/0000-0002-8802-8256 Aviad Levis® https://orcid.org/0000-0001-7307-632X Zhiyuan Li (李志远》 https://orcid.org/0000-0003-0355-6437

Rocco Lico® https://orcid.org/0000-0001-7361-2460
Greg Lindahl® https://orcid.org/0000-0002-6100-4772
Michael Lindqvist® https://orcid.org/0000-0002-3669-0715
Mikhail Lisakov® https://orcid.org/0000-0001-6088-3819
Jun Liu (刘俊) https://orcid.org/0000-0002-7615-7499
Kuo Liu ® https://orcid.org/0000-0002-2953-7376
Elisabetta Liuzz® https://orcid.org/0000-0003-0995-5201

Wen-Ping Lo® https://orcid.org/0000-0003-1869-2503
Andrei P. Lobanov® https://orcid.org/0000-0003-1622-1484
Laurent Loinard® https://orcid.org/0000-0002-5635-3345
Colin J. Lonsdale® https://orcid.org/0000-0003-4062-4654
Amy E. Lowitz ® https://orcid.org/0000-0002-4747-4276
Ru-Sen Lu (路如森》 https://orcid.org/0000-0002-7692-7967

Nicholas R.MacDonald[®] https://orcid.org/0000-0002-6684-8691

Jirong Mao (毛基荣) https://orcid.org/0000-0002-7077-7195

Nicola Marchili https://orcid.org/0000-0002-5523-7588 Sera Markoff[®] https://orcid.org/0000-0001-9564-0876 Daniel P. Marrone https://orcid.org/0000-0002-2367-1080 Alan P. Marscher https://orcid.org/0000-0001-7396-3332 Iván Martí-Vidal https://orcid.org/0000-0003-3708-9611 Satoki Matsushita https://orcid.org/0000-0002-2127-7880 Lynn D. Matthews https://orcid.org/0000-0002-3728-8082 Lia Medeiros https://orcid.org/0000-0003-2342-6728 Karl M. Menten® https://orcid.org/0000-0001-6459-0669 Daniel Michalik https://orcid.org/0000-0002-7618-6556 Izumi Mizuno https://orcid.org/0000-0002-7210-6264 Yosuke Mizuno https://orcid.org/0000-0002-8131-6730 James M.Moran https://orcid.org/0000-0002-3882-4414 Kotaro Moriyama https://orcid.org/0000-0003-1364-3761 Monika Moscibrodzka https://orcid.org/0000-0002-4661-6332

Wanga Mulaudzio https://orcid.org/0000-0003-4514-625X Cornelia Müller https://orcid.org/0000-0002-2739-2994 Hendrik Müller https://orcid.org/0000-0002-9250-0197 Alejandro Muso https://orcid.org/0000-0003-0329-6874 Gibwa Musokeo https://orcid.org/0000-0003-1984-189X Ioannis Myserliso https://orcid.org/0000-0003-3025-9497 Andrew Nadolskio https://orcid.org/0000-0001-9479-9957 Hiroshi Nagaio https://orcid.org/0000-0003-0292-3645 Neil M. Nagaro https://orcid.org/0000-0001-6920-662X Masanori Nakamuro https://orcid.org/0000-0001-6081-2420

Gopal Narayanan https://orcid.org/0000-0002-4723-6569 Iniyan Natarajan https://orcid.org/0000-0001-8242-4373 Antonios Nathanail https://orcid.org/0000-0002-1655-9912 Joey Neilsen https://orcid.org/0000-0002-8247-786X Roberto Nerio https://orcid.org/0000-0002-7176-4046 Chunchong Nio https://orcid.org/0000-0003-1361-5699 Aristeidis Noutson https://orcid.org/0000-0002-4151-3860 Michael A. Nowak https://orcid.org/0000-0002-4151-3860 Michael A. Nowak https://orcid.org/0000-0001-6923-1315 Junghwan Oho https://orcid.org/0000-0002-4991-9638 Hiroki Okino https://orcid.org/0000-0003-3779-2016 Héctor Olivares https://orcid.org/0000-0001-6833-7580 Gisela N.Ortiz-León https://orcid.org/0000-0002-2863-676X

Tomoaki Oyama https://orcid.org/0000-0003-4046-2923 Feryal Özel https://orcid.org/0000-0003-4413-1523 Daniel C.M. Palumbo https://orcid.org/0000-0002-7179-3816

Georgios Filippos Paraschoshttps://orcid.org/0000-0001-6757-3098

Jongho Park® https://orcid.org/0000-0001-6558-9053
Harriet Parsons® https://orcid.org/0000-0002-6327-3423
Nimesh Patel® https://orcid.org/0000-0002-6021-9421
Ue-Li Pen® https://orcid.org/0000-0003-2155-9578
Dominic W. Pesce® https://orcid.org/0000-0002-5278-9221

```
Richard Plambeck https://orcid.org/0000-0001-6765-9609
Oliver Porth https://orcid.org/0000-0002-4584-2557
Felix M. Pötzl https://orcid.org/0000-0002-6579-8311
Ben Prathe https://orcid.org/0000-0002-0393-7734
Jorge A. Preciado-Lópe https://orcid.org/0000-0002-4146-0113
```

Dimitrios Psaltis https://orcid.org/0000-0003-1035-3240 Hung-Yi Pu https://orcid.org/0000-0001-9270-8812 Venkatessh Ramakrishnanhttps://orcid.org/0000-0002-9248-086X

Ramprasad Ra® https://orcid.org/0000-0002-1407-7944 Mark G. Rawlings® https://orcid.org/0000-0002-6529-202X Alexander W.Raymond® https://orcid.org/0000-0002-5779-4767

Luciano Rezzolla https://orcid.org/0000-0002-1330-7103
Angelo Ricarte https://orcid.org/0000-0001-5287-0452
Bart Ripperda https://orcid.org/0000-0002-7301-3908
Freek Roelof https://orcid.org/0000-0001-5461-3687
Alan Roger https://orcid.org/0000-0003-1941-7458
Cristina Romero-Cañizal https://orcid.org/0000-0001-6301-9073

Eduardo Roso https://orcid.org/0000-0001-9503-4892 Arash Roshanineshat https://orcid.org/0000-0002-8280-9238

Alan L. Roy https://orcid.org/0000-0002-1931-0135 Ignacio Ruizhhttps://orcid.org/0000-0002-0965-5463 Chet Ruszczykhttps://orcid.org/0000-0001-7278-9707 Kazi L. J. Rygl https://orcid.org/0000-0003-4146-9043 Salvador Sánchezhttps://orcid.org/0000-0002-8042-5951 David Sánchez-Argüelleshttps://orcid.org/0000-0002-7344-9920

Miguel Sánchez-Portal https://orcid.org/0000-0003-0981-9664

Mahito Sasada https://orcid.org/0000-0001-5946-9960
Kaushik Satapathy https://orcid.org/0000-0003-0433-3585
Tuomas Savolainen https://orcid.org/0000-0001-6214-1085
Jonathan Schonfeld https://orcid.org/0000-0002-8909-2401
Karl-Friedrich Schusten https://orcid.org/0000-0003-2890-9454

Lijing Shao https://orcid.org/0000-0002-1334-8853 Zhiqiang Shen (沈志强) https://orcid.org/0000-0003-3540-8746

Des Small® https://orcid.org/0000-0003-3723-5404
Bong Won Sohn® https://orcid.org/0000-0002-4148-8378
Jason SooHo® https://orcid.org/0000-0003-1938-0720
León David Sosapanta Salashttps://orcid.org/0000-0003-1979-6363

Kamal Soucca® https://orcid.org/0000-0001-7915-5272
Joshua SStanway® https://orcid.org/0009-0003-7659-4642
He Sun (孙赫》 https://orcid.org/0000-0003-1526-6787
Fumie Tazak® https://orcid.org/0000-0003-0236-0600
Alexandra J.Tetarenko® https://orcid.org/0000-0003-3906-4354

Paul Tiede® https://orcid.org/0000-0003-3826-5648
Remo P. J. Tilanu® https://orcid.org/0000-0002-6514-553X
Michael Titus® https://orcid.org/0000-0001-9001-3275
Pablo Torne® https://orcid.org/0000-0001-8700-6058
Teresa Toscan® https://orcid.org/0000-0003-3658-7862
Efthalia Traianou® https://orcid.org/0000-0002-1209-6500
Sascha Tripp® https://orcid.org/0000-0003-0465-1559
Matthew Turk® https://orcid.org/0000-0002-5294-0198
Ilse van Bemmel® https://orcid.org/0000-0001-5473-2950

```
Huib Jan van Langevelde https://orcid.org/0000-0002-0230-5946
```

Daniel R. van Rossum https://orcid.org/0000-0001-7772-6131

Jesse Vos https://orcid.org/0000-0003-3349-7394
Jan Wagnen https://orcid.org/0000-0003-1105-6109
Derek Ward-Thompson https://orcid.org/0000-00031140-2761

John Wardle® https://orcid.org/0000-0002-8960-2942 Jasmin E.Washington® https://orcid.org/0000-0002-7046-0470

Jonathan Weintroub https://orcid.org/0000-0002-4603-5204

Robert Wharton® https://orcid.org/0000-0002-7416-5209 Maciek Wielgus® https://orcid.org/0000-0002-8635-4242 Kaj Wiik ® https://orcid.org/0000-0002-0862-3398 Gunther Witzel® https://orcid.org/0000-0003-2618-797X Michael F. Wondrak® https://orcid.org/0000-0002-6894-1072

Nitika Yadlapalli https://orcid.org/0000-0003-3255-4617 Paul Yamaguchi https://orcid.org/0000-0002-6017-8199 Aristomenis Yfantis https://orcid.org/0000-0002-3244-7072

Doosoo Yoon® https://orcid.org/0000-0001-8694-8166
André Young® https://orcid.org/0000-0003-0000-2682
Ken Young® https://orcid.org/0000-0002-3666-4920
Ziri Younsi ® https://orcid.org/0000-0001-9283-1191
Wei Yu (于威)® https://orcid.org/0000-0002-5168-6052
Feng Yuan (袁峰) https://orcid.org/0000-0003-3564-6437
Ye-Fei Yuan (袁业飞) https://orcid.org/0000-0002-7330-4756

J. Anton Zensus https://orcid.org/0000-0001-7470-3321 Shuo Zhang https://orcid.org/0000-0002-2967-790X Guang-Yao Zhao https://orcid.org/0000-0002-4417-1659 Shan-Shan Zhao (赵杉杉)https://orcid.org/0000-0002-9774-3606

Mahdi Najafi-Ziyazi[®] https://orcid.org/0009-0008-0922-3995

Agol, E. 2000, ApJL, 538, L121

References

Anantua, R., Emami, R., Loeb, A., & Chael, A. 2020, ApJ, 896, 30 The Astropy Collaboration, Robitaille, T. P., Tollerud, E. J., et al. 2013, A&A, Ball, D., Sironi, L., & Özel, F. 2018, ApJ, 862, 80 Bardeen, J. M. 1973, Les Astres Occlus (New York: Gordon & Breach), 215 Bisnovatyi-Kogan, G. S., & Ruzmaikin, A. A. 1976, Ap&SS, 42, 401 Blandford, R. D., & Znajek, R. L. 1977, MNRAS, 179, 433 Bower, G. C., Broderick, A., Dexter, J., et al. 2018, ApJ, 868, 101 Broderick, A. E., Fish, V. L., Doeleman, S. S., & Loeb, A. 2009, ApJ, 697, 45 Broderick, A. E., Fish, V. L., Doeleman, S. S., & Loeb, A. 2011, ApJ, 735, 110 Broderick, A. E., Fish, V. L., Johnson, M. D., et al. 2016, ApJ, 820, 137 Broderick, A. E., Gold, R., Karami, M., et al. 2020, ApJ, 897, 139 Broderick, A. E., Johannsen T., Loeb, A., & Psaltis, D. 2014, ApJ, 784, 7 Bromley, B. C., Melia, F., & Liu, S. 2001, ApJL, 555, L83 Bronzwaer, T., Davelaar, J., Younsi, Z., et al. 2018, A&A, 613, A2 Bronzwaer, T., Younsi, Z., Davelaar, J., & Falcke, H. 2020, A&A, 641, A126 Chael, A., Lupsasca, A., Wong, G. N., & Quataert, E. 2023, ApJ, 958, 65 Chael, A., Rowan, M., Narayan, R., Johnson, M., & Sironi, L. 2018, MNRAS, Chael, A., Johnson, M. D., Narayan, R., et al. 2016, ApJ, 829, 11 Chatterjee K., Younsi, Z., Liska, M., et al. 2020, MNRAS, 499, 362

Kunz, M. W., Stone, J. M., & Quataert, E. 2016, PhRvL, 117, 235101

```
Conroy, N. S., Bauböck, M., Dhruv, V., et al. 2023, ApJ, 951, 46
                                                                              Levis, A., Chael, A. A., Bouman, K. L., Wielgus, M., & Srinivasan, P. P. 2023,
Cruz-Osorio, A., Fromm, C. M., Mizuno, Y., et al. 2022, NatAs, 6, 103
                                                                                 arXiv:2310.07687
Davelaar, J., Mościbrodzka, M., Bronzwaer, T., & Falcke, H. 2018, A&A,
                                                                              Liska, M., Hesp, C., Tchekhovskoy A., et al. 2018, MNRAS, 474, L81
                                                                              Liska, M. T. P., Chatterjee K., Issa, D., et al. 2022, ApJS, 263, 26
  612. A34
                                                                              Luminet, J.-P. 1979, A&A, 75, 228
Davelaar, J., Olivares, H., Porth, O., et al. 2019, A&A, 632, A2
                                                                              Mahadevan R., & Quataert, E. 1997, ApJ, 490, 605
De Villiers, J.-P., Hawley, J. F., & Krolik, J. H. 2003, ApJ, 599, 1238
Dexter, J. 2016, MNRAS, 462, 115
                                                                              Mao, S. A., Dexter, J., & Quataert, E. 2017, MNRAS, 466, 4307
Dexter, J., Jiménez-Rosales,A., Ressler,S. M., et al. 2020, MNRAS,
                                                                              Markoff, S., Bower, G. C., & Falcke, H. 2007, MNRAS, 379, 1519
                                                                              Markoff, S., Falcke, H., Yuan, F., & Biermann, P. L. 2001, A&A, 379, L13
                                                                              McKinney, W. 2010, in Proc. 9th Python in Science Conf., ed.
Dibi, S., Drappeau, S., Fragile, P. C., Markoff, S., & Dexter, J. 2012, MNRAS,
   426, 1928
                                                                                 S. van der Walt & J. Millman, 51
                                                                              Medeiros, L., Chan, C.-K., Narayan, R., Özel, F., & Psaltis, D. 2022, ApJ,
Dihingia, I. K., Mizuno, Y., Fromm, C. M., & Rezzolla, L. 2023, MNRAS,
                                                                                 924.46
  518,405
Emami, R., Anantua, R., Chael, A. A., & Loeb, A. 2021, ApJ, 923, 272
                                                                              Meyrand, R., Kanekar, A., Dorland, W., & Schekochihin, A. A. 2019, PNAS,
Emami, R., Anantua, R., Ricarte, A., et al. 2023a, Galax, 11, 11
                                                                                 116, 1185
Emami, R., Ricarte, A., Wong, G. N., et al. 2023b, ApJ, 950, 38
                                                                              Mizuno, Y., Fromm, C. M., Younsi, Z., et al. 2021, MNRAS, 506, 741
Event Horizon Telescope Collaboration Akiyama, K., Alberdi, A., et al.
                                                                              Mościbrodzka, M., Dexter, J., Davelaar, J., & Falcke, H. 2017, MNRAS,
  2022a, ApJL, 930, L12
                                                                                 468, 2214
Event Horizon Telescope Collaboration Akiyama, K., Alberdi, A., et al.
                                                                              Mościbrodzka, M., & Falcke, H. 2013, A&A, 559, L3
  2022b, ApJL, 930, L13
                                                                              Mościbrodzka, M., Falcke, H., & Shiokawa, H. 2016, A&A, 586, A38
Event Horizon Telescope Collaboration Akiyama, K., Alberdi, A., et al.
                                                                              Mościbrodzka, M., & Gammie, C. F. 2018, MNRAS, 475, 43
  2022c, ApJL, 930, L14
                                                                              Mościbrodzka, M., Janiuk, A., & De Laurentis, M. 2021, MNRAS, 508, 4282
                                                                              Murchikova, L., White, C. J., & Ressler, S. M. 2022, ApJL, 932, L21
Event Horizon Telescope Collaboration Akiyama, K., Alberdi, A., et al.
  2022d, ApJL, 930, L15
                                                                              Narayan, R., Igumenshchev, I. V., & Abramowicz, M. A. 2003, PASJ, 55, L69
                                                                              Narayan, R., Sadowski, A., Penna, R. F., & Kulkarni, A. K. 2012, MNRAS,
Event Horizon Telescope Collaboration Akiyama, K., Alberdi, A., et al.
   2022e, ApJL, 930, L16
                                                                                 426, 3241
Event Horizon Telescope Collaboration, Akiyama, K., Alberdi, A., et al. 2022f, Noble, S. C., Leung, P. K., Gammie, C. F., & Book, L. G. 2007, CQGra,
   ApJL, 930, L17
                                                                                 24, S259
Event Horizon Telescope Collaboration, Akiyama, K., Alberdi, A., et al. 2023,
                                                                              Olivares, H., Porth, O., Davelaar, J., et al. 2019, A&A, 629, A61
   ApJI 957 L20
                                                                              Özel, F., Psaltis, D., & Narayan, R. 2000, ApJ, 541, 234
                                                                              Palumbo, D. C. M., Gelles, Z., Tiede, P., et al. 2022, ApJ, 939, 107
Event Horizon Telescope Collaboration, Akiyama, K., Alberdi, A., et al. 2024,
                                                                              Palumbo, D. C. M., Wong, G. N., & Prather, B. S. 2020, ApJ, 894, 156
   ApJL, 964, L25
Event Horizon Telescope CollaborationAkiyama, K., Algaba, J. C., et al.
                                                                              Pordes, R., Petravick, D., Kramer, B., et al. 2007, JPhCS, 78, 012057
   2021a, ApJL, 910, L12
                                                                              Porth, O., Chatterjee K., Narayan, R., et al. 2019, ApJS, 243, 26
Event Horizon Telescope CollaborationAkiyama, K., Algaba, J. C., et al.
                                                                              Porth, O., Olivares, H., Mizuno, Y., et al. 2017, ComAC, 4, 1
                                                                              Prather, B., Wong, G., Dhruv, V., et al. 2021, JOSS, 6, 3336
   2021b, ApJL, 910, L13
Falcke, H., Mannheim, K., & Biermann, P. L. 1993, A&A, 278, L1
                                                                              Pu, H.-Y., Akiyama, K., & Asada, K. 2016, ApJ, 831, 4
Falcke,H., & Markoff, S. 2000, A&A, 362, 113
                                                                              Pu, H.-Y., & Broderick, A. E. 2018, ApJ, 863, 148
Falcke, H., Melia, F., & Agol, E. 2000, ApJL, 528, L13
                                                                              Qiu, R., Ricarte, A., Narayan, R., et al. 2023, MNRAS, 520, 4867
Farah, J., Galison, P., Akiyama, K., et al. 2022, ApJL, 930, L18
                                                                              Quataert E., & Gruzinov, A. 2000, ApJ, 545, 842
Fishbone L. G., & Moncrief, V. 1976, ApJ, 207, 962
                                                                              Ressler, S. M., Quataert, E., & Stone, J. M. 2019, MNRAS, 482, L123
Fragile, P. C., Blaes, O. M., Anninos, P., & Salmonson, J. D. 2007, ApJ,
                                                                              Ressler, S. M., White, C. J., & Quataert, E. 2023, MNRAS, 521, 4277
  668,417
                                                                              Ricarte, A., Palumbo, D. C. M., Narayan, R., Roelofs, F., & Emami, R. 2022,
Fromm, C. M., Cruz-Osorio, A., Mizuno, Y., et al. 2022, A&A, 660, A107
                                                                                  ApJL, 941, L12
                                                                              Ricarte, A., Prather, B. S., Wong, G. N., et al. 2020, MNRAS, 498, 5468
Gammie, C. F., McKinney, J. C., & Tóth, G. 2003, ApJ, 589, 444
GRAVITY Collaboration, Abuter, R., Amorim, A., et al. 2018, A&A, 618,
                                                                              Ricarte, A., Qiu, R., & Narayan, R. 2021, MNRAS, 505, 523
                                                                              Ricarte, A., Tiede, P., Emami, R., Tamar, A., & Natarajan, P. 2023, Galax,
GRAVITY Collaboration, Bauböck, M., Dexter, J., et al. 2020a, A&A,
  635, A143
                                                                              Riquelme, M. A., Quataert, E., & Verscharen, D. 2015, ApJ, 800, 27
GRAVITY Collaboration, Jiménez-Rosales, A., Dexter, J., et al. 2020b, A&A,
                                                                              Ryan, B. R., Ressler S. M., Dolence, J. C., et al. 2017, ApJL, 844, L24
                                                                              Sądowski, A., Narayan, R., Penna, R., & Zhu, Y. 2013, MNRAS, 436, 3856
Harris, C. R., Millman, K. J., van der Walt, S. J., et al. 2020, Natur, 585, 357
                                                                              Sfiligoi, I., Bradley, D. C., Holzman, B., et al. 2009, in 2009 WRI World
Hilbert, D. 1917, Nachrichten von der Königlichen Gesellschaft der
                                                                                 Congress on Computer Science and Information Engineering 2 (New York:
   Wissenschaften zu Göttingen-Mathematisch-physikalischeKlasse
                                                                                 IEEE), 428
                                                                              Sironi, L., & Narayan, R. 2015, ApJ, 800, 88
   (Berlin: Weidmannsche Buchhandlung), 53
Hunter, J. D. 2007, CSE, 9, 90
                                                                              Su, K.-Y., Hopkins, P. F., Bryan, G. L., et al. 2021, MNRAS, 507, 175
Igumenshchev, I. V., Narayan, R., & Abramowicz, M. A. 2003, ApJ, 592, 1042
                                                                              Tchekhovskoy, A., Narayan, R., & McKinney, J. C. 2011, MNRAS, 418, L79
Issaoun,S., Johnson,M. D., Blackburn,L., et al. 2019, ApJ, 871, 30
                                                                              The Astropy CollaborationPrice-WhelanA. M., Sipőcz,B. M., et al. 2018,
Issaoun,S., Johnson,M. D., Blackburn,L., et al. 2021, ApJ, 915, 99
                                                                                 AJ, 156, 123
Jaroszynski, M., & Kurpiewski, A. 1997, A&A, 326, 419
                                                                              Tiede, P., Pu, H.-Y., Broderick, A. E., et al. 2020, ApJ, 892, 132
Jiménez-Rosales, & Dexter, J. 2018, MNRAS, 478, 1875
                                                                              Tsunetoe, Y., Mineshige, S., Ohsuga, K., Kawashima, T., & Akiyama, K.
Johnson, M. D., Lupsasca, A., Strominger, A., et al. 2020, SciA, 6, eaaz1310
                                                                                 2021, PASJ, 73, 912
                                                                              Vasyliunas, V. M. 1968, JGR, 73, 2839
Johnson, M. D., Narayan, R., Psaltis, D., et al. 2018, ApJ, 865, 104
Jones, E., Oliphant, T., Peterson, P., et al. 2001, SciPy: Open Source Scientifid/incent, F. H., Gralla, S. E., Lupsasca A., & Wielgus, M. 2022, A&A,
  Tools for Python,http://www.scipy.org/
                                                                                 667. A170
Jones,T. W., & Hardee, P. E. 1979, ApJ, 228, 268
                                                                              Vos, J., Mościbrodzka, M. A., & Wielgus, M. 2022, A&A, 668, A185
Jones, T. W., & O'Dell, S. L. 1977, ApJ, 214, 522
                                                                              Wielgus, M., Issaoun, S., Martí-Vidal, I., et al. 2024, A&A, 682, A97
Kluyver, T., Ragan-Kelley, B., Pérez, F., et al. 2016, in Positioning and Power Wielgus, M., Marchili, N., Martí-Vidal, I., et al. 2022a, ApJL, 930, L19
   in Academic Publishing: Player Agents and Agenda cd. F. Loizides &
                                                                              Wielgus, M., Moscibrodzka, M., Vos, J., et al. 2022b, A&A, 665, L6
                                                                              Wong, G. N., & Gammie, C. F. 2022, ApJ, 937, 60
   B. Schmidt (Amsterdam: IOS Press), 87
                                                                              Wong, G. N., Prather, B. S., Dhruv, V., et al. 2022, ApJS, 259, 64
Knollmüller, J., Arras, P., & Enßlin, T. 2023, arXiv:2310.16889
Kunz, M. W., Schekochihin, A. A., & Stone, J. M. 2014, PhRvL, 112, 205003
                                                                              Xiao, F. 2006, PPCF, 48, 203
```

Yoon, D., Chatterjee,K., Markoff, S. B., et al. 2020, MNRAS, 499, 3178

The Event Horizon Telescope Collaboration,

```
Kazunori Akiyama<sup>1,2,3</sup>, Antxon Alberdi<sup>4</sup>, Walter Alef, Juan Carlos Algaba, Richard Anantua<sup>7,8</sup>, Keiichi Asada,
                                                    Rebecca Azulay 10,110, Uwe Bach Anne-Kathrin Baczk 120, David Ball 3, Mislav Baloković 40,
                                    Bidisha Bandyopadhyayo, John Barretto, Michi Bauböck 60, Bradford A. Benson 7,180, Dan Bintley 19,20,
                   Lindy Blackburn<sup>3,7</sup>, Raymond Blundelo, Katherine L.Bouman<sup>1</sup>, Geoffrey C.Bower<sup>22,23</sup>, Hope Boyce<sup>4,25</sup>,
                    Michael Breme<sup>26</sup>, Christiaan D.Brinkerink<sup>27</sup>, Roger Brissenden<sup>7</sup>, Silke Britzen<sup>5</sup>, Avery E. Broderick<sup>28,29,30</sup>,
                                                                Dominique Broguiere , Thomas Bronzwaer, Sandra Bustamante, Do-Young Byun 32,330,
        Koushik Chatterjee 70, Shami Chatterjee 1, Ming-Tang Chen (陈永军),420, Xiaopeng Chen 60,
                                            Ilje Cho<sup>4,32,43</sup>, Pierre Christian Nicholas S.Conroy, John E.Conway, James M.Cordes, James M.Cordes,
Thomas M. Crawford<sup>8,34</sup>, Geoffrey B. Crew, Alejandro Cruz-Osori<sup>6,47</sup>, Yuzhu Cui (崔玉竹<sup>4</sup>,49,49, Rohan Dahal<sup>6</sup>,
                                       Jordy Davelaar<sup>7,50,51</sup>, Mariafelicia De Laurentis<sup>7,52,53</sup>, Roger Deane<sup>4,55,59</sup>, Jessica Dempse<sup>9,20,57</sup>,
                                  Gregory Desvignes<sup>58</sup>, Jason Dexte<sup>9</sup>, Vedant Dhru<sup>16</sup>, Indu K. Dihingia<sup>49</sup>, Sheperd SDoeleman<sup>7,7</sup>
         Sean Dougali<sup>3</sup>, Sergio A. Dzib<sup>5,26</sup>, Ralph P. Eatough<sup>6,60</sup>, Razieh Emamili, Heino Falcke<sup>7</sup>, Joseph Farani, 62,
                                   Vincent L. Fish<sup>1</sup>, Edward Fomalon<sup>2</sup>, H. Alyson Ford<sup>3</sup>, Marianna Foschi, Raquel Fraga-Encina<sup>3</sup>,
                        William T. Freemaĥ<sup>4,65</sup>, Per Friberg<sup>9,20</sup>, Christian M. Fromm<sup>5,47,66</sup>, Antonio Fuente<sup>4</sup>. Peter Galison<sup>67,68</sup>.
                         Charles F.Gammie 6,45,69, Roberto García, Olivier Genta 6, Boris Georgie 3, Ciriaco Godd 70,71,72,73,
                            Roman Gold<sup>4</sup><sup>6</sup>, Arturo I. Gómez-Rui<sup>Z5,76</sup><sup>6</sup>, José L.Góme<sup>2</sup><sup>6</sup>, Minfeng Gu (顾敏峰<sup>4</sup>),<sup>77</sup><sup>6</sup>, Mark Gurwell<sup>7</sup><sup>6</sup>,
         Kazuhiro Hada Daryl Haggard Kazuhiro Hada Roman Haggard Ro
               Luis C. Ho (何子山<sup>81,82</sup>, Paul Ho<sup>9,19,20</sup>, Mareki Honma<sup>78,79,83</sup>, Chih-Wei L. Huang<sup>6</sup>, Lei Huang (黄磊<sup>1),77</sup>,
                        David H. Hughes<sup>75</sup>, Shiro Ikeda<sup>3,84,85,86</sup>, C. M. Violette Impellizzeri<sup>63,87</sup>, Makoto Inoue<sup>6</sup>, Sara Issaou<sup>7</sup>
                                                 David J. Jame<sup>§8,89</sup>, Buell T. Jannuz<sup>13</sup>, Michael Jansse<sup>77</sup>, Britton Jete<sup>9</sup>, Wu Jiang ( 江悟<sup>1</sup>).
      Alejandra Jiménez-Rosafe, Michael D. Johnson, Svetlana Jorstado, Abhishek V. Joshi 60, Taehyun Jung 32,330,
                Mansour Karami<sup>8,29</sup>, Ramesh Karuppusam, Tomohisa Kawashim<sup>1</sup>, Garrett K.Keating, Mark Kettenis<sup>2</sup>,
                               Dong-Jin Kim<sup>5</sup>, Jae-Young Kim<sup>5,93</sup>, Jongsoo Kim<sup>32</sup>, Junhan Kim<sup>94</sup>, Motoki Kino<sup>2,95</sup>, Jun Yi Koay<sup>9</sup>,
                                       Prashant Kocherlakota, Yutaro Kofuji<sup>78,83</sup>, Patrick M. Koch<sup>9</sup>, Shoko Koyama, Carsten Krame, Ca
Joana A. Kramḗno, Michael Kramḗno, Thomas P. Krichbauno, Cheng-Yu Kuo<sup>97</sup>no, Noemi La Bella not R. Lauero, Tod R. Lauero, Cheng-Yu Kuo not R. Lauero, Noemi La Bella not R. Lauero, Cheng-Yu Kuo not R. Lauero, Noemi La Bella not Republication (Notation and Notation a
Daeyoung Leeo, Sang-Sung Leeo, Po Kin Leung, Aviad Levis, Zhiyuan Li (李志远), Rocco Lico, Rocco Lico, Aviad Levis, Zhiyuan Li (李志远), Rocco Lico, Rocco 
                       Greg Lindahl , Michael Lindgvist , Mikhail Lisakov , Jun Liu ( 刘俊 , Kuo Liu , Liu ,
               Wen-Ping Logo, Andrei P. Lobanovo, Laurent Loinardo, Colin J. Lonsdaldo, Amy E. Lowitz 13, Ru-Sen Lu
        路如森<sup>5</sup>,41,106, Nicholas R. MacDonalo, Jirong Mao (毛基荣)7,108,106, Nicola Marchill,103, Sera Markoff10,1116,
                          Lia Medeiros 112,1540, Karl M. Menter 0, Daniel Michalik 18,1130, Izumi Mizuno 19,200, Yosuke Mizuno 47,49,1140,
           James M.Moran<sup>3,7</sup>, Kotaro Moriyama<sup>4,47,78</sup>, Monika Moscibrodzka<sup>7</sup>, Wanga Mulaudzi<sup>10</sup>, Cornelia Müller<sup>5,27</sup>,
                                   Hendrik Müller 10, Alejandro Mus 10,110, Gibwa Musoke 7,1100, Ioannis Myserlis 150, Andrew Nadolsk 150,
                                  Hiroshi Naga<sup>7,79</sup>, Neil M. Naga<sup>75</sup>, Masanori Nakamu<sup>9</sup>, Gopal Narayana<sup>3</sup>, Iniyan Natarajah<sup>7</sup>,
                   Antonios Nathana 17,117, Santiago Navarro Fuentes, Joey Neilsen 18, Roberto Ner 6, Chunchong N 28,29,30,
                                          Aristeidis Noutsoso, Michael A. Nowak<sup>119</sup>, Junghwan Oho, Hiroki Okino<sup>78,83</sup>, Héctor Olivares<sup>7</sup>,
Gisela N. Ortiz-Leóñ<sup>75</sup>, Tomoaki Oyama<sup>8</sup>, Feryal Özel<sup>20</sup>, Daniel C. M. Palumbð<sup>7</sup>, Georgios Filippos Parascho, Jongho Park<sup>21</sup>, Harriet Parson<sup>9,20</sup>, Nimesh Patello, Ue-Li Per<sup>9,28,122,123,12</sup>, Dominic W. Pesce<sup>7</sup>, Vincent Piétu<sup>6</sup>,
                                    Richard Plambeck Aleksandar PopStefanija Oliver Porth Pelix M. Pötz B. Ben Prathe Ben Prathe PopStefanija Oliver Porth PopStefanija Oliver PopStefanija Oliver Porth PopStefanija Oliver PopStefan
                               Jorge A. Preciado-Lópezo, Dimitrios Psaltis Ps
Ramprasad Rato, Mark G. Rawling 19,20,13 to, Alexander W. Raymond to, Luciano Rezzolla, 132,13 to, Angelo Ricarte, and Company of the Raymond to, Luciano Rezzolla, 132,13 to, Angelo Ricarte, and Company of the Raymond to, Luciano Rezzolla, 132,13 to, Angelo Ricarte, and Company of the Raymond to, Luciano Rezzolla, 132,13 to, Angelo Ricarte, and Company of the Raymond to, Luciano Rezzolla, 132,13 to, Angelo Ricarte, and Company of the Raymond to, Luciano Rezzolla, 132,13 to, Angelo Ricarte, and Company of the Raymond to, Angelo Ricarte, and Angelo Ricarte, and
                          Bart Ripperda<sup>8,122,123,13</sup>, Freek Roelofs<sup>7,27</sup>, Alan Rogers, Cristina Romero-Cañizal<sup>6</sup>, Eduardo Ros,
              Arash Roshanineshato, Helge Rottmann, Alan L. Royoo, Ignacio Ruiz<sup>15</sup>, Chet Ruszczyko, Kazi L. J. Rygl<sup>103</sup>,
                                    Salvador Sánchez-Portal (5,760), David Sánchez-Argüelle (5,760), Miguel Sánchez-Portal (6,135,1360).
   Kaushik Satapathy , Tuomas Savolaine 130,137, F. Peter Schloer , Jonathan Schonfe , Karl-Friedrich Schuster ,
                                    Lijing Shao<sup>5,82</sup>, Zhiqiang Shen (沈志強<sup>1</sup>)<sup>42</sup>, Des Smalf<sup>2</sup>, Bong Won Sohn<sup>2,33,43</sup>, Jason SooHo<sup>1</sup>,
         León David Sosapanta Salasto, Kamal Souccalto, Joshua SStanway<sup>38</sup>to, He Sun (孙赫<sup>1</sup>)<sup>9,140</sup>to, Fumie Tazaki<sup>8</sup>to, Alexandra J.Tetarenko<sup>41</sup>to, Paul Tiede<sup>3,7</sup>to, Remo P.J. Tilanus<sup>13,27,87,144</sup>to, Michael Titus<sup>1</sup>to, Pablo Torne<sup>115</sup>to,
                   Teresa Toscano, Efthalia Traiano , Tyler Trent, Sascha Trippe, Matthew Turk, Ilse van Bemme, Ilse van Bemme, Sascha Trippe, Matthew Turk, Ilse van Bemme, Ilse
     Huib Jan van Langevelde. 92,144, Daniel R. van Rossum, Jesse Vos 10, Jan Wagne Derek Ward-Thompson Derek W
John Wardle Jasmin E. Washington Jonathan Weintroub Donathan Weintroub Marton Marton Maciek Wielgus Naj Wiik 146, Robert Wharton Naj Wiele Naj Wiik 146, Robert Wharton Naj Wiik 146, Robert White Naj Wiik 146, Robert White Naj Wiik 146, Robe
```

```
Paul Yamaguchio, Aristomenis Yfantiŝ<sup>7</sup>, Doosoo Yoon<sup>10</sup>, André Young<sup>7</sup>, Ken Young<sup>7</sup>, Ziri Younsi<sup>47,150</sup>,
              Wei Yu (于威疗, Feng Yuan (袁峰疗, Ye-Fei Yuan (袁业飞疗, J. Anton Zensus, Shuo Zhang, Shuo Zhang,
                                         Guang-Yao Zhao 50, Shan-Shan Zhao (赵杉 杉 10, and Mahdi Najafi-Ziyazi 100
                                       <sup>1</sup> Massachusetts Institute of Technology Haystack Observa@yMillstone Road,Westford,MA 01886, USA
                                                      National Astronomical Observatory of Japan 21-1 OsawaMitaka, Tokyo 181-8588, Japan
                                                    <sup>3</sup> Black Hole Initiative at Harvard University20 Garden StreetCambridge,MA 02138, USA
                                               <sup>4</sup> Instituto de Astrofísica de Andalucía-CSIGlorieta de la Astronomía s/nE-18008 Granadapain
                                                          Max-Planck-Institut für Radioastronomiauf dem Hügel 69,D-53121 Bonn,Germany
                                                  6 Department of Physics aculty of Science Universiti Malaya, 50603 Kuala Lumpur Malaysia
                                                <sup>7</sup> Center for AstrophysicsHarvard & Smithsonian60 Garden StreetCambridgeMA 02138, USA
                       <sup>8</sup> Department of Physics & Astronomy, he University of Texas at San Antonio, ne UTSA Circle, San Antonio, TX 78249, USA
 9 Institute of Astronomy and Astrophysics cademia Sinica 11F of Astronomy-Mathematics Building S/NTU No. 1, Sec.4, Roosevelt Road Taipei 10617,
                             Taiwan, R.O.C.

Taiwan, R.O.C.

Taiwan, R.O.C.

Taiwan, R.O.C.

Noliner 50, E-46100 Burjassof/aléncia, Spain
                                       Observatori AstronómicUniversitat de ValénciaC. Catedrático José Beltrán £-46980 PaternaValéncia, Spain
                12 Department of SpaceEarth and EnvironmentChalmers University of TechnologyOnsala Space ObservatoryE-43992 OnsalaSweden
                             Steward Observatory and Department of Astronorbyniversity of Arizona, 933 N. Cherry Avenue, Tucson, AZ 85721, USA

14 Yale Center for Astronomy & Astrophysics ale University, 52 Hillhouse AvenueNew Haven, CT 06511, USA

15 Astronomy Department Universidad de Concepción asilla 160-C, Concepción Chile
                                                 <sup>16</sup> Department of Physics University of Illinois, 1110 West Green Street Irbana, IL 61801, USA
                                                          Fermi National Accelerator Laborator MS209, P.O. Box 500, Batavia, IL 60510, USA
                              <sup>18</sup>Department of Astronomy and Astrophysidshiversity of Chicago 5640 South Ellis AvenueChicago,IL 60637, USA
                                                                        East Asian Observator 660 N. A'ohoku Place, Hilo, HI 96720, USA
                                                       <sup>20</sup> James Clerk Maxwell Telescope (JCMT6)60 N. A'ohoku Place,Hilo, HI 96720, USA
                                                 <sup>21</sup>California Institute of Technology1200 East California Boulevard?asadenaCA 91125,USA
                                          <sup>22</sup> Institute of Astronomy and AstrophysicsAcademia Sinica645 N. A'ohoku Place,Hilo, HI 96720, USA
                               Department of Physics and Astronomyniversity of Hawaii at Manoa2505 Correa Road, Honolulu, HI 96822, USA
                                                   Department of PhysicsMcGill University, 3600 rue University, Montréal, QC H3A 2T8, Canada
                                                          Trottier Space Institute at McGill3550 rue University, Montréal, QC H3A 2A7, Canada
                                    <sup>26</sup> Institut de Radioastronomie Millimétrique (IRAM)300 rue de la Piscine—38406 Saint Martin d'Hére—rance
<sup>27</sup> Department of Astrophysics, Institute for Mathematics, Astrophysics and Particle Physics (IMAPP), Radboud University, P.O. Box 9010, 6500 GL Nijmegen, The
                                                                                                                    Netherlands
                                            <sup>28</sup> Perimeter Institute for Theoretical Physicst Caroline Street NorthWaterloo,ON N2L 2Y5, Canada
                        Department of Physics and AstronomyIniversity of Waterloo,200 University Avenue WestWaterloo,ON N2L 3G1, Canada

30 Waterloo Centre for AstrophysicsUniversity of Waterloo,Waterloo,ON N2L 3G1, Canada

31 Department of AstronomyIniversity of MassachusettsAmherst MA 01003, USA
                                                              Department of AstronomyUniversity of MassachusettAmherst, MA 01003, USA
                                 <sup>32</sup> Korea Astronomy and Space Science Instituted edeok-daero 776/, useong-guDaejeon 34055 Republic of Korea
                                             <sup>3</sup>University of Science and Technolog@ajeong-ro 217Yuseong-guDaejeon 34113Republic of Korea
                                 34 Kavli Institute for Cosmological Physics Iniversity of Chicago, 5640 South Ellis Avenue Chicago, IL 60637, USA
                                                  Department of Physics University of Chicago, 5720 South Ellis Avenue Chicago, IL 60637, USA
                                               <sup>36</sup>Enrico Fermi Institute University of Chicago 5640 South Ellis AvenueChicago,IL 60637, USA
                                                         Princeton Gravity Initiative, Jadwin Hall, Princeton University Princeton, NJ 08544, USA
                                                Data Science Institute Ins
                                            <sup>39</sup> Program in Applied Mathematics Iniversity of Arizona, 617 N. Santa Rita, Tucson, AZ 85721, USA
                                             <sup>40</sup> Cornell Center for Astrophysics and Planetary Sciencernell University, Ithaca, NY 14853, USA
                    <sup>41</sup>Shanghai Astronomical Observato@hinese Academy of Science®0 Nandan RoadShanghai 20003@eople's Republic of China
42 Key Laboratory of Radio Astronomy and Technology, Chinese Academy of Sciences, A20 Datun Road, Chaoyang District, Beijing, 100101, People's Republic of
                                                                                                                        China
                                      <sup>43</sup>Department of AstronomyYonsei University,Yonsei-ro 50,Seodaemun-gu)3722 SeoulRepublic of Korea
                             <sup>44</sup>Physics Department, airfield University, 1073 North Benson Road, airfield, CT 06824, USA
<sup>45</sup>Department of Astronomy, University of Illinois at Urbana-Champaigri, 202 West Green Street, brana, IL 61801, USA
                       46 Instituto de Astronomía Universidad Nacional Autónoma de México (UNAMApdo Postal 70-264 Ciudad de México México
                             Institut für Theoretische PhysikGoethe-Universität Frankfurt Max-von-Laue-Straße D-60438 Frankfurt am MainGermany
                                     Research Center for Astronomical Computing Laboratory Hangzhou 311100 People's Republic of China
                        Tsung-Dao Lee Institute$hanghai Jiao Tong Universit$hengrong Road 52\hat{Shanghai201210,People's Republic of China
              50 Department of Astronomy and Columbia Astrophysics Laborat@ylumbia University,500 W. 120th StreetNew York, NY 10027, USA
                                             Center for Computational Astrophysics latiron Institute, 162 Fifth Avenue, New York, NY 10010, USA
   Dipartimento di Fisica "E.Pancini," Universitá di Napoli "Federico II," ComplUniv. di Monte S. Angelo, Edificio G, Via Cinthia, I-80126, Napoli, Italy
                   Wits Centre for Astrophysics University of the Witwatersrand Jan Smuts Avenue Braamfontein Johannesburg 205 South Africa
                                                              Department of Physics University of Pretoria Hatfield, Pretoria 0028 South Africa
      <sup>56</sup>Centre for Radio Astronomy Techniques and Technologlespartment of Physics and Electronics hodes University Makhanda 6140 South Africa <sup>57</sup> ASTRON, Oude Hoogeveensedijk 4,991 PD Dwingeloo, The Netherlands
          LESIA, Observatoire de Paris Jniversité PSL,CNRS, Sorbonne Université Jniversité de Paris place Jules Jansse Fr,92195 Meudon France

JILA and Department of Astrophysical and Planetary Science versity of Colorado, Boulder, CO 80309, USA
     National Astronomical Observatorieshinese Academy of Science AD Datun Road, Chaoyang District Beijing 100101, People's Republic of China
                                                        <sup>1</sup>Las Cumbres Observator 7,740 Cortona Drive Suite 102, Goleta, CA 93117-5575, USA <sup>62</sup> Department of Physics University of California, Santa Barbara CA 93106-9530, USA
                                                 63 National Radio Astronomy Observator 20 Edgemont Road Charlottesville, VA 22903, USA
   64 Department of Electrical Engineering and Computer ScieMæssachusetts Institute of Technolo∰2-D476,77 Massachusetts Avenu€ambridgeMA
                                                                                                                   02142,USA
                                                                           <sup>65</sup>Google Research 55 Main St., Cambridge MA 02142, USA
                           66 Institut für Theoretische Physik und Astrophysikiniversität Würzburg Emil-Fischer-Str31, D-97074 Würzburg Germany
                                                             Department of History of Science Harvard University, Cambridge, MA 02138, USA
```

```
<sup>68</sup>Department of PhysicsHarvard University,Cambridge,MA 02138, USA
                                           <sup>69</sup> NCSA. University of Illinois, 1205 W. Clark Street, Urbana, IL 61801, USA
         70 Instituto de Astronomia Geofísica e Ciências Atmosféricas, Universidade de São Paulo, Matão, 1226, São Paulo, P 05508-090 Brazil
                        Dipartimento di Fisica Università degli Studi di Cagliari SP Monserrato-Sestu km 0.F.09042 Monserrato (CA) Italy

To INAF—Osservatorio Astronomico di Cagliari a della Scienza 5I-09047 Selargius (CA) Italy

To INFN, sezione di Cagliari I-09042 Monserrato (CA) Italy
                                  <sup>74</sup>CP3-Origins,University of Southern DenmarkCampusvej 55DK-5230 Odense MDenmark
                          <sup>75</sup> Instituto Nacional de AstrofísicaÓptica y ElectrónicaApartado Postal 51 y 21672000.Puebla Pue.México
                    <sup>76</sup> Conseio Nacional de Humanidad iencia y Tecnología Av. Insurgentes Sur 1582/3940, Ciudad de México México
            77 Key Laboratory for Research in Galaxies and Cosmolo@ninese Academy of Science\hat{Shanghai 20003@eople's Republic of China
             78 Mizusawa VLBI ObservatoryNational Astronomical Observatory of Japan, 12 Hoshigaoka Mizusawa, Oshu, Iwate 023-0861 Japan
     <sup>79</sup> Department of Astronomical Sciencēhe Graduate University for Advanced Studies (SOKENDÆ)21-1 OsawaMitaka, Tokyo 181-8588 Japan
   80 NOVA Sub-mm Instrumentation Group apteyn Astronomical Institute Iniversity of Groningen Landleven 12,9747 AD Groningen, The Netherlands
                            Department of AstronomySchool of PhysicsPeking University,Beijing 100871,People's Republic of China
                         82 Kavli Institute for Astronomy and Astrophysics eking University, Beijing 100871, People's Republic of China
              <sup>83</sup> Department of AstronomyGraduate School of Science he University of Tokyo,7-3-1 Hongo,Bunkyo-ku,Tokyo 113-0033,Japan
                                     The Institute of Statistical Mathematics 0-3 Midori-cho, Tachikawa, Tokyo, 190-8562, Japan
    Begartment of Statistical Science he Graduate University for Advanced Studies (SOKENDAI)-3 Midori-cho, Tachikawa, Tokyo 190-8562 Japan
             Kavli Institute for the Physics and Mathematics of the University of Tokyo,5-1-5 Kashiwanohakashiwa,277-8583,Japan

87 Leiden ObservatoryLeiden University,Postbus 23009513 RA Leiden,The Netherlands
                                                  <sup>88</sup> ASTRAVEO LLC, P.O. Box 1668, Gloucester MA 01931, USA
                                                <sup>89</sup> Applied Materials Inc.,35 Dory Road,Gloucester,MA 01930, USA
                         90 Institute for Astrophysical ResearcBoston University,725 Commonwealth Avenueoston,MA 02215, USA
                       <sup>91</sup>Institute for Cosmic Ray Researchhe University of Tokyo,5-1-5 Kashiwanohakashiwa,Chiba 277-8582Japan
                                Joint Institute for VLBI ERIC (JIVE), Oude Hoogeveensedijk 4991 PD Dwingeloo, The Netherlands
                   <sup>93</sup>Department of Astronomy and Atmospheric Scienderungpook National UniversityDaegu 702-701Republic of Korea
   94 Department of Physics orea Advanced Institute of Science and Technology (KAIS 29,1 Daehak-ro Yuseong-gu Daejeon 34141 Republic of Korea
                  Kogakuin University of Technology & Engineering Cademic Support Center 665-1 Nakano Hachioji, Tokyo 192-0015 Japan
                     Graduate School of Science and Technologyigata University,8050 Ikarashi 2-no-choNishi-ku, Niigata 950-2181 Japan
                        Physics DepartmenNational Sun Yat-Sen UniversityNo. 70, Lien-Hai Road, Kaosiung City 80424, Taiwan, R.O.C.
                                     National Optical Astronomy Observator $50 N. Cherry Avenue, Tucson, AZ 85719, USA 99 Department of Physics, The Chinese University of Hong Kong Shatin, N.T., Hong Kong
                           100 School of Astronomy and Space Sciendanjing University, Nanjing 210023 People's Republic of China
                  101 Key Laboratory of Modern Astronomy and Astrophysidslanjing University, Nanjing 210023 People's Republic of China
102 INAF-Istituto di Radioastronomia/ia P. Gobetti 101,I-40129 Bologna Italy
                        103 INAF-Istituto di Radioastronomia & Italian ALMA Regional Centre/ia P. Gobetti 101,I-40129 Bologna,Italy
                       104 Department of Physics National Taiwan University No. 1, Sec. 4, Roosevelt Road Taipei 10617, Taiwan, R.O.C
                        105 Instituto de Radioastronomía y Astrofísicaniversidad Nacional Autónoma de Méxicanomía 58089, México
                       106 Key Laboratory of Radio AstronomyChinese Academy of Sciencesanjing 210008 People's Republic of China
                    Yunnan ObservatoriesChinese Academy of Sciences50011 Kunming, Yunnan Province People's Republic of China
  108 Center for Astronomical Mega-Sciencehinese Academy of Science ADA Datun Road Chaoyang District Beijing, 100012, People's Republic of China
       Key Laboratory for the Structure and Evolution of Celestial Obje@sinese Academy of Science$50011 Kunming People's Republic of China 110 Anton Pannekoek Institute for Astronomylniversity of Amsterdam Science Park 9041098 XH, Amsterdam The Netherlands
 Gravitation and Astroparticle Physics Amsterdam (GRAPPA) Instituteiversity of AmsterdamScience Park 9041098 XH Amsterdam, The Netherlands

112 Department of Astrophysical Science eyoton Hall, Princeton University Princeton, NJ 08544, USA
  113 Science Support OfficeDirectorate of Science Suropean Space Research and Technology Centre (ESA/ESTIKED)erlaan 1,2201 AZ Noordwijk, The
                                                                               Netherlands
           114 School of Physics and Astronom@hanghai Jiao Tong Universit@00 Dongchuan Roa@hanghai200240,People's Republic of China 115 Institut de Radioastronomie Millimétrique (IRAM@hvenida Divina Pastora 7Local 20, E-18012,Granada@pain
                  116 National Institute of Technology, Hachinohe College 16-1 Uwanotai, Tamonoki, Hachinohe City, Aomori 039-1192, Japan
                                   Research Center for AstronomAcademy of Athens Soranou Efessiou 4115 27 Athens Greece
                                118 Department of Physics/illanova University,800 Lancaster Avenue/illanova, PA 19085,USA
119 Physics Department/Vashington UniversityCB 1105, St. Louis, MO 63130, USA
                               120 School of Physics Georgia Institute of Technology§37 State Street NWAtlanta, GA 30332, USA
Department of Astronomy and Space Science, Kyung Hee University, 1732, Deogyeong-daero, Giheung-gu, Yongin-si, Gyeonggi-do 17104, Republic of Korea
                     Canadian Institute for Theoretical Astrophysicaniversity of Toronto,60 St. George StreetToronto, ON M5S 3H8, Canada
                Dunlap Institute for Astronmy and Astrophysicshiversity of Toronto,50 St. George StreetToronto, ON M5S 3H4, Canada 124 Canadian Institute for Advanced Researding Dundas Street West, oronto, ON M5G 1Z8, Canada 125 Dundas Street West, oronto, ON M5G 1Z8, Canada 125 Dundas Street West, oronto, ON M5G 1Z8, Canada
                                            Radio Astronomy Laboratory University of California, Berkeley, CA 94720, USA
                          <sup>126</sup>Institute of AstrophysicsFoundation for Research and Technology—Hellvsutes,7110 Heraklion,Greece
                    Department of Physics National Taiwan Normal University No. 88, Sec. 4, Tingzhou Road, Taipei 116, Taiwan, R.O.C.
           128 Center of Astronomy and Gravitation National Taiwan Normal UniversityNo. 88, Sec.4, Tingzhou Road, Taipei 116, Taiwan, R.O.C.

129 Finnish Centre for Astronomy with ESCF, I-20014 University of Turku, Finland
                                 130 Aalto University Metsähovi Radio Observator Metsähovintie 114FI-02540 Kylmälä, Finland
                                          Gemini Observatory/NSF's NOIRLab670 N. A'ohōkū Place, Hilo, HI 96720, USA
                                <sup>132</sup>Frankfurt Institute for Advanced StudieRuth-Moufang-Strasse D-60438 Frankfurt,Germany
                                                         School of MathematicsTrinity College, Dublin 2, Ireland
                              <sup>134</sup>Department of Physics Iniversity of Toronto, 60 St. George Street Toronto, ON M5S 1A7, Canada
                         <sup>135</sup>Department of PhysicsTokyo Institute of Technology2-12-1 OokayamaMeguro-ku,Tokyo 152-8551 Japan
              Hiroshima Astrophysical Science Centerioshima University,1-3-1 KagamiyamaHigashi-HiroshimaHiroshima 739-8526Japan
                                 Aalto University Department of Electronics and Nanoengineer Mg,15500,FI-00076 Aalto,Finland
                                          Jeremiah Horrocks Institute Iniversity of Central Lancashire Preston PR1 2HEUK
                              National Biomedical Imaging CentePeking University, Beijing 100871, People's Republic of China College of Future Technology, Peking University, Beijing 100871, People's Republic of China
                              <sup>141</sup>Department of Physics and Astronomlyniversity of Lethbridge Lethbridge, AB T1K 3M4, Canada
```

964:L26 (37pp),2024 April 1

142 Netherlands Organisation for Scientific Research (NWR)stbus 931382509 AC Den Haag,The Netherlands
143 Department of Physics and Astronomyeoul National UniversityGwanak-gu,Seoul 08826Republic of Korea
144 University of New Mexico,Department of Physics and Astronomylbuquerque,NM 87131, USA
145 Physics DepartmenBrandeis University415 South StreetWaltham,MA 02453, USA
146 Tuorla ObservatoryDepartment of Physics and Astronomyliversity of Turku,Finland
147 Radboud Excellence Fellow of Radboud Universityimegen,The Netherlands
148 School of Natural Sciencestritute for Advanced Studyl Einstein Drive,Princeton,NJ 08540,USA
149 School of PhysicsHuazhong University of Science and TechnologyUhan,Hubei, 430074,People's Republic of China
150 Mullard Space Science LaboratoryIniversity College LondonHolmbury St. Mary, Dorking, Surrey,RH5 6NT, UK
151 Center for Astronomy and Astrophysics and Department of Physfordian University,Shanghai 200438;People's Republic of China
152 Astronomy DepartmentUniversity of Science and Technology of Chinalefei 230026,People's Republic of China
153 Department of Physics and Astronomylichigan State University567 Wilson Road East LansingMI 48824, USA